UNIVERSITY OF MICHIGAN
NOV 15 1950
ENGINEERING LIBRARY

JOURNAL OF THE AERONAUTICAL SCIENCES

VOLUME 17 NOVEMBER, 1950 NUMBER 11

CONTENTS

Lift on Inclined Bodies of Revolution in Hypersonic Flow
G. GRIMMINGER, E. P. WILLIAMS, AND G. B. W. YOUNG 675

The Longitudinal Stability of Elastic Swept Wings at Supersonic Speed
C. W. FRICK AND R. S. CHUBB 691

A System for the Excitation of Pure Natural Modes of Complex Structure
ROBERT C. LEWIS AND DONALD L. WRISLEY 705

The Flow over a Wedge Profile at Mach Number 1
G. GUDERLEY AND H. YOSHIHARA 723

Effect of Torsional Stiffness Requirements on Wing Structural Weight
W. R. MICKS 736

Readers' Forum: "Roll to Sideslip or Yaw Ratios," by Dunstan Graham and Allan McCaskill; "On the Plastic Buckling of Plates," by P. P. Bijlaard; "Plastic Column Behavior," by N. J. Hoff; "A Note on the Calculation of Oblique Shock-Wave Characteristics," by M. J. Thompson 741–744

Published by the

INSTITUTE OF THE AERONAUTICAL SCIENCES, INC.

JOURNAL OF THE AERONAUTICAL SCIENCES

Editor: HUGH L. DRYDEN, *Director, N.A.C.A.*

Associate Editor: ROBERT R. DEXTER *Managing Editor:* BERNEICE H. JARCK

The Institute of the Aeronautical Sciences publishes monthly the JOURNAL OF THE AERONAUTICAL SCIENCES and the AERONAUTICAL ENGINEERING REVIEW.

The JOURNAL OF THE AERONAUTICAL SCIENCES prints papers of scientific and technical interest to Institute members and subscribers. In general, it provides an opportunity for specialists to publish articles disclosing new knowledge and new applications in the field of the aeronautical sciences. The JOURNAL restricts itself to the aeronautical aspects of advances in science and engineering, and papers printed have either been submitted directly to the JOURNAL or have been previously presented at a meeting of the Institute.

The AERONAUTICAL ENGINEERING REVIEW keeps members and subscribers informed regarding the contents of new books and current periodicals in the field of aeronautics. It reviews new developments in the aircraft industry and reports on progress from house organs and catalogs published by aircraft and engine manufacturers and other companies engaged in aeronautical activities. It publishes papers on applied engineering and aircraft production. News of Institute activities is published in the REVIEW.

Statements and opinions expressed in the JOURNAL are to be understood as individual expressions of the authors and not those of the Institute.

SUBSCRIPTION RATES

Journal of the Aeronautical Sciences
Published Monthly

United States and Possessions		Foreign Countries Including Canada (American Currency Rate)	
1 Year	$12.00	1 Year	$13.00
Single Copies	1.50	Single Copies	1.50

Aeronautical Engineering Review
Published Monthly

United States and Possessions		Foreign Countries Including Canada (American Currency Rates)	
1 Year	$3.00	1 Year	$3.50
Single Copies	0.50	Single Copies	0.50

Notices of change of address should be sent to the Institute at least 30 days prior to actual change of address.

Manuscripts for publication, proofs, and all correspondence should be addressed to the Editorial Office of the JOURNAL.

Correspondence regarding subscriptions may be addressed to Publication Office, 20th and Northampton Sts., Easton, Pa., or to the Editorial Office of the JOURNAL OF THE AERONAUTICAL SCIENCES, 2 East 64th Street, New York 21, New York.

Copyright, 1950, by the Institute of the Aeronautical Sciences, Inc.

Entered as Second Class Matter at the Post Office, Easton, Pa , May 1, 1937. Acceptance for mailing at a special rate of Postage provided for in the Act of August 24, 1912. Authorized April 29, 1937.

JOURNAL OF THE AERONAUTICAL SCIENCES

VOLUME 17 NOVEMBER, 1950 NUMBER 11

Lift on Inclined Bodies of Revolution in Hypersonic Flow

G. GRIMMINGER,* E. P. WILLIAMS,† AND G. B. W. YOUNG‡

The RAND Corporation

SUMMARY

The importance of body lift lies in the fact that at moderate angles of attack and high Mach Number it can constitute an appreciable part of the total lift of a winged missile. In this paper an attempt has been made to analyze body lift in hypersonic flow by an approximate method and, together with a correlation of existing experimental data, to indicate the probable variation of body lift over a wide range of Mach Numbers extending from low supersonic to hypersonic. The method of analysis of hypersonic flow over inclined bodies of revolution employed herein has been denoted as the *hypersonic approximation*. It is an improvement on the Newtonian corpuscular theory of aerodynamics, since it considers the centrifugal forces resulting from the curved paths of the air particles in addition to the impact (Newtonian) forces.

SYMBOLS

A = cross-section area
$\boldsymbol{b}$ = unit vector tangent to a circular parallel
C_N = normal force coefficient $= N/q_0\pi r_B^2$
C_N' = local normal force coefficient $= dC_N/d(x/d_B)$
C_p = $(p - p_0)/q_0$ = pressure coefficient
C_X = axial force coefficient $= X/q_0\pi r_B^2$
C_X' = local axial force coefficient $= dC_X/d(x/d_B)$
d = diameter
l = length
M_0 = free-stream Mach Number
$\dot{m}$ = rate of mass flow
N = normal force—that is, force normal to longitudinal axis of body
$\boldsymbol{n}$ = unit vector normal to surface, positive inward
p = static pressure
q = $(1/2)\rho V^2$ = dynamic pressure
R = radius of normal curvature of a stream line
r = radius
S = surface area
$\boldsymbol{t}$ = unit vector tangent to a meridian
V = velocity
$\boldsymbol{V}_0$ = free-stream velocity vector
V_s = velocity of flow over the surface of the body
X = axial force—that is, force in direction of longitudinal axis of body
x = distance along longitudinal axis of body
α = angle of attack
β = angular position of a point on the surface of the body
β_u = upper limit of integration around a circular parallel
γ = angle between body stream line and a meridian
δ_B = thickness of body layer
η = angle between $\boldsymbol{V}_0$ and $\boldsymbol{n}$
θ = angle between $\boldsymbol{t}$ and the longitudinal axis of the body
θ_v = semivertex angle of cone
ρ = mass density
ρ_B = density in body layer

Subscripts

$()_B$ = based on maximum body dimensions
$()_c$ = centrifugal force values
$()_C$ = converging or boat-tail section
$()_D$ = nose or diverging section
$()_e$ = refers to expansion flow
$()_i$ = impact values
$()_S$ = straight or cylindrical section
$()_0$ = based on free-stream conditions

(I) INTRODUCTION

IN THE FIELD OF GUIDED MISSILES, investigations of possible performance will inevitably lead to the consideration of flight at higher and higher Mach Numbers. Although for some missiles the Mach Number $M_0 = 5$ might be considered as the upper end of the speed range, for missiles of a different category the high-speed range of flight can conceivably extend to $M_0 = 20$ or 25. As far as wing aerodynamics is concerned, for supersonic speeds up to $M_0 = 5$ the wing lift may be obtained with satisfactory accuracy by means of the linearized supersonic wing theories, and at higher Mach Numbers satisfactory results are obtained on the basis of two-dimensional gas dynamics.

Presented at the Aerodynamics Session, Eighteenth Annual Meeting, I.A.S., New York, January 23–26, 1950. Revised and received April, 1950.

* Physical Scientist. Now with the Department of Defense, Washington, D.C., as Scientific Warfare Adviser.

† Aerodynamics Engineer.

‡ Research Engineer.

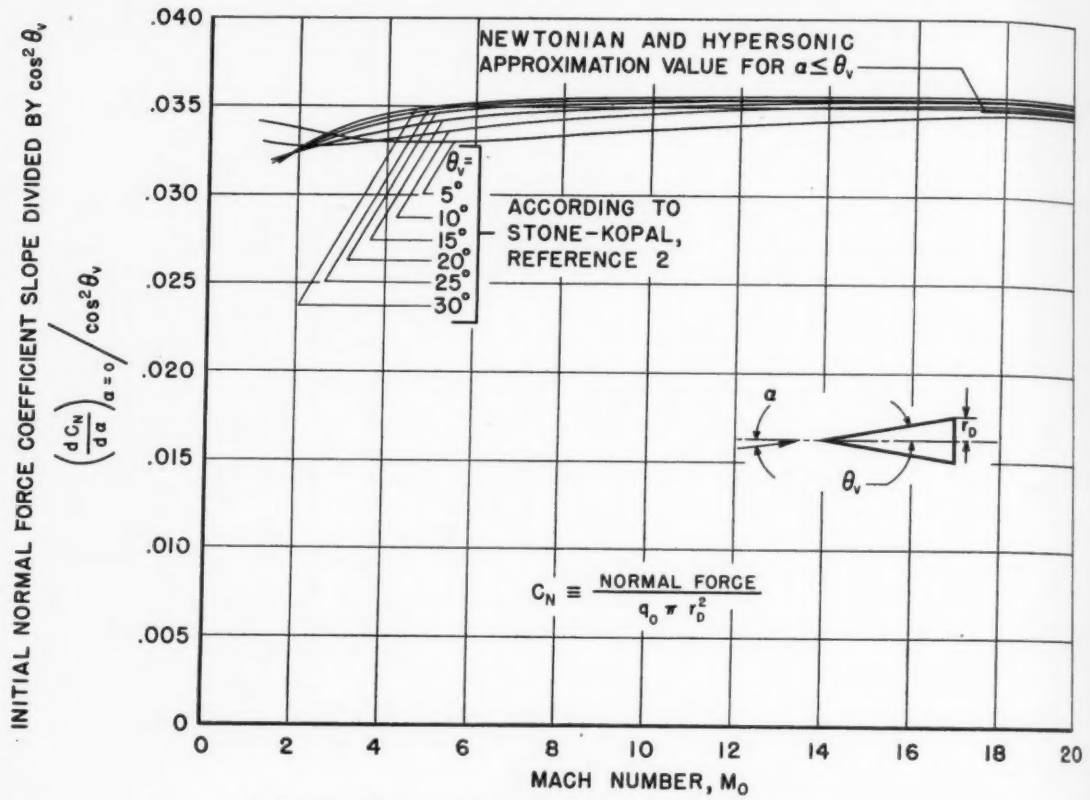

FIG. 1. Cone normal force coefficient slope vs. Mach Number.

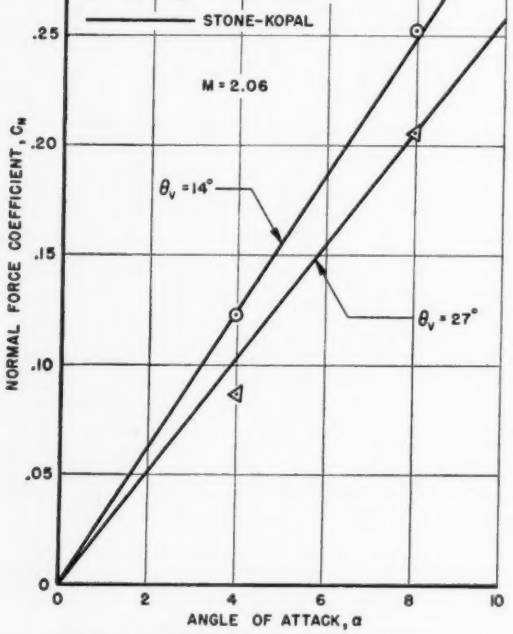

FIG. 2. Normal force coefficient for cones.

However, this is not at all the case for strictly three-dimensional flow such as that over a yawed body of revolution. In the usual application of linearized theories in two- and three-dimensional flow, wherein the higher order terms are neglected throughout for the sake of consistency, good solutions can be obtained for supersonic wings but not for body lift. Furthermore, these linearized solutions are subject to Mach Number limitations. On the other hand, reliable theoretical lift results exist for cones at the present time.[1, 2] This yawed cone theory gives the exact initial normal force slope that is practically independent of Mach Number and in excellent agreement with the hypersonic approximation of the present paper as shown by Fig. 1; agreement with some experimental data is shown in Fig. 2. Less is known about the lift of an ogive, however, and still less about the lift of a cylinder following either a cone or ogive.

In view of the fact that at the higher Mach Numbers body lift can constitute an appreciable part of the total lift of a winged missile, an attempt has been made to analyze body lift in hypersonic flow by an approximate method and, together with an analysis of existing experimental data, to indicate the probable variation of body lift over a wide range of Mach Numbers extending from low supersonic to hypersonic. First, the Newtonian analysis is presented for an arbitrary inclined

body of revolution. The resulting forces on a cone and cylinder are then given. Centrifugal force effects reduce the cylinder normal force resulting from the Newtonian analysis by approximately 10 per cent. Corresponding effects for slender cones and ogives are less for the angle-of-attack range of general interest ($\alpha < 2\theta_v$); therefore, for practical purposes, the Newtonian analysis needs no modification for predicting the lift on the nose of a body of revolution at extremely high Mach Numbers. A qualitative discussion of the pressures on cone and cylinder areas situated in regions of expansion flow at hypersonic speeds is then presented. It serves as a guide for extending the results of the following correlation of experimental lift data through the hypersonic region to the hypersonic approximation values. A more detailed discussion and analysis of centrifugal force effects are given in the Appendix.

(II) The Newtonian (Impact) Aerodynamic Forces on a Yawed Body of Revolution

In view of the general lack of exact gas dynamic results for three-dimensional flow, it is important to realize that valuable results concerning the lift on a pointed body of revolution can be obtained from the relatively simple theory of Newtonian aerodynamics. At high supersonic Mach Numbers, particularly when the angle of attack is appreciable, the gas pressure forces on a body may be approximated in a simple manner on the basis of the concept of Newtonian flow.[3–5] In Newtonian flow it is assumed that the gas stream maintains its speed and direction unchanged until it strikes the solid surface exposed to the flow, whereupon it loses the component of momentum normal to the surface and moves along the surface with the tangential component of momentum unchanged. Thus, in this concept the shock wave is assumed to lie on, or follow, the surface of the body. The Newtonian approximation does not specify the pressure on surfaces that do not "see" the flow—that is, surfaces on which gas dynamics would predict expansion flow. For a flat plate inclined at an angle to the flow, the Newtonian pressure coefficient on the lower surface is

$$C_p \equiv (p - p_0)/q_0 = 2 \sin^2 \alpha \qquad (1)$$

where p_0 denotes free-stream pressure and $q_0 = \rho_0 V_0^2/2$ is the free-stream dynamic pressure.

The concept of Newtonian flow can also be approached from the exact two-dimensional gas dynamical equations by letting $M_0 \to \infty$. Considering a flat plate inclined to the flow, there will be shock flow over the lower surface and expansion flow over the upper surface. As the Mach Number increases, the shock wave approaches closer and closer to the lower surface (leading to increasing pressures) and the amount of expansion increases on the upper surface (leading to decreasing pressures). In the limit when $M_0 = \infty$, both the pressure and the pressure coefficient on the upper surface become zero, and the pressure coefficient on the lower surface becomes[6]

$$C_p = (\gamma + 1) \sin^2 \alpha = C_N \qquad (2)$$

where γ is the ratio of the specific heats. Since the upper surface pressure coefficient is zero, Eq. (2) is also the expression for the normal force coefficient C_N. It is indicated in reference 4 that $\gamma \to 1$ as $M_0 \to \infty$, which brings Eq. (2) into agreement with the Newtonian result, Eq. (1). It is worth pointing out that for a given Mach Number and angle of attack the Newtonian theory gives considerably better results for a three-dimensional body than for a two-dimensional body. Thus, the Newtonian hypersonic approximation for a pointed body of revolution (such as a cone, for example) is surprisingly good and is much better than for a two-dimensional flat plate.

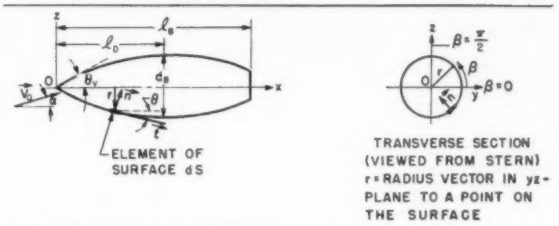
ELEMENT OF SURFACE dS
TRANSVERSE SECTION (VIEWED FROM STERN)
r = RADIUS VECTOR IN yz-PLANE TO A POINT ON THE SURFACE
V_0 = FREE-STREAM VELOCITY VECTOR
n = UNIT VECTOR NORMAL TO A SURFACE ELEMENT
t = UNIT VECTOR TANGENT TO SURFACE ELEMENT AND LYING IN A PLANE CONTAINING THE x-AXIS
d_B = MAXIMUM DIAMETER OF BODY
ℓ_B = TOTAL LENGTH OF BODY
ℓ_D = LENGTH OF DIVERGING PORTION OF BODY
θ_v = SEMI-VERTEX ANGLE AT THE NOSE

FIG. 3. Body of revolution inclined at an angle to Newtonian flow.

(A) *Arbitrary Body of Revolution*

To derive the Newtonian pressure forces on a body of revolution of general shape, consider the body shown in Fig. 3 for which the longitudinal axis of symmetry is the positive x-axis. The angle of attack α is the angle in the xz-plane between the free-stream velocity vector $\boldsymbol{V}_0$ and the positive x-axis. The y-axis is perpendicular to the xz-plane, forming a right-handed system of coordinates. Consider a differential element of surface area dS at an arbitrary point O' on the surface of the body, and let x', y', z' denote a local right-handed system of coordinates at the point O', such that x', y', z' are parallel respectively to x, y, z. Let r, β be the polar coordinates in the yz-plane of the point O' on the surface of the body. Let $\boldsymbol{n}$ be a unit vector that is normal to the surface element dS and positive in the inward direction. Let $\boldsymbol{t}$ be a unit vector that is tangent to the element dS, forming an angle θ with the positive x'-axis. Let $\boldsymbol{b}$ denote a unit vector that, together with $\boldsymbol{n}$ and $\boldsymbol{t}$, forms a right-handed coordinate system, such that $\boldsymbol{b} = \boldsymbol{n} \times \boldsymbol{t}$. For a body of revolution, which is the only case to be considered here, $\boldsymbol{t}$ is tangent to a meridian and therefore lies in the plane formed by the line

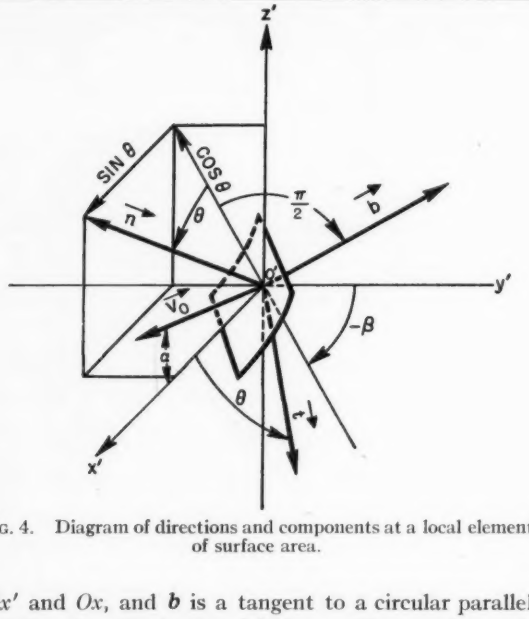

FIG. 4. Diagram of directions and components at a local element of surface area.

$O'x'$ and Ox, and $\boldsymbol{b}$ is a tangent to a circular parallel and therefore lies in the $y'z'$-plane. The angular position of the point O' (and the vector $\boldsymbol{n}$) is given by the angle β, which is measured positive counterclockwise from the positive y'-axis. The angle θ between $O'x'$ and $\boldsymbol{t}$ is considered positive in the sense of a counterclockwise rotation about $\boldsymbol{b}$.

The relations between the $\boldsymbol{n}$, $\boldsymbol{t}$, $\boldsymbol{b}$ coordinate system and the x', y', z' system (Fig. 4) are given in Table 1.

TABLE 1
Direction Cosines

	x'	y'	z'
$\boldsymbol{t}$	$\cos\theta$	$\sin\theta\cos\beta$	$\sin\theta\sin\beta$
$\boldsymbol{b}$	0	$-\sin\beta$	$\cos\beta$
$\boldsymbol{n}$	$\sin\theta$	$-\cos\theta\cos\beta$	$-\cos\theta\sin\beta$
$\boldsymbol{V}_0$	$\cos\alpha$	0	$\sin\alpha$

The free-stream velocity vector $\boldsymbol{V}_0$ lies in the $x'z'$-plane and makes an angle α (angle of attack) with the positive x'-axis. The angle η between the velocity vector $\boldsymbol{V}_0$ and the normal $\boldsymbol{n}$ is given by

$$\cos\eta \equiv \cos(\boldsymbol{V}_0, \boldsymbol{n}) = \cos\alpha\sin\theta - \sin\alpha\cos\theta\sin\beta \quad (3)$$

The condition for Newtonian flow is imposed by specifying that the gas stream upon striking the surface loses all of its momentum in the direction normal to the surface. Since the component of $\boldsymbol{V}_0$ normal to the surface element dS is $\boldsymbol{V}_0\cos\eta$ and the rate of mass flow striking the element is $\rho_0 V_0\cos\eta\, dS$, the rate of change of momentum on the surface element in the direction of its normal is

$$V_0\cos\eta \times \rho_0 V_0\cos\eta\, dS = \rho_0 V_0^2\cos^2\eta\, dS$$

Thus, the excess local pressure force df produced by the momentum change is

$$df \equiv (p - p_0)\, dS = \rho_0 V_0^2\cos^2\eta\, dS = 2q_0\cos^2\eta\, dS \quad (4)$$

and the local pressure coefficient is

$$C_p \equiv (p - p_0)/q_0 = 2\cos^2\eta = 2(\cos\alpha\sin\theta - \sin\alpha\cos\theta\sin\beta)^2 \quad (5)$$

With respect to body axes, the forces on the body may be separated into a normal force N in the z-direction and an axial force X in the x-direction (Fig. 3). For an element of area which "sees" the flow, the force components are

$$dN = -q_0 C_p\sin\beta\cos\theta\, dS = -q_0 C_p r\sin\beta\, d\beta\, dx \quad (6)$$

since $dS\cos\theta = r\, d\beta\, dx$ and

$$dX = q_0 C_p\sin\theta\, dS = q_0 C_p r\tan\theta\, d\beta\, dx \quad (7)$$

The total force is obtained by integration over the surface of the body. In general, C_p will be a function of both x and β.

Consideration must now be given to those portions of the body surface which are inclined away from the free-stream direction $\boldsymbol{V}_0$ and which may therefore be thought of as lying in the "shadow" of the free stream. This situation is illustrated in Fig. 5. As the flow proceeds over the body, there will exist a boundary ac determined by the condition $C_p = 0$ (that is, $p = p_0$). All of the body surface situated upstream from ac is exposed to the oncoming flow that, upon striking the surface, undergoes compression according to Eq. (5). All of the body surface downstream from ac is in a region of expansion flow for which Eq. (5) has no meaning. Along the boundary ac, the tangent vector $\boldsymbol{t}$ and the free-stream vector $\boldsymbol{V}_0$ both lie in the same plane—the tangent plane—and, consequently, $\boldsymbol{n}$ and $\boldsymbol{V}_0$ are perpendicular. This condition defines ac and, from Eq. (3), leads to the relation

$$\cos\eta_u = \cos\alpha\sin\theta_u - \sin\alpha\cos\theta_u\sin\beta_u = 0$$

or

$$\sin\beta_u = (\tan\theta_u/\tan\alpha) \quad (8)$$

where the subscript $(\,)_u$ refers to conditions along the

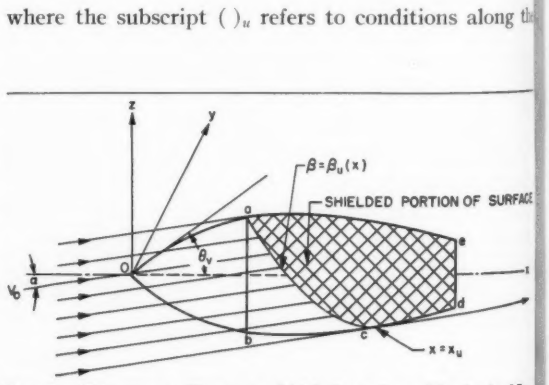

FIG. 5. Diagram to illustrate shielded portion of body in Newtonian flow.

boundary ac, which defines the limit of the compression flow area.

For all transverse sections (sections normal to the x-axis) from the nose back to the section ab, the limits of integration for β are from $-\pi/2$ to $+\pi/2$. Downstream from the section ab, the upper limit for β, β_u must correspond to the points lying on the boundary ac and will be a function of x. The point c, designated by $x = x_u$, is the last point on the body to intercept any of the free-stream flow, and at this point $\beta_u = -\pi/2$ (Fig. 5). The extreme forward tip of a pointed body may be assumed to be conical over a short distance. Let the semivertex angle of the cone tip be denoted by θ_v. When $\alpha < \theta_v$, the point a is situated along the top meridian ($\beta = \pi/2$) at the point where $\theta = \alpha$. When $\alpha \geq \theta_v$, the point a is situated at the beginning of the body ($x = 0$). Thus, in integrating Eqs. (6) and (7), two cases must be distinguished: (1) $\alpha \leq \theta_v$, some transverse sections are completely exposed to the flow with $\beta_u = \pi/2$; (2) $\alpha > \theta_v$, the transverse sections are only partially exposed to the flow with $\beta_u = \sin^{-1}(\tan\theta/\tan\alpha)$.

Concerning the pressures on the shadowed or shielded portions of surface lying in expansion flow, which may be denoted by p_e, little can be said except that $0 < p_e < p_0$. If it should be assumed that the flow is completely separated over the shielded regions, it would then be appropriate to use $p_e = p_0$, which gives $C_{p_e} = 0$ for the pressure coefficient. The general relation for the pressure coefficient is*

$$C_{p_e} = (2/\gamma M_0^2)\,[(p_e/p_0) - 1] \tag{9}$$

* The value $\gamma = 1.4$ should be used for expansion flow.

If it is assumed that separation does not occur, p_e/p_0 becomes small compared to unity as M_0 increases, and, when $M_0 = \infty$, both p_e/p_0 and C_{p_e} are zero. Since $C_{p_e} = 0$ for either of these possible extremes, the shielded portions of the surface would contribute nothing to the integrals of Eqs. (6) and (7).

Thus, for true Newtonian conditions corresponding to $M_0 = \infty$, the total normal and axial force on the body obtained from Eqs. (6) and (7) are†

$$N = -2q_0 \int_0^{x_u} \int_{-\pi/2}^{\beta_u} C_p r \sin\beta \, d\beta \, dx \tag{10}$$

$$X = 2q_0 \int_0^{x_u} \int_{-\pi/2}^{\beta_u} C_p r \tan\theta \, d\beta \, dx \tag{11}$$

where C_p is given by Eq. (5). The Newtonian results, Eqs. (10) and (11), can be used as hypersonic approximations provided the Mach Number is sufficiently large ($M_0 = 15$, for example). When separation does not occur, C_{p_e} increases with decreasing Mach Number, and, as lower Mach Numbers are considered ($M_0 < 10$ or 15, for example), it would be necessary to allow for values of C_{p_e} different from zero because the pressures on the expansion areas begin to have an appreciable effect on the lift. On the other hand, for decreasing Mach Numbers, the value of C_p given by Eq. (5) for the pressure on compression areas is less than the gas dynamic value and can therefore still be used as a conservative estimate for the compression flow. In this Mach Number range, an approximation to the aerodynamic forces could be written in the form

† Although no mention has been made of the base pressure coefficient, when $M_0 = \infty$ it vanishes in the same fashion as C_{p_e}.

$$N = -2q_0 \int_0^{x_u} \int_{-\pi/2}^{\beta_u} C_p r \sin\beta \, d\beta \, dx - 2q_0 \int_0^{l_B} \int_{\beta_v}^{\pi/2} C_{p_e} r \sin\beta \, d\beta \, dx \tag{12}$$

$$X = 2q_0 \int_0^{x_u} \int_{-\pi/2}^{\beta_u} C_p r \tan\theta \, d\beta \, dx + 2q_0 \int_0^{l_B} \int_{\beta_u}^{\pi/2} C_{p_e} r \tan\theta \, d\beta \, dx \tag{13}$$

where it is understood that C_{p_e} may be put equal to zero without introducing appreciable error when the Mach Number is high enough or when separation occurs.

Before obtaining the integrals (10) and (11) for a particular body shape, it is convenient to derive the general expressions for the local forces on a transverse section. The normal force coefficient C_N for the entire body is defined by $C_N = N/q_0\pi r_B^2$, where $d_B = 2r_B$ is the maximum diameter of the body. Axial distance along the x-axis will be expressed in units of x/d_B. Considering only the first term in Eq. (10) corresponding to the surfaces in compression flow, the local normal force coefficient per unit length, C_N', is

$$C_N' \equiv \frac{dC_N}{d(x/d_B)} = \frac{1}{q_0\pi r_B^2} \frac{dN}{d(x/d_B)} = -\frac{4}{\pi} \frac{r}{r_B} \int_{-\pi/2}^{\beta_u} C_p \sin\beta \, d\beta \tag{14}$$

where r is a function of x only. Introducing

$$C_p = 2(\cos\alpha \sin\theta - \sin\alpha \cos\theta \sin\beta)^2$$

from Eq. (5), the integration yields

$$C_N' = \frac{4}{\pi}\frac{r}{r_B} \times$$

$$\left\{\frac{1}{2}\left(\beta_u + \frac{\pi}{2}\right)\sin 2\alpha \sin 2\theta + \cos\beta_u\left[2\cos^2\alpha\sin^2\theta - \frac{1}{2}\sin 2\alpha \sin 2\theta \sin\beta_u + \frac{2}{3}\sin^2\alpha\cos^2\theta(\sin^2\beta_u + 2)\right]\right\} \quad (15)$$

Introducing an axial force coefficient $C_X = X/q_0\pi r_B^2$, the local axial force coefficient per unit length is written

$$C_X' \equiv \frac{dC_X}{d(x/d_B)} = \frac{1}{q_0\pi r_B^2}\frac{dX}{d(x/d_B)} = \frac{4}{\pi}\frac{r}{r_B}\tan\theta\int_{-\pi/2}^{\beta_u} C_p\, d\beta \quad (16)$$

where θ is a function of x only. The integration yields

$$C_X' = \frac{4}{\pi}\frac{r}{r_B}\tan\theta\left[\left(\beta_u + \frac{\pi}{2}\right)(2\cos^2\alpha\sin^2\theta + \sin^2\alpha\cos^2\theta) + \cos\beta_u(\sin 2\alpha\cos 2\theta - \sin^2\alpha\cos^2\theta\sin\beta_u)\right] \quad (17)$$

Distinction is now made between the two cases $\alpha \leq \theta_v$ and $\alpha > \theta_v$.

Case 1. $\alpha \leq \theta_v$: For this case $\beta = \pi/2$ and Eqs. (15) and (17) reduce to

$$C_N' = 2(r/r_B)\sin 2\alpha \sin 2\theta \quad (18)$$

and

$$C_X' = 4(r/r_B)\tan\theta[2\sin^2\theta + \sin^2\alpha(1 - 3\sin^2\theta)] \quad (19)$$

Case 2. $\alpha > \theta_v$: In this case, Eq. (8),

$$\beta_u = \sin^{-1}(\tan\theta/\tan\alpha)$$

and

$$\cos\beta_u = \sqrt{1 - (\tan^2\theta/\tan^2\alpha)}$$

and Eqs. (15) and (17) reduce to

$$C_N' = 4\frac{r}{r_B}\cos^2\theta\sin 2\alpha\left\{\frac{[\beta_u + (\pi/2)]}{\pi}\tan\theta + \frac{1}{3\pi}\cos\beta_u(\cot\alpha\tan^2\theta + 2\tan\alpha)\right\} \quad (20)$$

$$C_X' = 4\frac{r}{r_B}\tan\theta\left\{\frac{[\beta_u + (\pi/2)]}{\pi}[2\sin^2\theta + \sin^2\alpha(1 - 3\sin^2\theta)] + \frac{3}{4\pi}\cos\beta_u\sin 2\alpha\sin 2\theta\right\} \quad (21)$$

Eqs. (18) through (21) are the general expressions for the normal and axial forces on local transverse sections of the body, assuming $C_{pe} = 0$ on the shielded surfaces and neglecting centrifugal forces in the flow. The total normal and axial forces are obtained by integrating these local values over the length of the body. In order to apply the equations to a particular body of revolution, the profile of the body shape is introduced by specifying θ as a function of x. Of particular interest in missile aerodynamics is the body consisting of cone plus cylinder. According to the Newtonian approximation that has been outlined, the pressure forces on a body are determined entirely by the local value of θ; consequently, the force on any portion of a body may be evaluated separately, and the total force may be obtained by addition.

(*B*) *Cone*

For a right circular cone of length l_D, base radius r_D, and semivertex angle θ_v, we have

$$x_u = l_D = \frac{r_D}{\tan\theta_v}; \qquad \theta = \text{const.} = \theta_v; \qquad \frac{r}{r_B} \equiv \frac{r}{r_D} = \frac{x}{l_D}$$

As before, two cases must be distinguished corresponding to $\alpha \leq \theta_v$ and $\alpha > \theta_v$.

Case 1. $\alpha \leq \theta_v$—$\beta_u = \pi/2$: From Eq. (18), it follows that

$$C_N = \int^{l_D/d_D} C_N'\, d(x/d_D) = (l_D/d_D)\sin 2\theta_v \sin 2\alpha$$

Since $l_D/d_D = 1/(2\tan\theta_v)$, this may be written

$$C_N = \cos^2\theta_v \sin 2\alpha \quad (22)$$

Similarly, from Eq. (19), the axial coefficient is

$$C_X = 2 \sin^2 \theta_v + \sin^2 \alpha(1 - 3 \sin^2 \theta_v) \tag{23}$$

It is interesting to examine the value of the initial lift curve slope for the cone. It is simply

$$(dC_L/d\alpha)_{\alpha=0} \equiv (dC_N/d\alpha)_{\alpha=0} = 2 \cos^2 \theta_v \tag{24}$$

For a slender cone ($\theta_v \to 0$) this reduces to the slender body result, $dC_L/d\alpha = 2$. This gives the rather surprising result that at small angles of attack the lift coefficient for a slender diverging body has nearly the same value at extremely high Mach Numbers as at extremely low supersonic speeds. This indicates that for a body of this type at small angles of attack the lift coefficient is essentially independent of Mach Number. This conclusion is completely borne out by the Stone-Kopal values for cone lift at small angle of attack shown in Fig. 1.

Case 2. $\alpha > \theta_v - \beta_u = \sin^{-1}(\tan \theta_v / \tan \alpha)$: For this case, it follows from Eq. (20) that

$$C_N = \cos^2 \theta_v \sin 2\alpha \left\{ \frac{[\beta_u + (\pi/2)]}{\pi} + \frac{1}{3\pi} \cos \beta_u (\tan \theta_v \cot \alpha + 2 \cot \theta_v \tan \alpha) \right\} \tag{25}$$

and from Eq. (21) that

$$C_X = \frac{[\beta_u + (\pi/2)]}{\pi} [2 \sin^2 \theta_v + \sin^2 \alpha(1 - 3 \sin^2 \theta_v)] + \frac{3}{4\pi} \cos \beta_u \sin 2\theta_v \sin 2\alpha \tag{26}$$

The center of pressure on the cone may be found by taking moments about the vertex. If a is the distance from the vertex to the center of pressure, this distance is determined by the relation

$$a = \frac{\text{moment}}{\text{normal force}} = \frac{d_D \int_0^{l_D/d_D} \frac{x}{d_D} C_N' \, d\left(\frac{x}{d_D}\right)}{C_N} \tag{27}$$

Using either Eq. (22) or (25), it is found that

$$a = (2/3) l_D \tag{28}$$

(C) *Cylinder*

To determine the Newtonian pressures on a circular cylinder, consider an infinite circular cylinder in a flow which is inclined at an angle α to the longitudinal axis of the cylinder. In the case of a circular cylinder, it is evident that only the lower half of the cylindrical surface is exposed to the free stream (Case 2) and, therefore, that $\beta_u = 0$. Also, since $\theta = 0$ and $r = r_B = \text{const.} = r_S$ (the subscript S is used to denote cylinder) for a circular cylinder, it follows from Eq. (20) that

$$C_N' = (16/3\pi) \sin^2 \alpha \tag{29}$$

If l_S is used to denote the length of any portion of the infinite cylinder, the normal force coefficient is

$$C_N \equiv \frac{N}{q_0 \pi r_S} = \frac{16}{3\pi} \frac{l_S}{d_S} \sin^2 \alpha = \frac{5.33}{\pi} \frac{l_S}{d_S} \sin^2 \alpha \tag{30}$$

where N is the normal force on the cylinder length l_S. The axial force on the cylinder, of course, is zero. Also $(dC_N/d\alpha)_{\alpha=0}$ is zero.

When the effect of centrifugal forces as influenced by the boundary layer is considered in addition to the impact (Newtonian) forces, the normal force on the cylinder is reduced by 10 per cent (see Appendix). Thus Eqs. (29) and (30) become

$$C_N' = (4.8/\pi) \sin^2 \alpha \tag{31}$$

and

$$C_N = (4.8 l_S/\pi \, d_S) \sin^2 \alpha \tag{32}$$

The analysis, including centrifugal forces, indicates that such effects are smaller for conventional slender noses, such as cones and ogives at moderate angles of attack, and, thus, the pressure forces on such slender noses are satisfactorily approximated by the Newtonian (impact force) method. Consequently, the aerodynamic characteristics of a cone as given by Eqs. (22) through (28) are not modified.

(D) *The Cone and Cylinder Areas Situated in Expansion Flow*

All of the expressions (14) through (32) can be interpreted in two ways. For truly Newtonian conditions corresponding to $M_0 = \infty$, it was pointed out previously that $C_{p_e} = 0$ and $p_e/p_0 = 0$. In this case, Eqs. (14) through (32) give the total forces on the entire body, including the surfaces situated in expansion flow. If Eqs. (14) through (32) are considered as hypersonic approximations, they may be thought of as applying only to the forces on the surfaces in compression flow. In this case—as discussed in connection with Eqs. (12) and (13)—it is appropriate to consider a nonzero value for the pressure coefficient C_{p_e}, where

$$C_{p_e} = (2/\gamma M_0^2) [(p_e/p_0) - 1]$$

corresponding to the surface areas situated in expansion flow. Although C_{p_e} is certainly negligible at extremely high Mach Numbers, it would have to be given consideration in any attempt to extrapolate the hypersonic approximations down to lower Mach Numbers. In view of the extremely approximate nature of such a procedure, it would probably be sufficient to use an average value $\bar{p}_e$, which is independent of β but which may be different on the cone and on the cylinder.

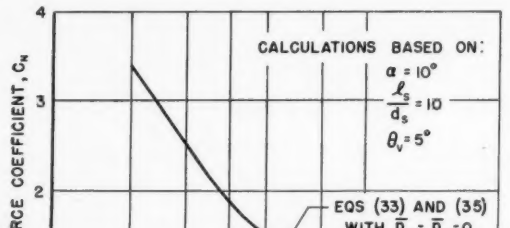
CALCULATIONS BASED ON:
α = 10°
$\frac{l_s}{d_s}$ = 10
θ_v = 5°
EQS (33) AND (35) WITH $\bar{p}_{e_D} = \bar{p}_{e_S} = 0$
BODY = CONE PLUS CYLINDER
EQS (25) AND (30)
NORMAL FORCE COEFFICIENT, C_N
MACH NUMBER, M_0

FIG. 6. Illustration of low Mach Number effect of expansion flow on the lift of a yawed body of revolution.

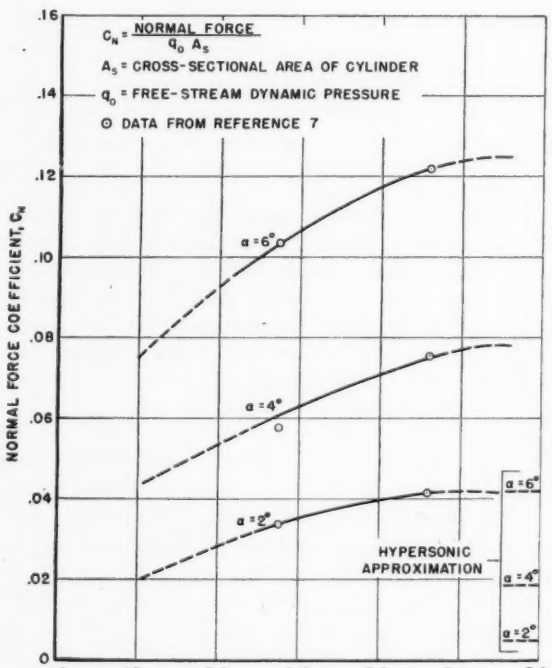

FIG. 7. Normal force coefficient for a circular cylinder situated behind an ogive—the German A4 missile.

(*1*) *Cone.*—If an average pressure is used, from Eq. (12) the normal force N_e on the expansion flow areas of the cone would be written

$$N_e = \frac{4q_0}{\gamma M_0^2}\left(1 - \frac{\bar{p}_{e_D}}{p_0}\right)\int^{l_D}\int_{\beta}^{\pi/2} r \sin\beta \, d\beta \, dx$$

where $\bar{p}_{e_D}$ is the average pressure on the shielded area of the cone and $\beta_u = \sin^{-1}(\tan\theta_v/\tan\alpha)$. The corresponding normal force coefficient C_{N_e} is

$$C_{N_e} = \frac{N_e}{q_0 \pi r_D^2} = \frac{2[1 - (\bar{p}_{e_D}/p_0)]}{\pi\gamma M_0^2}\sqrt{\cot^2\theta_v - \cot^2\alpha} \qquad (33)$$

Similarly, the axial coefficient is found to be

$$C_{X_e} = -\frac{2[(\bar{p}_{e_D}/p_0) - 1]}{\pi\gamma M_0^2}\left(\frac{\pi}{2} - \beta_u\right) \qquad (34)$$

(*2*) *Cylinder.*—For the cylinder (since $\beta_u = 0$, r = const., and it is assumed that $p = \bar{p}_e$ = const.), the result is

$$C_{N_e} = \frac{q_0 C_{p_e} l_S \, d_S}{q_0 \pi r_S^2} = \frac{4l_S}{\pi r_S}\frac{[(\bar{p}_{e_S}/p_0) - 1]}{\gamma M_0^2} \qquad (35)$$

In order to use these equations, approximate values for $\bar{p}_{e_D}$ and $\bar{p}_e$ must be estimated in any manner that appears feasible, possibly from two-dimensional gas dynamics and low aspect ratio supersonic wing theory. An indication of the maximum effect of the expansion pressures on the lift of a yawed body is obtained by putting $\bar{p}_{e_D} = \bar{p}_{e_S} = 0$. This is shown in Fig. 7 for a typical body. The actual lift (normal force) could be expected to be somewhere between the two curves shown in Fig. 6.

(III) The Correlation of Experimental Results for the Supersonic Lift on Bodies of Revolution

The previous discussions have been concerned entirely with approximate methods for predicting the lift of a body of revolution at hypersonic Mach Numbers of the order of 10 or 15 and above. Since it is important to have values of body lift throughout the complete Mach Number range, this still leaves the problem of estimating body lift at all lower Mach Numbers. Because of the lack of theoretical results applicable to this range of Mach Number ($2 < M_0 < 10$), a study has been made of available experimental data, and an attempt has been made to use the indications of these results to estimate (interpolate) the body lift in the intermediate range of Mach Number. For this purpose, use is made of the hypersonic approximation for the upper end of the Mach Number range. This procedure is admittedly almost qualitative in some respects, and it is expected that at least some of the results given here will have to be modified as more theoretical and experimental data become available.

The amount of available systematic supersonic experimental data for yawed bodies of revolution appears to be extremely limited. A survey of all supersonic data on yawed bodies of revolution shows that there exists no complete systematic series of tests (at least with data in usable form) in which body lift is determined as a function of angle of attack, Mach Number and body fineness ratio—particularly for varying lengths of cylinder behind the same nose shape. Except for the complete tests on the A4[7] and the Wasserfall,[8] there is a great scarcity of pressure distribution data for yawed bodies. This type of information is essential if significant comparisons are to be made with any theoretical results. Even for so simple a shape as a cone, there are but fragmentary pressure distribution

data for the yawed condition.[9] Moreover, most of the systematic experimental work in the past has been limited to body fineness ratios (l_B/d_B) of 7 or less.[10] The importance of tests on bodies of large fineness ratio lies in the indications of the discussion below that the lift on the cylindrical part of the body behind the nose not only becomes appreciable, Fig. 7, but also—at high enough speeds, Eq. (32)—the lift is directly proportional to the cylinder length and to the square of the angle of attack. While much is to be desired by way of experimental data, by using the hypersonic approximation as a guide together with available experimental results, it has been possible to obtain a rather consistent correlation for body lift over a wide range of conditions.

(A) *Lift on a Cylinder Following a Cone or Ogive*

From the close agreement in Fig. 1 between the hypersonic approximation and the Stone-Kopal values for cone lift, it is evident that the hypersonic-approximation values give a good approximation for cone lift even at low supersonic Mach Numbers. It is instructive to compare, at low Mach Numbers, the hypersonic approximation for cylinder lift with the experimental values for the lift on a cylinder following a cone or ogive. It is possible to extract some rather definite indications in this regard from the complete pressure distribution data for the German A4 missile at angle of attack.[9] The A4 body has an ogival nose followed by a straight cylindrical section that extends back to the beginning of the tail surfaces, beyond which there is a boat tail. If x is the distance measured from the forward tip of the nose and d_B denotes the maximum body diameter ($d_B = d_S$, the diameter of the cylindrical section), the straight cylindrical section extends from $x/d_B = 3.5$ to 6.0, giving a cylinder length of 2.5 cal.

The data in reference 7 give the local normal force coefficients C_N' as a function of position x/d_B along the body for a range of Mach Number and angle of attack. These local values of C_N' have been integrated over the cylinder section and give the cylinder lift values shown in Fig. 7. These results show that at supersonic speeds the cylindrical portion of a body contributes appreciable lift—which is rather strongly dependent on angle of attack and Mach Number and emphasizes the extremely poor approximation given by the slender body (zero-order) theory—which predicts zero lift on the cylinder, and by the linearized (first-order) theories that predict only limited cylinder lift. Fig. 7 also indicates that for low supersonic speeds the lift on the cylinder has already exceeded the hypersonic-approximation value and is increasing rapidly with Mach Number. At high enough Mach Numbers, yet to be determined, these curves must decrease to the hypersonic-approximation values. In view of the constant value of the normal force coefficient for a cone, for example, this suggests that the normal force coefficient for a cone plus cylinder body must go through a maximum with respect to Mach Number. It will be seen later that this is exactly what is indicated by the analysis of available experimental data.

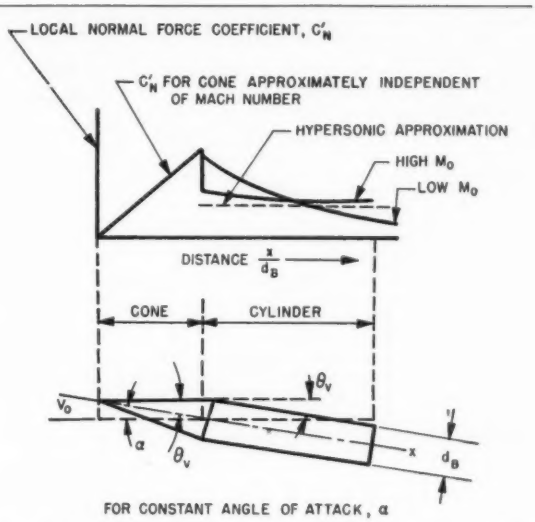

FIG. 8. Schematic diagram to illustrate the effect of increasing Mach Number on the distribution of C_N' along a cylindrical section behind a cone.

The qualitative notions concerning the lift distribution on a cylinder following an ogive are indicated by Fig. 8. At low supersonic Mach Numbers ($M_0 = 2$ to 3), the local normal force coefficient C_N' decreases with distance downstream along the axis of the cylinder but gives an integrated lift coefficient C_N greater than the hypersonic-approximation value. At some higher Mach Number, probably in the range $3 < M_0 < 6$, C_N reaches its highest value. At still higher Mach Numbers the variation of C_N' along the cylinder axis becomes smaller and smaller, approaching a constant condition, and C_N approaches the hypersonic-approximation value. The Mach Number at which the total body lift becomes approximately equal to the hypersonic-approximation value will be discussed below on the basis of the indications of the experimental data.

(B) *The Initial Normal Force Slope for Missiles with Cylindrical Afterbodies*

A typical missile body is shown schematically in Fig. 9. It consists of a diverging section (nose) of length l_D, which may be either a cone or an ogive; a straight (cylindrical section) of length l_S; and a converging (boat-tail) section of length l_C. The semivertex angle of the nose cone, or of the inscribed cone when the nose is ogival, is denoted by θ_v. The total body length is l_B, the maximum body diameter is d_B, the maximum cross-section area is $A_B = (\pi/4)d_B^2$, and the diameter of the base is d_b. All of the body aft of the nose, or forebody, may be referred to as the afterbody, and its length may be denoted by $l_A (= l_S + l_C)$. The afterbody may consist of all cylinder, part cylinder, and part boat tail, or all boat tail. In general, the vari-

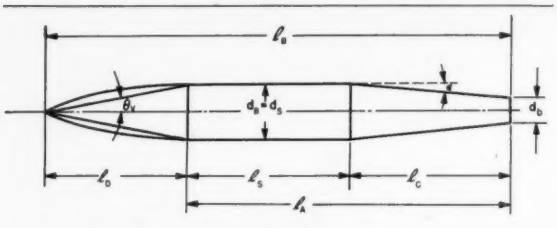
θ_v = SEMI-VERTEX ANGLE OF INSCRIBED CONE
d_B = MAXIMUM DIAMETER OF BODY
$A_B = \frac{\pi}{4} d_B^2$ = MAXIMUM CROSS SECTION AREA OF BODY
ϵ = BOATTAIL ANGLE
d_b = BASE DIAMETER
l_B = TOTAL LENGTH OF BODY
l_n = LENGTH OF NOSE, OR DIVERGING SECTION
l_s = LENGTH OF STRAIGHT OR CYLINDRICAL SECTION
l_c = LENGTH OF CONVERGING SECTION

FIG. 9. Diagram of typical missile body—schematic.

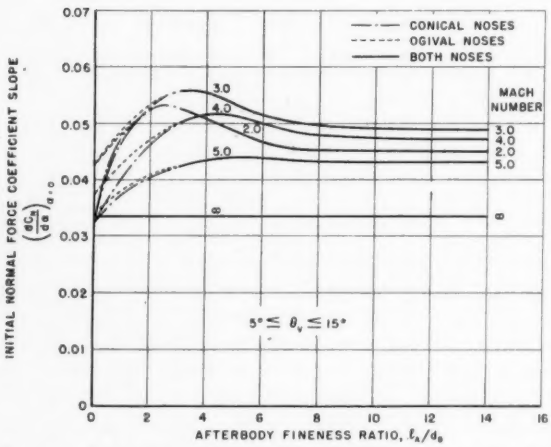

FIG. 10. Initial normal force slope for missiles with cylindrical afterbodies.

ables upon which the normal force coefficient will depend may be indicated by the relation

$$C_N \equiv \frac{\text{normal force}}{q_0 A_B} = \text{func.}\left(\theta_v, \frac{l_A}{d_B}, \frac{d_b}{d_B}, M_0, \alpha\right) \quad (36)$$

For the case in which the entire afterbody is cylindrical (no boat tail), it follows that $l_A = l_S$, $d_B = d_S$, and the dependency of C_N becomes

$$C_N \equiv \frac{\text{normal force}}{q_0 A_B} = \text{func.}\left(\theta_v, \frac{l_S}{d_S}, M_0, \alpha\right) \quad (37)$$

Since most of the available lift data are restricted to small angles of attack, such results are employed to greatest advantage when they are used to evaluate $(dC_N/d\alpha)_{\alpha=0}$. From Eq. (24) and Figs. 1 and 2, it appears that the normal force on the conical nose varies approximately as $\cos^2 \theta_v$, and this suggests use of the parameter $(dC_N/d\alpha)_{\alpha=0}/\cos^2 \theta_v$. However, most of the test data fall within the range $5° \leq \theta_v \leq 15°$, so the variation of $\cos^2 \theta_v$ from its median value is less than 4 per cent and within the accuracy of the experimental data. Furthermore, an investigation of the lift on the cylinder immediately following a cone (using yawed cone data and Prandtl-Meyer expansions) indicates that the cylinder lift may vary with cone semivertex angle so as to counteract the variation of cone lift with θ_v. For these reasons θ_v is eliminated and the experimental correlation is reduced to the form

$$(dC_N/d\alpha)_{\alpha=0} = \text{func.}\ (l_S/d_S, M_0) \quad (38)$$

This correlation has been carried out and yields the results* shown in Fig. 10. While the experimental points (not indicated) show considerable scatter, the correlation is sufficiently good to define individual curves for cone and ogive nose shapes and is considered fairly satisfactory, at least for preliminary purposes. It is found that when the length of the afterbody exceeds about 3 diameters (calibers), as far as total lift is concerned it makes little difference whether the nose is an ogive or a cone. At the lower Mach Numbers, the curves go through a maximum with respect to both afterbody fineness ratio and Mach Number. As l_S/d_S becomes large (> 9), the initial normal force slope becomes essentially independent of afterbody length. At the higher Mach Numbers, $M_0 > 9$, the initial slope becomes equal to that given by the hypersonic approximation for a cone. This follows from the fact that a cylindrical afterbody contributes nothing to the initial normal force slope in hypersonic flow [Eq. (30)]. At hypersonic speeds the ogive normal force is approximately equal to the normal force on its inscribed cone, as has been assumed in Fig. 10.

(C) *Additional Normal Force Resulting from Angle of Attack*

If the normal force curve slope were independent of α, the normal force could then be obtained immediately from Fig. 10. However, except for small angles of attack and missiles with no afterbody, the normal force is found to depart widely from a linear variation with α and to vary in a manner that is more nearly a quadratic function of α. This effect of angle of attack on normal force can be studied by introducing an increment in normal force coefficient, ΔC_N, defined by

$$C_N = (dC_N/d\alpha)_{\alpha=0} \times \alpha + \Delta C_N \quad (39)$$

This is illustrated in Fig. 11. Eq. (39) is the relation used to correlate angle-of-attack conditions, including the effects of Mach Number and afterbody length at angle of attack. It appears that, within the accuracy of the data, ΔC_N varies as $\sin^2 \alpha$; therefore, the results of the correlation are presented in the form $\Delta C_N \div$

* It will be noted that the abscissa in Fig. 10 is labeled l_A/d_B and therefore is not limited to missiles without boat tail. It is pointed out in Section (D) that the effect of boat tail may be accounted for as an increment in initial normal force slope (see Fig. 15) which must be added to the values obtained from Fig. 10. When there is no boat tail, $l_A/d_B = l_S/d_B$ and the values of Fig. 10 apply directly.

$\sin^2\alpha$. Before giving the results of this correlation, it is worth while to point out how the hypersonic approximations may be used to extrapolate from the limited range of conditions covered by the experimental results to conditions of higher Mach Number and angle of attack.

By using the experimental correlation results such as those of Figs. 10 and 11, it is possible to obtain experimentally based estimates of C_N up to $M_0 = 4$, over a range of values of l_S/d_S and α. These are shown by the left-hand end of the curves ($M_0 \leq 4.0$) in Figs. 12 and 13. At the high Mach Number end ($M_0 \approx 15$ or 20 and higher), we have the hypersonic-approximation values that are independent of Mach Number. As explained in Part (II-D), by extending the hypersonic approximation to lower Mach Numbers using $p_e = 0$ for the surfaces in expansion flow, an indication is obtained of the limits within which the actual value of C_N must lie. These limits are shown as curves 1 and 2 in Fig. 12, for example. Since there are no experimental data for $M_0 > 4.31$ and since most of the experimental data do not extend beyond $M_0 = 3$, these limit curves may be used as a guide for extending the low Mach Number range into the hypersonic range. This is the procedure that has been followed to obtain the results shown in Figs. 12 and 13. While this procedure

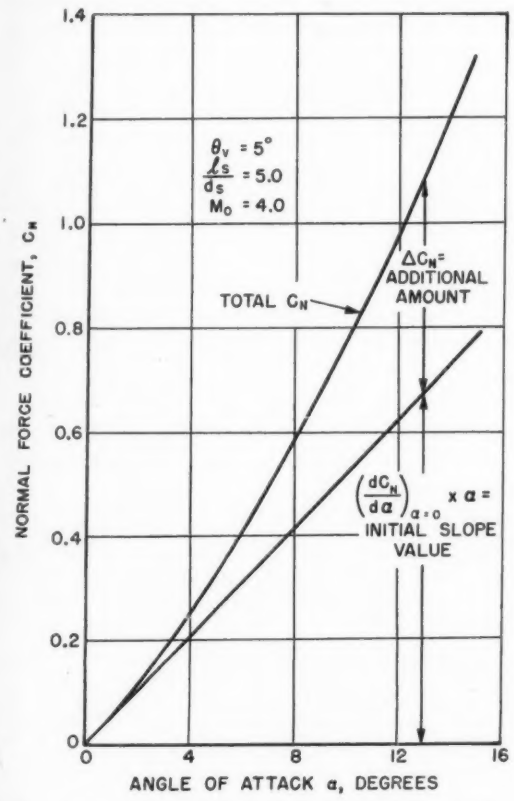

FIG. 11. Diagram to illustrate typical variation of normal force coefficient with angle of attack—schematic.

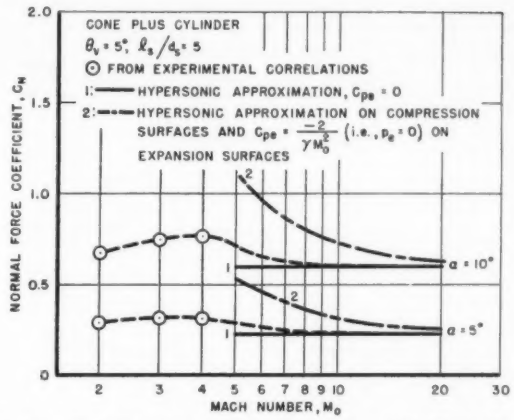
CONE PLUS CYLINDER
$\theta_V = 5°$, $l_S/d_S = 5$
FROM EXPERIMENTAL CORRELATIONS
1: HYPERSONIC APPROXIMATION, $C_{pe} = 0$
2: HYPERSONIC APPROXIMATION ON COMPRESSION SURFACES AND $C_{pe} = \frac{-2}{\gamma M_0^2}$ (i.e., $p_e = 0$) ON EXPANSION SURFACES
NORMAL FORCE COEFFICIENT, C_N
MACH NUMBER, M_0
α = 10°
α = 5°

FIG. 12. Variation of normal force coefficient with Mach Number and angle of attack.

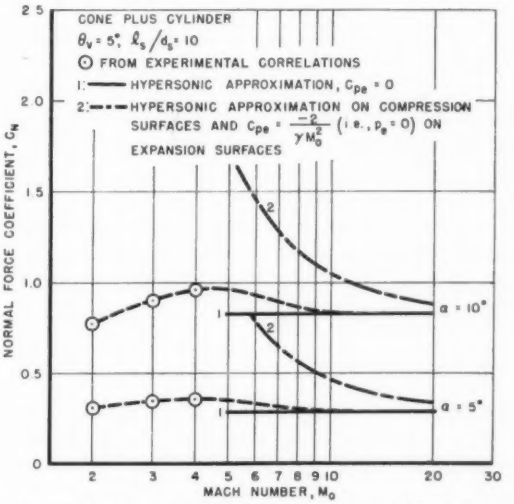
CONE PLUS CYLINDER
$\theta_V = 5°$, $l_S/d_S = 10$
FROM EXPERIMENTAL CORRELATIONS
1: HYPERSONIC APPROXIMATION, $C_{pe} = 0$
2: HYPERSONIC APPROXIMATION ON COMPRESSION SURFACES AND $C_{pe} = \frac{-2}{\gamma M_0^2}$ (i.e., $p_e = 0$) ON EXPANSION SURFACES
NORMAL FORCE COEFFICIENT, C_N
MACH NUMBER, M_0
α = 10°
α = 5°

FIG. 13. Variation of normal force coefficient with Mach Number and angle of attack.

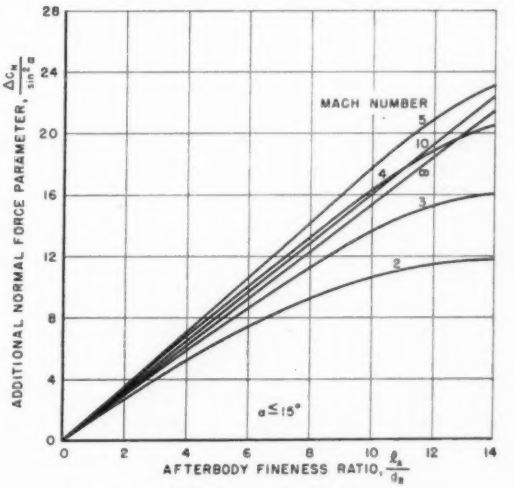

FIG. 14. Additional normal force parameter.

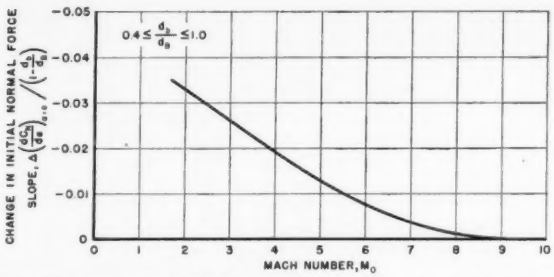

FIG. 15. Decrease in initial normal force slope due to boat tail.

admittedly contains certain elements of arbitrariness, it is believed to yield fairly realistic results and at least gives preliminary working values for lift over a range of conditions for which no other information exists.

By employing results of the type shown in Figs. 12 and 13, the correlated values of ΔC_N (Fig. 11) from test data have been extended into the hypersonic region as shown in Fig. 14. The hypersonic approximation for cones gives C_N as practically a linear function of angle of attack for the low-angle-of-attack range ($\alpha < 2\theta_c$) which is of most interest. The meager experimental cone data indicate that this is also true at low supersonic speeds. Thus, the additional normal force coefficient ΔC_N for a cone is zero, at least to the same degree of accuracy as can be expected from the experimental data. Consequently, it follows that the ΔC_N values in Fig. 14 refer to the cylinder only and, for $M_0 = \infty$, are given by Eq. (32).

(D) *Effect of Boat Tail*

A preliminary correlation of available data has shown the effect of boat tail on normal force to be limited to the initial normal force slope, $(dC_N/d\alpha)_{\alpha=0}$. No consistent, pronounced effect on the additional normal force, ΔC_N, was found within the angle-of-attack range of the tests ($\alpha \leq 10°$). It is likely, however, that data at higher angles of attack ($\alpha > 10°$) would show some effect of boat tail on ΔC_N. It appears that the initial normal force slope decreases linearly with decreasing base ratio, d_b/d_B, over the normal range of base ratios—$0.4 \leq d_b/d_B \leq 1.0$. The effects of boat-tail angle and type (conical or ogival) and the body preceding the boat tail appear to be small compared with the effect of the base ratio. The results of this correlation are shown by Fig. 15. It will be noted that the boat-tail effect is a maximum at low speeds and decreases to zero at about $M_0 = 9$. This is in agreement with the slender-body theories[11] that predict zero lift when $d_b/d_B = 0$ and with the hypersonic approximation that indicates no boat-tail effect on the initial slope parameter. It should be mentioned, however, that the hypersonic approximation would show an effect of boat tail on ΔC_N, since the boat-tail portion of the body would be completely shielded at angles of attack less than the boat-tail angle.

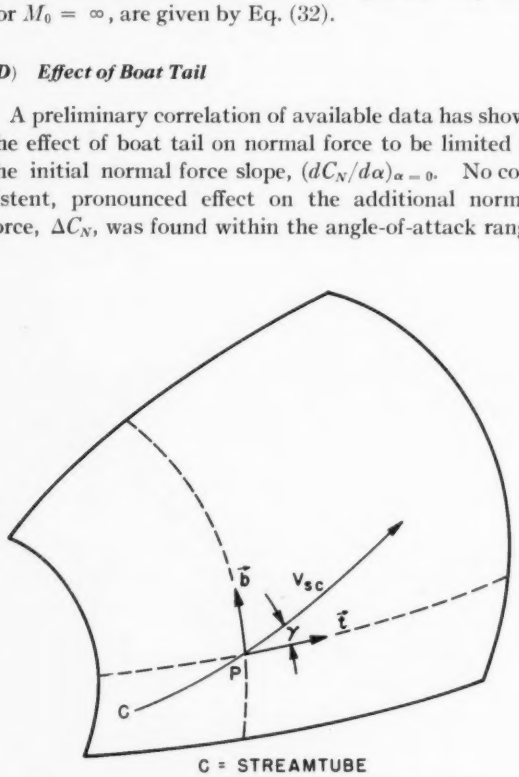

FIG. 16. Diagram of stream tube on surface of body.

(E) *Center of Pressure*

By using the normal forces that have been estimated for any cone-cylinder or ogive-cylinder combination, it is possible to estimate the corresponding center of pressure. Figs. 10 and 14 give the normal force on a cone or ogive and the normal force distribution along a cylinder following the cone or ogive. The center of pressure of the cone and ogive are approximately $0.67l_D$ and $0.53l_D$, respectively, aft of the nose. Fig. 15 gives the increment in normal force due to boat tail. It appears satisfactory to assume that this force acts at the midpoint of the boat tail. The location of the missile center of pressure aft of the nose tip, $x_{c.p.}$, is obtained by forming the summation of the various components according to the formula

$$x_{c.p.} = \sum C_{N_k} x_k / \sum C_{N_k} \tag{40}$$

Preliminary checks of this method have shown satisfactory agreement with experimental data.

Appendix

Analysis of the Centrifugal Force Effects

General Discussion

The simple analysis of Newtonian flow is incomplete inasmuch as the effects of centrifugal forces in the flow around the body have been neglected. In the flow over plane surfaces at angle of attack and on cones at zero angle of attack, since the paths of the air particles over such surfaces (that is, the stream lines on the surfaces) are straight lines, no centrifugal forces are present. However, when the surface stream lines are curved (as is the case for bodies of revolution at angle of attack, for example), centrifugal forces will be present in the flow. For these flow problems, the total

surface pressure coefficient at any point on the body is equal to the impact pressure coefficient minus the centrifugal pressure effect.[12, 13] If $C_{p_i} = (p_i - p_0)/q_0$ is the pressure coefficient due to the Newtonian impact pressure p_i and if p_c is the pressure relief due to centrifugal forces, then the net pressure coefficient C_p is, simply,

$$C_p = C_{p_i} - (p_c/q_0) = [(p_i - p_c) - p_0]/q_0 \quad (41)$$

where the net pressure p is specified by $p = p_i - p_c$. Also, when centrifugal forces are present, the limit angle β_u denotes the point of zero net pressure coefficient and not the point of zero impact pressure coefficient, as in the earlier discussion.

The Newtonian impact pressures are evaluated according to the methods given in Part (II). The pressure relief p_c resulting from centrifugal forces is evaluated from the formula

$$p_c = \dot{m} V_{s_c}/R\Delta C \quad (42)$$

where

$\dot{m}$ = rate of mass flow through a stream tube at any point on the surface
V_{s_c} = effective velocity in a stream tube at any point on the surface
R = radius of normal curvature of the stream tube at any point on the surface
ΔC = width of the stream tube (the height of stream tube is the body layer thickness described below)

In order to evaluate $\dot{m}$ and R for a body of revolution at angle of attack, the particle paths, or stream tubes, on the body surface must be determined. In the hypersonic approximation, the shock wave may be imagined to wrap itself around the portions of the body which are subject, or exposed, to compression flow. On these portions of the body, the flow is confined to a thin, high-density layer that lies on the surface of the body and which, therefore, may be referred to as "the body layer." Neglecting friction, the total reaction of the body-layer fluid on the surface and of the forces acting on the fluid must be normal to the surface. Hence, the principal normal (normal radius of curvature) and, therefore, the osculating plane at every point on a stream line must be normal to the surface. Thus, the stream tubes are similar to the geodesic paths obtained for the constrained motion of a particle on a curved surface.[14] At each point along a stream tube, the radius of curvature is directed along the inward normal to the surface—that is, along the vector $\boldsymbol{n}$. The rate of mass flow $\dot{m}$ at any point on a body-layer stream tube is obtained by finding the sum of all the particles that have previously entered the body layer along the particular stream tube.

Let the curve C, Fig. 16, denote a stream tube lying on the surface of the body, and let the radius of normal curvature of the stream tube at the point P on the surface be denoted by R. Let the lines of curvature at P have the directions given by the unit vectors $\boldsymbol{t}$ (maximum radius of normal curvature) and $\boldsymbol{b}$ (minimum radius of normal curvature), and let the curve C (that is, the stream tube) at this point make the angle γ with $\boldsymbol{t}$ (Fig. 16). According to Euler's theorem[15] it follows that

$$1/R = (\cos^2 \gamma)/R_1 + (\sin^2 \gamma)/R_2 \quad (43)$$

where R_1 is the radius of principal normal curvature in the $\boldsymbol{t}$ direction, and R_2, that in the $\boldsymbol{b}$ direction. For a body of revolution, which will be the case treated here, $\boldsymbol{t}$ is tangent to a meridian and $\boldsymbol{b}$ is tangent to a circular parallel; the meridians and parallels are the lines of curvature on the surface.[16] R_1 is the radius of curvature of the normal (meridian) section obtained by passing a plane normal to the surface and containing the axis of symmetry. R_1 is known immediately when the profile shape of the body of revolution is specified. R_2 may be determined by means of Meusnier's theorem (see page 505, reference 15), which shows that

$$R_2 = r/\cos \theta \quad (44)$$

where r is the radius of curvature of a circular parallel and θ is the angle between $\boldsymbol{n}$ and $\boldsymbol{r}$ (that is, θ is the direction of the tangent along a meridian). From Eqs. (43) and (44), it follows that

$$1/R = (\cos^2 \gamma)/R_1 + (\sin^2 \gamma \cos \theta)/r \quad (45)$$

is the relation for the radius of curvature of the stream line at any point on the surface of a body of revolution.

Consideration must next be given to the velocity V_{s_c} of the flow over the surfaces of the body which are exposed to compression flow. When a free-stream particle strikes the body layer at a local point P (see Fig. 16), it loses its component of velocity normal to the surface at this point, while the velocity components in the tangent plane remain unchanged. Letting η_n denote the angle between $\boldsymbol{V}_0$ and $\boldsymbol{n}$ [η_n is identical with η in Eq. (3)], it follows from Eq. (3) that

$$\cos \eta_n = \cos \alpha \sin \theta - \sin \alpha \cos \theta \sin \beta$$

The normal component of velocity $V_0 \cos \eta_n$ is lost upon impact, and the fluid particle after impact at the point P is left with the velocity components along $\boldsymbol{t}$ and $\boldsymbol{b}$ unchanged. If the angle between $\boldsymbol{V}_0$ and $\boldsymbol{t}$ is denoted by η_t and the angle between $\boldsymbol{V}_0$ and $\boldsymbol{b}$ by η_b, it follows from Eq. (3) that

$$\cos \eta_t = \cos \alpha \cos \theta + \sin \alpha \sin \theta \sin \beta \quad (46)$$

and

$$\cos \eta_b = \sin \alpha \cos \beta \quad (47)$$

After impact, the particle is left with the instantaneous velocity components $V_0 \cos \eta_t$ along $\boldsymbol{t}$ and $V_0 \cos \eta_b$ along $\boldsymbol{b}$. The resultant velocity vector is of magnitude

$$V_{s_t} = V_0(\cos^2 \eta_t + \cos^2 \eta_b)^{1/2} \quad (48)$$

It lies in the $\boldsymbol{tb}$-plane and makes the angle γ with the

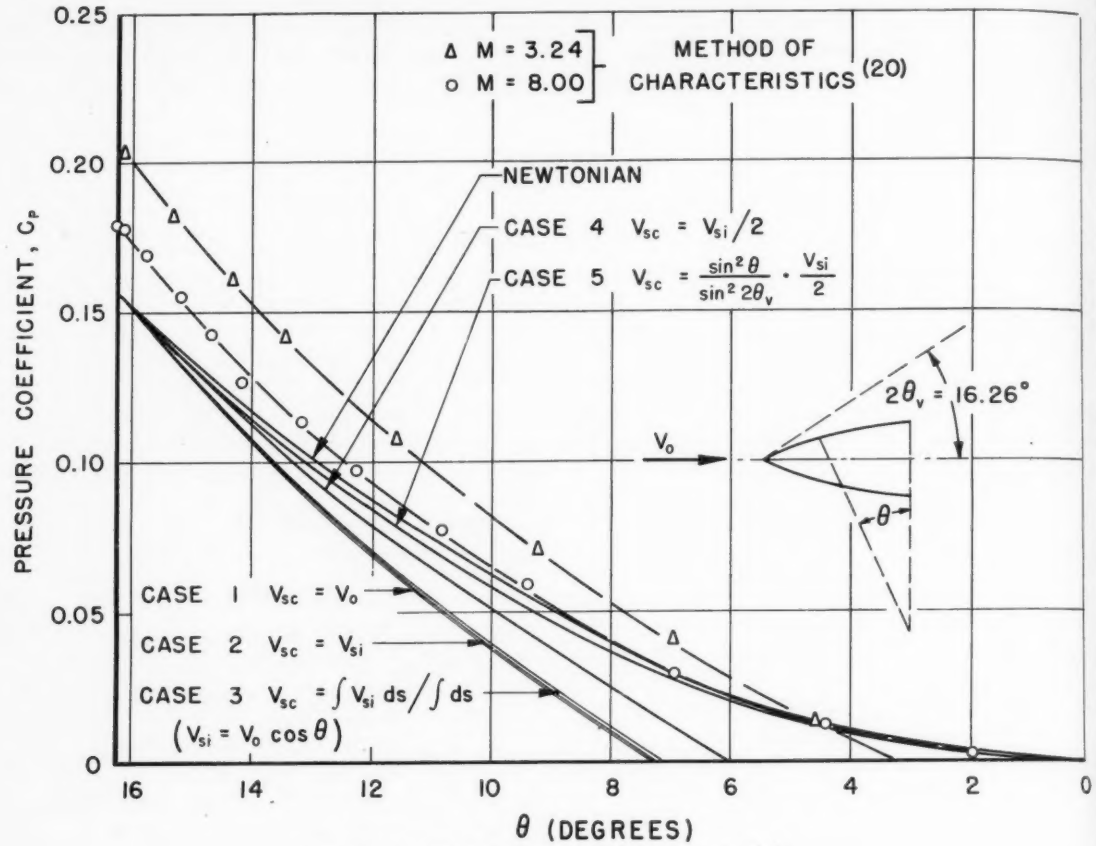

FIG. 17. Variation of pressure coefficient on nose of A4.

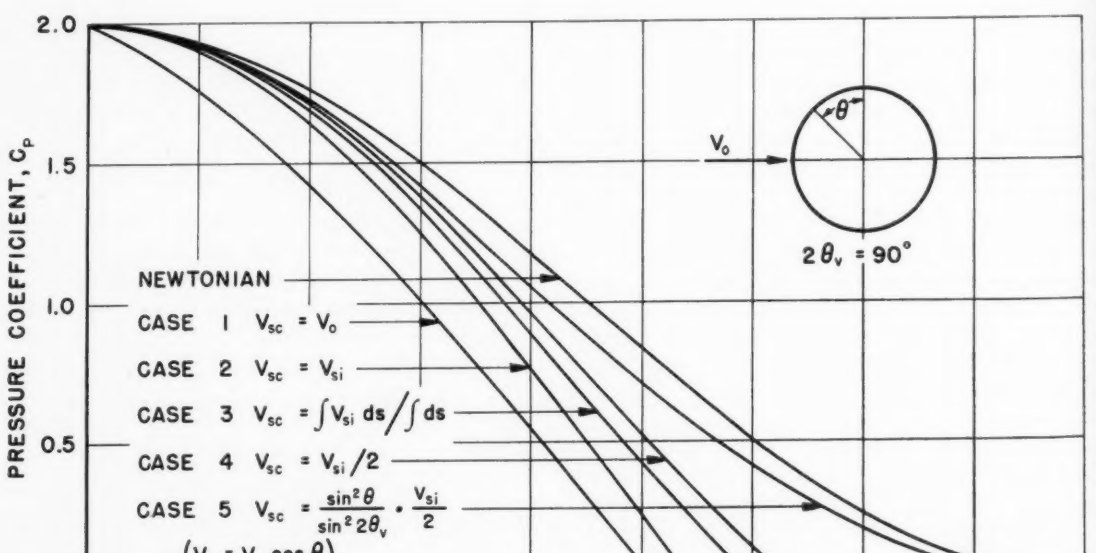

FIG. 18. Variation of pressure coefficient on a sphere.

vector $\boldsymbol{t}$, where

$$\cos \gamma = \frac{(V_0 \cos \eta_t)}{V_{s_t}} = \frac{1}{[1 + (\cos \eta_b / \cos \eta_t)^2]^{1/2}} \quad (49)$$

From the relation $\tan \gamma = \cos \eta_b / \cos \eta_t$, it follows that

$$\tan \gamma = 1/(\cot \alpha \cos \theta \sec \beta + \sin \theta \tan \beta) \quad (50)$$

Although a single particle after striking the body would continue its motion in the tangential plane formed by $\boldsymbol{t}$ and $\boldsymbol{b}$, the actual flow of a continuous medium constrains the particles to follow a stream tube on the surface. In order to evaluate the effective body-layer stream-tube velocity, V_{s_c}, a relationship must be found between V_{s_c} and V_{s_t} or V_0. Five postulations have been scrutinized.

Case 1. $V_{s_c} = V_0$: This is the most simple assumption and would overestimate the centrifugal force effects.

Case 2. $V_{s_c} = V_{s_t}$: This yields the result that each particle does accelerate along the body layer, but the postulation does not give a velocity gradient in the body layer at each point.

Case 3. $V_{s_c} = \int V_{s_t} dS / \int dS$: According to this method, the velocity of a particle remains constant after impact and results in the existence of a velocity gradient in the body layer.[12, 13, 17–19]

Case 4. $V_{s_c} = V_{s_t}/2$: This relation is the result of the assumption that the thickness of the body layer is of the order of magnitude of that of the boundary layer. The velocity distribution normal to the body surface is considered as a linear function of the distance from the surface throughout the body layer.

Case 5. $V_{s_c} = f(\theta, \beta, \alpha) V_{s_t}/2$: Upon examination of the pressure distribution as obtained by Sauer[20] using the method of characteristics for the A4 nose at Mach Numbers of 3.24 and 8.00 (see Fig. 17), it appears that the local pressure coefficient should decrease slower than any of the above four cases and that the location of zero pressure coefficient should occur at the position where the surface tangent is parallel to the free-stream direction. Since Case 4 yields reasonable pressure variation at the start of the body layer, it is used as a starting point for a fifth case. The present fifth case is then a modification of Case 4, where $f(\theta, \beta, \alpha)$ must be unity at the origin of the body layer, varies as a quadratic along the body layer, and approaches zero at the position where the surface tangent is parallel to the axis of the free stream. As an additional check on the validity of Case 5, all five cases are applied to flow over spheres (see Fig. 18). The aerodynamic drags are shown in Fig. 19 as the limiting values for the experimental data of Charters.[21] Since the skin friction and base drags for spheres at high velocities are negligibly small, Case 5 appears best.

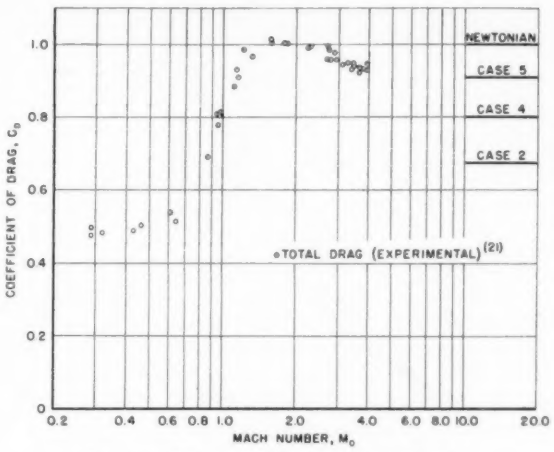

FIG. 19. The aerodynamic drag on spheres.

Example of Application—Cylinder, Case 5

The treatment of the hypersonic forces on a cylinder will be based on the assumption that the cylinder is infinite. In the case of an infinite cylinder, the surface stream lines are all parallel. This condition makes unnecessary the determination of the individual stream lines in the calculation of the centrifugal pressure effects. The rate of mass flow in the body layer at any particular position on the surface of the cylinder, where the centrifugal pressure is desired, is

$$\dot{m} = \rho_0 V_0 A_{cap} = \rho_0 V_0 r l_S \sin \alpha \cos \beta = \rho_B \delta_B V_{s_c} l_S \sin \gamma \quad (51)$$

where l_S is a specified length of the infinite cylinder. From Eq. (45), the radius of curvature R of a stream line on a cylinder is (since $R_1 = \infty$ and $\theta = 0$ for a cylinder)

$$R = r/\sin^2 \gamma \quad (52)$$

The expression for the centrifugal pressure at a point on a cylinder is

$$p_c = \dot{m} V_{s_c} / l_S R \sin \gamma \quad (53)$$

Combining Eqs. (51), (52), and (53), the centrifugal pressure relation may be written

$$p_c = \frac{\rho_0 V_0 r l_S \sin \alpha \cos \beta \sin^2 \gamma}{r l_S \sin \gamma} V_{s_c} =$$

$$\rho_0 V_0 V_{s_c} \sin \alpha \cos \beta \sin \gamma \quad (54)$$

Employing Case 5, the effective surface velocity for a cylinder is

$$V_{s_c} = (1/2) \sin^2 \beta \; V_0 \; (\cos \alpha / \cos \gamma) \quad (55)$$

since $V_{s_t} = V_0 (\cos \alpha / \cos \gamma)$ as given by Eq. (49). Now Eq. (54) may be written

$$p_c = \rho_0 V_0^2 \sin \alpha \cos \beta \sin \gamma (1/2) \sin^2 \beta \; (\cos \alpha / \cos \gamma) =$$

$$(1/2) \rho_0 V_0^2 \sin \alpha \cos \beta \sin^2 \beta \tan \gamma \cos \alpha \quad (56)$$

For a cylinder ($\theta = 0$), Eq. (50) yields

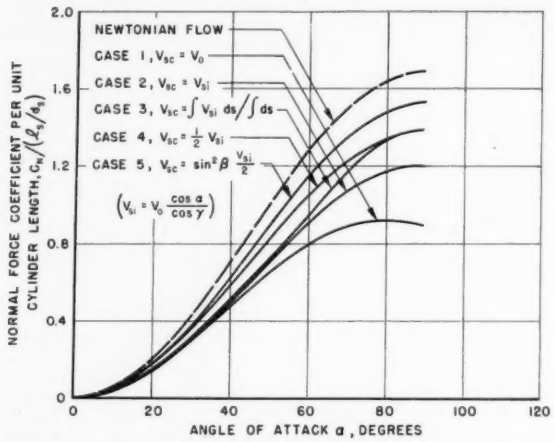

FIG. 20. Effect of V_{s_c} on the normal force for a cylinder.

$$\tan\gamma = \tan\alpha\cos\beta \tag{57}$$

and Eq. (56) becomes

$$p_c = (1/2)\rho_0 V_0^2 \sin^2\alpha\cos^2\beta\sin^2\beta = q_0 \sin^2\alpha\cos^2\beta\sin^2\beta \tag{58}$$

For a cylinder, the impact pressure coefficient given by Eq. (5) is

$$C_{p_i} = 2\sin^2\alpha\sin^2\beta \tag{59}$$

and the net pressure coefficient is

$$C_p \equiv C_{p_i} - (p_c/q_0) = \sin^2\beta\sin^2\alpha(2 - \cos^2\beta) \tag{60}$$

The equation defining β_u is $C_p = 0$, or $\sin^2\beta_u = 0$. Thus, for a cylinder, $\beta_u = 0°$ for all α.

From Eq. (6) the normal force coefficient corresponding to the surface of the cylinder exposed to compression flow is

$$C_N \equiv \frac{N}{q_0\pi {r_S}^2} = -\frac{2}{\pi}\frac{l_S}{r_S}\int_{-\pi/2}^{0} C_p \sin\beta\, d\beta = \frac{72}{15\pi}\frac{l_S}{d_S}\sin^2\alpha \tag{61}$$

where r_S is the cylinder radius and $d_S = 2r_S$ is the cylinder diameter. By comparing this result with Eq. (30) for the case in which the centrifugal forces are neglected it is found that

$$(C_N)_{\text{with centrifugal force}}/(C_N)_{\text{Newtonian}} = 0.900 \tag{62}$$

In Fig. 20, the effect of the various postulated V_{sc} on the normal force for a cylinder is given.

REFERENCES

[1] Stone, A. H., *On Supersonic Flow Past a Slightly Yawing Cone*, M.I.T. Journal of Mathematics and Physics, Vol. XXVII, No. 1, April, 1948.

[2] Kopal, Z. (Ed.), *Supersonic Flow Around Yawing Cones*, M.I.T. Center of Analysis Technical Report No. 3, 1947.

[3] Zahm, A. F., *Superaerodynamics*, J. Franklin Inst., Vol. 217, No. 2, p. 153, February, 1934.

[4] Epstein, P., *On the Air Resistance of Projectiles*, Proc. Nat. Acad. Sci., Vol. 17, No. 9, pp. 532–547, September, 1931.

[5] von Kármán, Th., *Isaac Newton and Aerodynamics*, Journal of the Aeronautical Sciences, Vol. 9, No. 14, p. 521, December, 1942.

[6] Laitone, E. V., *Exact and Approximate Solutions of Two-Dimensional Shock Flow*, Journal of the Aeronautical Sciences, Vol. 14, No. 1, p. 37, January, 1947.

[7] Erdmann, H., *Druckverteilungsmessungen am A4 VIP im Bereich der Unter- und Überschallgeschwindigkeiten*, Peenemünde Archiv Nr. 66/100.

[8] Herrman, E., *Druckverteilungsmessung am C2*, Peenemünde Archiv Nr. 66/136; *Vorläufiges Ergebnis der Druckverteilungsmessung am C2 des Projekts "Wasserfall,"* Peenemünde Archiv Nr. 66/146.

[9] Ferri, Antonio, *Supersonic-Tunnel Measurements on Missiles*, N.A.C.A. Wartime Report No. L-152, October, 1945.

[10] Walchner, O., *Systematic Wind-Tunnel Measurements on Missiles*, N.A.C.A. T.M. No. 1122, March, 1947.

[11] Munk, M. M., *The Aerodynamic Forces on Airship Hulls*, N.A.C.A. T.R. No. 184, 1923.

[12] Busemann, A., *Flüssigkeiten un Gasbewegung*, Handwörterbuch der Naturwissenschaften, Zweite Auflage, pp. 275–277, 1933.

[13] Ivey, H. R., Klunker, B. E., and Bowen, E. N., *A Method for Determining the Aerodynamic Characteristics of Two- and Three-Dimensional Shapes at Hypersonic Speeds*, N.A.C.A. T.N. No. 1613, July, 1948.

[14] MacMillan, W. D., *Theoretical Mechanics—Statics and Dynamics of a Particle*, pp. 329–335; McGraw-Hill Book Company, Inc., New York, 1927.

[15] Goursat, E., and Hedrick, E. R., *A Course in Mathematical Analysis*, Vol. 1, p. 501; Ginn and Company, Boston, 1904.

[16] Eisenhardt, L. F., *A Treatise on the Differential Geometry of Curves and Surfaces*, p. 126; Ginn and Company, Boston, 1909.

[17] Ivey, H. R., and Morrissette, R. R., *An Approximate Determination of the Lift of Slender Cylindrical Bodies and Wing-Body Combinations at Very High Supersonic Speeds*, N.A.C.A. T.N. No. 1740, October, 1948.

[18] Sänger, E., and Bredt, J., *Über einen Raketenatrieb für Fernbomber*, ZWB, UM Nr. 3538, Berlin, 1944. (Available as Navy Translation CGD-32, "A Rocket Drive for Long-Range Bombers.")

[19] Sänger, E., *The Prospects of Jet Reaction Flight*, Interavia, Vol. III, No. 10, October, 1948.

[20] Isenberg, J. S., *The Method of Characteristics in Compressible Flow, Part 1B*, Air Force A.M.C. Technical Report TR 1173C, December, 1947.

[21] Charters, A. C., *Some Ballistic Contributions to Aerodynamics*, Journal of the Aeronautical Sciences, Vol. 14, No. 3, p. 155, March, 1947.

The Longitudinal Stability of Elastic Swept Wings at Supersonic Speed

C. W. FRICK* AND R. S. CHUBB†

Ames Aeronautical Laboratory, N.A.C.A.

SUMMARY

The longitudinal stability characteristics of elastic swept wings experiencing bending and torsional deformations are calculated for supersonic speed by the application of linearized lifting-surface theory. A parabolic wing deflection curve is assumed, and the analysis is simplified by considering the wing panels to be simple cantilever beams. The method is thereby limited in application to wings of high aspect ratio for which the root effects are small. Expressions for the lift, pitching moment, and span load distribution are derived in terms of the elastic properties of the wing—namely, the design stress, the modulus of elasticity, the shearing modulus, and the maximum design load factor. The analysis applies to wings with leading edges swept behind the Mach lines. In all cases, however, the trailing edge is sonic or supersonic.

The validity of the assumption of a parabolic deflection curve is investigated by comparison with matrix calculations for a wing with the moment of inertia varying with the fourth power of the spanwise dimension. It is shown that for such wings the assumption of a parabolic deflection curve gives valid results for the wing stiffnesses and flight conditions in which the designer is primarily interested.

Calculations made for subsonic speed, when compared with the results for supersonic speed, indicate that, except for the effects of the change in the chordwise position of the section center of pressure, the aeroelastic characteristics are primarily a function of the flight dynamic pressure and not of Mach Number, at least for wings that have subsonic leading edges at all flight Mach Numbers.

INTRODUCTION

FOR THE PAST SEVERAL YEARS, the N.A.C.A. has been engaged in analytical studies of various wing-body combinations to determine their suitability for efficient supersonic flight. A great deal of this research has been concerned with wing-body combinations for which the wing is swept within the Mach cone. For such airplane configurations, Jones[1] has shown that lift-drag ratios of the order of 10 to 12 are possible at moderate supersonic speeds ($M = 1.1$ to 1.4).

In view of the promising flight efficiencies of swept wings, the analytical investigation was extended to include the stability characteristics of these wings. The changes in stability due to the elastic deformation of the wing, especially, were thought to be of major significance, since it was recognized that the structural weight penalty necessary to overcome these adverse aeroelastic effects might easily outweigh the aerodynamic advantages. The present investigation was therefore undertaken to provide estimates of the aerodynamic effects of the elastic deformation of the wing panels.

The analysis is concerned with aerodynamically efficient wings—that is, tapered swept wings of high aspect ratio with essentially elliptic span load distributions. For such wings of usual structural design, the ratio of the bending moment to the section moment of inertia is essentially constant spanwise so that the deflection curve is of parabolic form. The twist of streamwise sections therefore varies linearly across the span, and the aerodynamic loading due to the twist may be calculated by lifting-surface theory.

The extent of the present paper is limited to the treatment of longitudinal stability. Accelerated flight conditions only are investigated, since the longitudinal stability of the aircraft has greatest significance in dynamic flight.

SYMBOLS

x_1, y_1	=	Cartesian coordinates
x, y	=	transformed Cartesian coordinates in terms of the semispan dimension, s
ξ, η	=	x, y coordinates of the apex of any superposed lifting sector
s	=	distance in the y_1 direction from the root section to the intersection of the flexural axis and the tip Mach cone
s'	=	distance along the flexural axis from the root section to the intersection of the flexural axis and the tip Mach cone
y'	=	distance measured from the root section along the flexural axis
$\overline{Y}$	=	spanwise distance in y direction from the root section to the center of load on the half wing
S	=	wing area
λ	=	taper ratio, ratio of tip chord to root chord
$c_{av.}$	=	average chord
$\overline{c}$	=	mean aerodynamic chord ($\int c^2\,dy / \int c\,dy$)
c	=	local chord parallel to the plane of symmetry
c_0	=	root chord parallel to the plane of symmetry in terms of the span dimension, s
A.R.	=	aspect ratio
Λ	=	angle of sweepback of the flexural axis
θ	=	slope of the flexural axis in a vertical plane passing through the flexural axis
n	=	maximum load factor
M	=	bending moment at any point on the flexural axis
M_r	=	bending moment at the root section of the wing beam
T	=	torsional moment at any point on the flexural axis
T_r	=	torsional moment at the root section of the wing beam
E	=	modulus of elasticity for the wing-beam material

Presented at the Aerodynamics Session, Eighteenth Annual Meeting, I.A.S., New York, January 23–26, 1950.

* Head, 6- by 6-Ft. Supersonic Wind Tunnel Section.

† Aeronautical Research Scientist.

G = shearing modulus for the wing-beam material
I = moment of inertia of the wing beam
I_r = moment of inertia of the root section of the wing beam
J = torsional stiffness constant
J_r = torsional stiffness constant of the root section of the wing beam
ζ = distance between the flexural axis and the center of pressure of the sectional lift in terms of the local chord, positive if the flexural axis is behind the center of pressure
$\sigma_{max.}$ = maximum design stress
d_r = maximum thickness of the wing at the root section
α = angle of attack of the root section of the wing, rad.
α_T = incremental angle of attack at any spanwise station of the wing, rad.
α_s = angle of attack of the wing section at any spanwise station, rad.
α_n = angle of attack of the root section at which maximum load factor is developed, rad.
β = $\sqrt{M^2 - 1}$, where M is the free-stream Mach Number
m = β times the cotangent of the angle of sweepback of the wing leading edge
m_l = β times the cotangent of the angle of sweepback of the wing trailing edge
l = β times the cotangent of the angle of sweepback of a ray from the apex of any superposed lifting sector
Γ = complete elliptic integral of the first kind with modulus ($\sqrt{1 - m^2}$)
Σ = complete elliptic integral of the second kind with modulus ($\sqrt{1 - m^2}$)
W = airplane weight
W/S = wing loading
q = dynamic pressure [$(1/2)\rho V^2$], where ρ is the mass density and V the velocity of the free stream
$\Delta p/q$ = lifting pressure coefficient
l = load per unit span

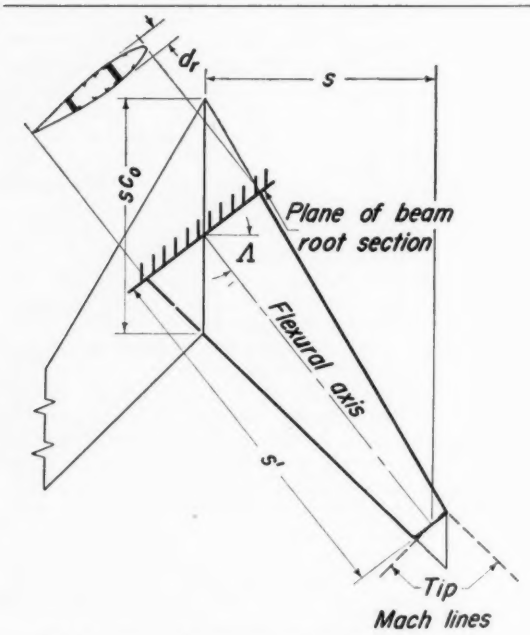

FIG. 1. Geometric characteristics of the wing beam.

L = lift
C_L = lift coefficient (L/qS)
C_{L_n} = lift coefficient at maximum load factor
m_s = section pitching moment of a wing section about the apex of the wing
C_m = pitching-moment coefficient about the apex of the wing in terms of the mean aerodynamic chord and the wing area
$C_{L\alpha}$ = the rate of change of lift coefficient with the angle of attack of the root section
C_{m_α} = the rate of change of pitching-moment coefficient with the angle of attack of the root section

ANALYSIS

Lifting-Surface Theory

For convenience, the aerodynamic effects of the bending deformation of the wing are considered first.*

Bending.—The bending deformation of a swept-wing beam differs somewhat from that calculated by the usual simple cantilever-beam theory used for unswept wings because of two differences in the wing structural characteristics:

(1) The swept-wing beam is restrained along a streamwise root section and not along a section perpendicular to the beam centerline.

(2) The swept-wing beam does not have a true flexural axis. The line of section torsional centers which usually defines the flexural axis has marked curvature near the root section.

For wings of high aspect ratio, however, the accuracy of the bending deformations calculated by simple beam theory is not greatly impaired by assuming a straight flexural axis exists coinciding with the straight portion of the line of section torsional centers. Further, for the purpose of analysis, as is shown in Fig. 1, the root section of the wing beam is assumed to be the section formed by extension of the wing-beam generators onto a plane perpendicular to the flexural axis and passing through the intersection of the flexural axis and the streamwise root section. This simplification of the beam analysis has some justification in recent experiments with swept-wing beams performed by Zender and Libove,[2] of the N.A.C.A. The length of the wing beam s' is taken as the distance along the flexural axis from the root section to the intersection of the flexural axis and the tip Mach cone. The semispan s of the wing is taken as extending from the root section to the intersection of the flexural axis and the tip Mach cone in a direction perpendicular to the plane of symmetry. The portion of the wing lying within the tip Mach cone is ignored, since, as has been shown by Cohen,[3] little load is carried in this region.

The coordinate system is selected as shown in Fig. 2. The origin of the coordinate system is placed at the apex of the wing, the positive branch of the x_1 axis lying downstream.

* The ameliorating influence of the distributed mass of the wing is not considered, and the change in camber of the airfoil sections due to the distortion of the wing surface is ignored.

The mathematical treatment may be made less tedious by transforming and nondimensionalizing the coordinates so that, in the following analysis,

$$y = \beta y_1/s, \quad x = x_1/s$$
$$c_0 = \text{root chord}/s$$

In general, at both subsonic and supersonic speeds, selection of the wing plan form for low drag leads to a combination of spanwise loading and spanwise distribution of the bending resistance in the wing beam such that the wing deflection curve is essentially parabolic; the ratio of the bending moment at any spanwise station to the moment of inertia at that station is constant across the span. The deflection curve deviates appreciably from a parabola only if the aeroelastic effects experienced by the wing are extremely large. Since the designer is primarily interested in wings for which the effects of the elastic deformations of the wing are small, it appears that the assumption of a parabolic deflection curve is admissible. This point will be developed further later in the analysis.

Assuming that the deflection curve of the flexural axis is parabolic, the slope of the flexural axis, as shown in Fig. 3, is

$$\theta = (M/EI)y'$$

where y' is measured along the flexural axis.

The incremental angle of attack of streamwise sections of the wing is related to the slope of the flexural axis as

$$\alpha_T = -\theta \sin \Lambda$$

The slope of the flexural axis in nondimensional transformed coordinates may be written as

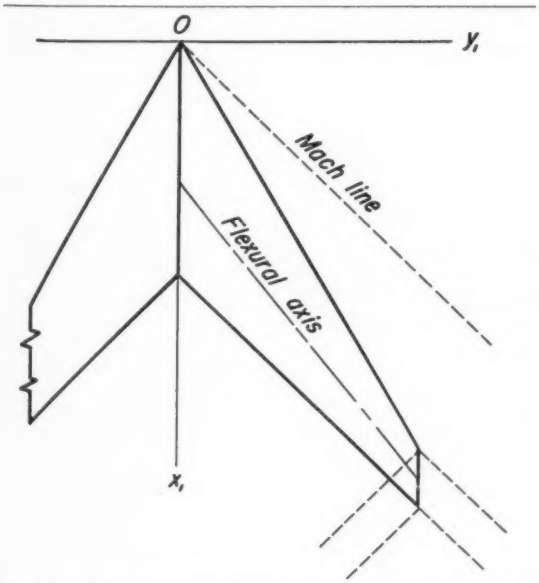

FIG. 2. Coordinate system for calculation of the characteristics of elastic wings.

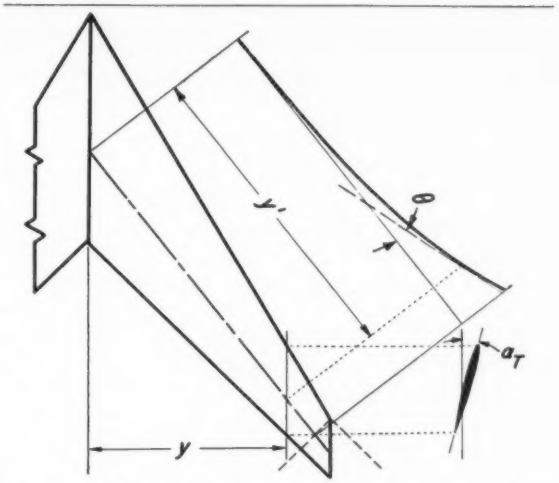

FIG. 3. Sketch of the deflection curve and angle of twist of the wing beam.

$$\theta = (M/EI)\ [s/(\beta \cos \Lambda)]y$$

The incremental angle of attack of any streamwise section of the elastic wing is then

$$\alpha_T = -(M/EI)\ (s/\beta)y \tan \Lambda$$

and the total angle of attack of any streamwise section is

$$\alpha_s = \alpha - (M/EI)\ (s/\beta)y \tan \Lambda \qquad (1)$$

where α is the angle of attack of the root section of the wing.

The distribution of pressure over the elastic wing due to twist may be determined by applying known conical-flow solutions for supersonic flow. In the linearized theory, the principle of superposition of various solutions may be used to satisfy the particular boundary conditions of the problem. For the elastic wing, the flow field may be considered to consist of the superposition of two distinct flow fields:

(1) The flow about a flat rigid wing at an angle of attack equal to the angle of attack of the root section.

(2) The flow about a twisted wing for which the angle of attack at the root is zero.

The solution for the first flow field is that given by Stewart[4] and Brown[5]; the second flow field can be obtained by determining the solution for a differential twist $d\alpha_s$ at one station and integrating this solution across the span.

The solution for the pressure distribution at any point, corresponding to a differential twist, must meet the following boundary conditions (Fig. 4):

(1) Outboard of the station of twist, the angle of attack must be constant and equal to the differential twist.

(2) Inboard of the station of twist, the angle of attack of the surface must be zero.

(3) Between the swept leading edge and the Mach cone, no lifting pressures may exist.

The conical-flow solution corresponding to these boundary conditions is that for a special lifting sector given by Lagerstrom[6] and is expressed in the notation of the present paper as

$$\frac{\Delta p}{q} = \frac{8\alpha}{\beta\pi} \frac{m^{3/2}}{(m+1)} \sqrt{\frac{1+t}{m-t}} \tag{2}$$

where t defines a ray from the apex of the sector. Fig. 4 shows both a sketch of the boundary conditions to be met by this solution and a plot of the pressure distribution given by Eq. (2).

The induced pressure resulting from twist due to bending of the elastic wing may be found by integrating across the span of the wing. This integration corresponds to the superposition of an infinite number of the lifting sectors along the span, each sector having an infinitesimal angle of attack $d\alpha_s$.

The pressure due to twist is then given by

$$\left(\frac{\Delta p}{q}\right)_T = -\frac{8}{\beta^2\pi} \frac{m^{3/2}}{(m+1)} \frac{Ms}{EI} \tan\Lambda \int_0^{\eta_0} \sqrt{\frac{1+t}{m-t}}\, d\eta$$

where

$$t = \frac{y-\eta}{x-\xi} = \frac{m(y-\eta)}{mx-\eta}$$

The x and y coordinates of the apex of any superposed sector are ξ, η.

The integration must be carried out from the root section of the wing $\eta = 0$ to the value of $\eta = \eta_0$ corresponding to the last superposed sector, the Mach cone of which encompasses the point x, y under consideration. The value of η_0 is found by placing t equal to -1 and solving for η.

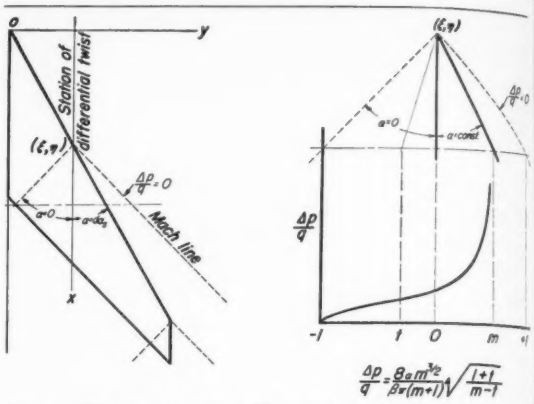

FIG. 4. The boundary conditions and pressure distribution for the conical-flow solution for differential twist.

$$\eta_0 = [m/(m+1)]\,(x+y)$$

The integration yields at any point x, y the pressure due to twist

$$\left(\frac{\Delta p}{q}\right)_T = -\frac{16}{3\beta^2\pi} \frac{m^{5/2}}{(m+1)^2} \tan\Lambda \frac{Ms}{EI} (x+y) \times \sqrt{\frac{x+y}{mx-y}} \tag{3}$$

To this expression must be added the conjugate term due to the elastic deformation of the opposite wing panel. The conjugate term may be obtained by substituting $-y$ for y. Then,

$$\left(\frac{\Delta p}{q}\right)_T = -\frac{16}{3\beta^2\pi} \frac{m^{5/2}}{(m+1)^2} \tan\Lambda \frac{Ms}{EI} \left[(x+y)\sqrt{\frac{x+y}{mx-y}} + (x-y)\sqrt{\frac{x-y}{mx+y}}\right] \tag{4}$$

It should be noted that the addition of the conjugate terms adds some small lifting pressure in the region between the wing leading edge and the Mach cone where no lifting pressure may exist. These pressures may be canceled by the superposition of constant lift sectors. Since these extraneous pressures, on the average, amount to about 3 per cent of the average pressure coefficient over the adjacent wing surface and since elimination of those pressures would change the pressures over the surface only about one-half of 1 per cent, it seems that, in view of the additional complication involved, the cancellation of these pressures is unwarranted.*

The total lifting pressure for the elastic wing at an angle of attack is then obtained by adding to Eq. (4) the solution for the flat lifting wing. For the elastic wing, then,

$$\frac{\Delta p}{q} = \frac{4m^2\alpha}{\beta\Sigma\sqrt{m^2(y/x)^2}} - \frac{16}{3\beta^2\pi} \frac{m^{5/2}}{(m+1)^2} \tan\Lambda \frac{Ms}{EI} \left[(x+y)\sqrt{\frac{x+y}{mx-y}} + (x-y)\sqrt{\frac{x-y}{mx+y}}\right] \tag{5}$$

* The authors have recently noted that an exact solution for the case of symmetric twist has been obtained by Theodore Goodman, of Cornell Aeronautical Laboratory (CAL/CM 524).

Examination of this equation shows that the relationship between M/EI and α must be established before the pressure distribution can be calculated. Since for wings with parabolic deflection curves the maximum stress occurs at the point of maximum thickness, usually the root, the maximum stress occurring at maximum load factor is

$$\sigma_{max.} = (M/I)_n(d_r/2)$$

and since the bending moment at any point on the span is a linear function of the angle of attack,

$$M/I = (2\sigma_{max.}/d_r)\ (\alpha/\alpha_n)$$

where $\sigma_{max.}$ is the design stress at maximum load factor, d_r is the thickness of the root section, and α_n is the angle of attack at maximum load factor; an expression for α_n is derived later.

The equation for the pressure distribution may then be written as

$$\frac{\Delta p}{q} = \frac{4m^2\alpha}{\beta\Sigma\sqrt{m^2 - (y/x)^2}} - \frac{32}{3\beta^2\pi}\frac{m^{5/2}}{(m+1)^2}\tan\Lambda\frac{\sigma_{max.}}{E}\frac{s}{d_r}\frac{\alpha}{\alpha_n}\left[(x+y)\sqrt{\frac{x+y}{mx-y}} + (x-y)\sqrt{\frac{x-y}{mx+y}}\right] \quad (6)$$

The load per unit span can be obtained from an integration of Eq. (6) with respect to x along any streamwise station (y = constant),

$$l/q = s\int_{y/m}^{(y+m_tc_0)/m_t} (\Delta p/q)_{y=const.}\, dx$$

The integration is carried out from the leading edge of the wing, $x = y/m$ to the trailing edge $x = (y + m_tc_0)/m_t$ and yields

$$\frac{l}{q} = \frac{4m^2s\alpha}{\beta\Sigma}f_1(y) - \frac{32}{3\beta^2\pi}\frac{m^{5/2}}{(m+1)^2}\tan\Lambda\frac{\sigma_{max.}}{E}\frac{s^2}{d_r}\frac{\alpha}{\alpha_n}f_2(y) \quad (7)$$

The functions $f_1(y)$ and $f_2(y)$ are given in the appendix since they are somewhat unwieldy.

The lift coefficient may be obtained by an integration of Eq. (7), spanwise from root to tip.

$$\beta C_L = (2s/S)\int_0^\beta (l/q)dy$$

The integration yields

$$\beta C_L = \frac{2s^2}{S}\left[\frac{4m^2\alpha}{\beta\Sigma}F_1 - \frac{32}{3\beta^2\pi}\frac{m^{5/2}}{(m+1)^2}\tan\Lambda\frac{\sigma_{max.}}{E}\frac{s}{d_r}\frac{\alpha}{\alpha_n}F_2\right] \quad (8)$$

The constants F_1 and F_2 are given by equations in the Appendix.

Eq. (8) may be used to determine the angle of attack at maximum load factor α_n which is needed in the foregoing equations:

$$\alpha_n = \frac{\beta^2\Sigma}{4m^2F_1}\left[\frac{S}{2s^2}C_{L_n} + \frac{32}{3\beta^3\pi}\frac{m^{5/2}}{(m+1)^2}\tan\Lambda\frac{\sigma_{max.}}{E}\frac{s}{d_r}F_2\right] \quad (9)$$

The pitching-moment characteristics of the elastic wing may be determined by an integration of the pressure distribution given by Eq. (6).

For any spanwise station, the section pitching moment about the apex of the wing is

$$m_s/q = -s^2\int_{y/m}^{(y+m_tc_0)/m_t} (\Delta p/q)_{y=const.}\, x\, dx$$

This integration yields

$$\frac{m_s}{q} = -s^2\left[\frac{4m^2\alpha}{\beta\Sigma}f_3(y) - \frac{32}{3\beta^2\pi}\frac{m^{5/2}}{(m+1)^2}\tan\Lambda\frac{\sigma_{max.}}{E}\frac{s}{d_r}\frac{\alpha}{\alpha_n}f_4(y)\right] \quad (10)$$

The functions $f_3(y)$ and $f_4(y)$ are given in the Appendix.

The total pitching-moment coefficient about the apex of the wing in terms of the mean aerodynamic chord is found by integration across the span,

$$\beta C_m = (2s/S\bar{c})\int_0^\beta (m_s/q)\, dy$$

$$\beta C_m = -\frac{2}{S}\frac{s^3}{\bar{c}}\left[\frac{4m^2\alpha}{\beta\Sigma}F_3 - \frac{32}{3\beta^2\pi}\frac{m^{5/2}}{(m+1)^2}\tan\Lambda\frac{\sigma_{max.}}{E}\frac{s}{d_r}\frac{\alpha}{\alpha_n}F_4\right] \quad (11)$$

or

$$\beta C_{m_\alpha} = -\frac{2}{S}\frac{s^3}{\bar{c}}\left[\frac{4m^2F_3}{\beta\Sigma} - \frac{32}{3\beta^2\pi}\frac{m^{5/2}}{(m+1)^2}\tan\Lambda\frac{\sigma_{max.}}{E}\frac{s}{d_r}\frac{F_4}{\alpha_n}\right] \quad (12)$$

The constants F_3 and F_4, functions of the aspect ratio, taper, and sweepback, are given in the Appendix.

Torsion.—The previous analysis has ignored the effects of wing twist due to torsion. The solutions obtained are, in reality, those for wings of infinite torsional stiffness. For wings having large angles of sweepback such as are necessary for efficient supersonic flight, the aerodynamic twist due to torsion has been calculated to be about 15 to 20 per cent of the twist due to bending (for thin wings). In such cases, the effect of the torsional deformation on the spanwise loading may be neglected *in calculating the torsional moment.* Eq. (7) may be utilized in the calculation of the torsional moment in this instance.

An expression for the torsional moment at the root section of the wing beam (perpendicular to the elastic axis) may be obtained by assuming that the distance from the center of pressure to the flexural axis for any section of the wing is a constant percentage of the local chord. Then,

$$\beta\frac{T_r}{q} = s\zeta\cos\Lambda\int_0^\beta\frac{l}{q}c\,dy$$

where c is the local streamwise chord given by the equation

$$c = sc_0\left[1-(1-\lambda)(y/\beta)\right]$$

where λ denotes the taper ratio of the wing and ζ is the distance from center of pressure to the flexural axis in terms of the streamwise chord. The function describing the spanwise loading l/q is given by Eq. (7).

The equation for the torsional moment at the root may be written as

$$\beta\frac{T}{q} = s^2\zeta c_0\cos\Lambda\int_0^\beta\frac{l}{q}\left[1-(1-\lambda)\frac{y}{\beta}\right]dy$$

$$\beta\frac{T_r}{q} = s^2\zeta c_0\cos\Lambda\left[\int_0^\beta\frac{l}{q}dy - \frac{1}{\beta}(1-\lambda)\int_0^\beta\frac{l}{q}y\,dy\right]$$

As will be shown later, it is convenient to derive the ratio of the torsional moment at the root to the bending moment at the root. The bending moment at the root is given as

$$\beta\frac{M_r}{q} = \frac{s^2}{\beta\cos\Lambda}\int_0^\beta\frac{l}{q}y\,dy$$

and

$$T_r/M_r = \zeta c_0[(\beta/Y) - (1-\lambda)]\cos^2\Lambda \quad (13)$$

where

$$\bar{Y} = \int_0^\beta\frac{l}{q}y\,dy\Big/\int_0^\beta\frac{l}{q}dy$$

and corresponds to the spanwise center of pressure for the load on the half wing. The value of $\bar{Y}$ may be determined by a graphical or analytical integration of Eq. (7).

When the assumption is made that the twist due to torsion varies linearly across the span (or that the ratio T/GJ is constant across the span), the incremental angle of attack of any section of the wing due to torsional deflection may be written as

$$\alpha_T = \frac{\cos\Lambda}{\beta}\frac{TS'}{GJ}y = \frac{Ts}{GJ}\frac{y}{\beta}$$

or

$$\alpha_T = \frac{Ms}{EI}\frac{y}{\beta}\left(\frac{T_rI_rE}{M_rJ_rG}\right)$$

and by adding this expression to the angle of twist due to bending [Eq. (1)], the total angle of twist of any section is

$$\alpha_s = \alpha - \frac{Ms}{EI}\frac{y}{\beta}\left[\tan\Lambda - \left(\frac{I_rE}{J_rG}\right)\frac{T_r}{M_r}\right] \quad (14a)$$

or

$$\alpha_s = \alpha - 2\frac{s}{d_r}\frac{\sigma_{max.}}{E}\frac{\alpha}{\alpha_n}\frac{y}{\beta}\left[\tan\Lambda - \left(\frac{I_rE}{J_rG}\right)\frac{T_r}{M_r}\right] \quad (14b)$$

Combined Bending and Torsion.—Expressions for the aerodynamic properties of swept wings experiencing both bending and torsional deformation may be obtained from Eqs. (6) to (12) if $\tan\Lambda$ is replaced by

$$[\tan\Lambda - (I_rE/J_rG)(T_r/M_r)]$$

The equation for the angle of attack at maximum load factor for combined bending and torsion is, then,

$$\alpha_n = \frac{\beta^2\Sigma}{4m^2F_1}\left\{\frac{S}{2s^2}C_{L_n} + \frac{32}{3\beta^3\pi}\frac{m^{5/2}}{(m+1)^2}\frac{\sigma_{max.}}{E}\frac{s}{d_r}\left[\tan\Lambda - \left(\frac{I_rE}{J_rG}\right)\frac{T_r}{M_r}\right]F_2\right\} \quad (15)$$

where

$$T_r/M_r = \zeta c_0[(\beta/\bar{Y}) - (1 - \lambda)] \cos^2 \Lambda$$

In applying the foregoing analysis to a specific wing, it is convenient to use the equations to obtain the ratio of C_{m_α} or C_{L_α} for the elastic wing to the value for the rigid wing. Multiplying this ratio by the value of C_{L_α} or C_{m_α} for the rigid wing, as determined by the complete theory wherein the region within the Mach cone of the tip, etc., is considered, will then give more accurate parameters for the elastic wing. Then,

$$\frac{l}{q\alpha} = \frac{4m^2 s}{\beta\Sigma} f_1(y) - \frac{32}{3\beta^2\pi} \frac{m^{5/2}}{(m+1)^2} \frac{\sigma_{max.}}{E} \frac{s^2}{d_r} \frac{f_2(y)}{\alpha_n} \left[\tan \Lambda - \left(\frac{I_r E}{J_r G}\right) \frac{T_r}{M_r}\right] \tag{16}$$

$$\frac{C_{L_{\alpha_{\text{elastic}}}}}{C_{L_{\alpha_{\text{rigid}}}}} = 1 - \frac{8}{3} \frac{\Sigma \sqrt{m}}{\beta\pi(m+1)^2} \frac{\sigma_{max.}}{E} \frac{s}{d_r \alpha_n} \left[\tan \Lambda - \left(\frac{I_r E}{J_r G}\right) \frac{T_r}{M_r}\right] \frac{F_2}{F_1} \tag{17}$$

$$\frac{C_{m_{\alpha_{\text{elastic}}}}}{C_{m_{\alpha_{\text{rigid}}}}} = 1 - \frac{8}{3} \frac{\Sigma \sqrt{m}}{\beta\pi(m+1)^2} \frac{\sigma_{max.}}{E} \frac{s}{d_r \alpha_n} \left[\tan \Lambda - \left(\frac{I_r E}{J_r G}\right) \frac{T_r}{M_r}\right] \frac{F_4}{F_3} \tag{18}$$

In using the preceding equations, it is necessary to solve for α_n. This, in turn, involves finding the ratio T_r/M_r, which is determined by the parameter $\bar{Y}$ (usually has a value of about 0.40).

A solution of the combined bending and torsional deformation effects can be obtained by assuming a value of $\bar{Y}$, solving for α_n, and checking the value of $\bar{Y}$ from a moment and area integration of a plot of Eq. (16) to see whether a second approximation is required to determine α_n more accurately.

The previous equations apply primarily to flat lifting wings or to twisted and cambered wings for which the loading due to twist and camber is the same essentially as the loading due to change in angle of attack. For wings with somewhat arbitrary camber and/or twist, these equations apply to all accelerated flight conditions. A solution for the aeroelastic characteristics in steady level flight for such wings must involve a consideration of the effects of the loading due to the known arbitrary twist.

Strip Theory

It is of interest to compare the results of the foregoing analysis, which utilizes lifting surface theory for the aerodynamic load calculations, with analytical results that more carefully consider the structural characteristics of the wing. Such a comparison involves the development of a strip theory of good accuracy which may be used in matrix calculations. One form of strip theory may be derived by using the basic loading for a flat swept wing at an angle of attack. The load at any spanwise station produced by an angle-of-attack change for that station is assumed equivalent to the load produced at that station by the same angle-of-attack change for the entire wing. The expression for the load may be written as

$$l/q\alpha = (4m^2 s/\beta\Sigma) f_1(y)[1 + (\alpha_r/\alpha)] \tag{19}$$

Comparisons of the load so computed with lifting-surface theory show that this form of strip theory is not of sufficient accuracy.

It is known from recent work by Brown and Adams[7] that a form of strip theory similar to that given by Eq. (19) gives the correct load distribution for wings with asymmetric linear twist. In the present case, symmetric linear twist is involved, but, since the mutual interference of the two wing panels is small, it appears

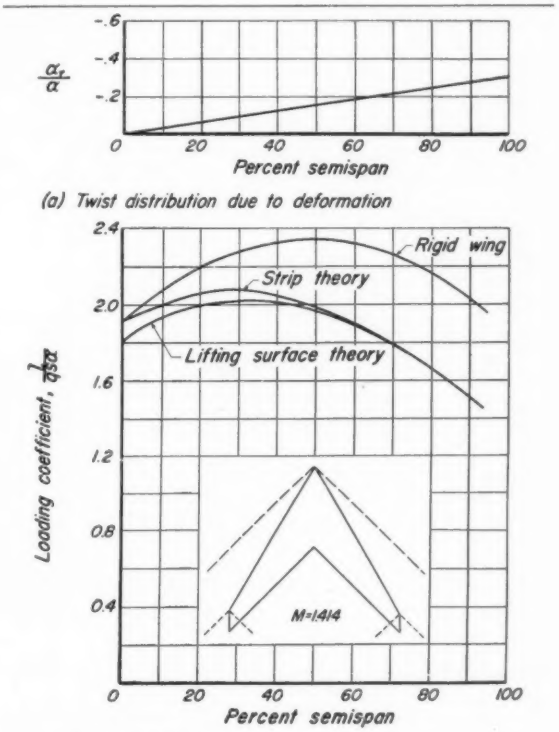

FIG. 5. Comparison of the load distributions as given by strip theory and lifting-surface theory for a wing with parabolic deflection curve.

that the strip theory resulting from Brown and Adams' work may prove satisfactory for aeroelastic calculations.* The expression for the load at any spanwise station is given as

$$\frac{l}{q\alpha} = \frac{4m^2 s}{\beta\Sigma} f_1(y) \left[1 + \frac{\Sigma}{\left(\frac{2 - m^2}{1 - m^2}\Sigma - \frac{m^2}{1 - m^2}\Gamma \right)} \frac{\alpha_T}{\alpha} \right] \tag{20}$$

A comparison of the loading given by Eq. (20) for a wing with a parabolic deflection curve with the loading for the same wing derived from lifting-surface theory is given in Fig. 5 for a Mach Number of 1.414. The spanwise twist distribution corresponding to the parabolic deflection curve is shown in part (a) of the figure. The loading for a flat wing is also shown. The same comparison is made in Fig. 6 for a cubic deflection curve. In both cases, the strip theory gives a close approximation to lifting-surface theory. Since the deflection curve of most wings can be closely approximated by suitable superposition of segments of parabolic and cubic arcs, it appears that this form of strip theory should be of sufficient accuracy.

If this simplified form of aerodynamic loading is utilized, Eqs. (15) to (18), which are based on lifting-surface theory, may be rewritten as

* The work of Goodman of Cornell cited in a previous footnote can be used to develop a similar strip theory that the authors have found possesses equal accuracy.

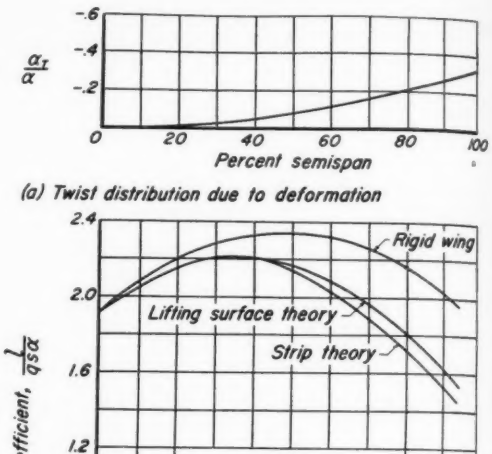

FIG. 6. Comparison of the load distributions as given by strip theory and lifting-surface theory for a wing with cubic deflection curve.

$$\frac{l}{q\alpha} = \frac{4m^2 s f_1(y)}{\beta\Sigma} \left\{ 1 - \frac{2s\sigma_{max.}}{\beta d_r E \alpha_n} y \left[\frac{\Sigma}{\left(\frac{2 - m^2}{1 - m^2}\Sigma - \frac{m^2}{1 - m^2}\Gamma \right)} \right] \left[\tan\Lambda - \left(\frac{I_r E}{J_r G} \right) \frac{T_r}{M_r} \right] \right\} \tag{21}$$

$$\alpha_n = \frac{\beta^2\Sigma}{4m^2 F_1} \left\{ \frac{S}{2s^2} C_{L_n} + \frac{8m^2}{\beta^3\Sigma} \frac{s}{d_r} \frac{\sigma_{max.}}{E} \left[\frac{\Sigma}{\left(\frac{2 - m^2}{1 - m^2}\Sigma - \frac{m^2}{1 - m^2}\Gamma \right)} \right] \left[\tan\Lambda - \left(\frac{I_r E}{J_r G} \right) \frac{T_r}{M_r} \right] F_5 \right\} \tag{22}$$

$$\frac{C_{L_{\alpha_{elastic}}}}{C_{L_{\alpha_{rigid}}}} = 1 - \frac{2}{\beta} \frac{s}{d_r} \frac{\sigma_{max.}}{E\alpha_n} \left[\frac{\Sigma}{\left(\frac{2 - m^2}{1 - m^2}\Sigma - \frac{m^2}{1 - m^2}\Gamma \right)} \right] \left[\tan\Lambda - \left(\frac{I_r E}{J_r G} \right) \frac{T_r}{M_r} \right] \frac{F_5}{F_1} \tag{23}$$

$$\frac{C_{m_{\alpha_{elastic}}}}{C_{m_{\alpha_{rigid}}}} = 1 - \frac{2}{\beta} \frac{s}{d_r} \frac{\sigma_{max.}}{\alpha_n} \left[\frac{\Sigma}{\left(\frac{2 - m^2}{1 - m^2}\Sigma - \frac{m^2}{1 - m^2}\Gamma \right)} \right] \left[\tan\Lambda - \left(\frac{I_r E}{J_r G} \right) \frac{T_r}{M_r} \right] \frac{F_6}{F_3} \tag{24}$$

The constants F_5 and F_6 are given in the Appendix.

Matrix Calculations

In order to investigate the validity of assuming that the wing deflection curve is parabolic, calculations were made utilizing strip theory with the matrix methods of a recent paper by Diederich,[8] of the N.A.C.A. In these calculations, it was assumed that the section moment of inertia of the wing beam varied with the fourth power of the spanwise dimension so that

$$I = I_r \left[1 - (1 - \lambda)(y_1/s) \right]^4$$

and that the torsional stiffness constant was directly

related to the bending moment of inertia of the wing beam as

$$J = (3/2)I$$

The geometric and structural characteristics of the swept wing of Fig. 7 were used in the analysis.

The results of the calculations are shown in Fig. 8. In part (a) of Fig. 8, the ratio of the lift-curve slope of the elastic wing to that of a rigid wing of the same plan form is shown as a function of the dynamic pressure. In part (b) of Fig. 8, the shift in the neutral point as a function of the dynamic pressure is given. A comparison is made between the aeroelastic characteristics as calculated by:

(1) Strip theory with matrix calculations for the wing with the moment of inertia varying as the fourth power of the spanwise dimension.

(2) Lifting-surface theory with the deflection curve assumed to be of parabolic shape.

(3) Strip theory with the deflection curve assumed to be of parabolic shape.

For the comparison of this figure, the calculations for all three cases were based on the same maximum design stress at the root section, and the effects of torsional deformation were not included. The results show that the assumption of a parabolic deflection curve gives reasonable results for all dynamic pressures up to a value for which the loss in lift-curve slope amounts to 40 per cent.

When the effects of both bending and torsional deformation are considered, the results shown in Fig. 9 are obtained. Matrix calculations that treat torsional effects more accurately give essentially the same result as the analysis of the present paper. It is evident, therefore, that, for the types of wings considered, the assumption of a parabolic deflection curve gives a reasonable estimate of the longitudinal stability characteristics.

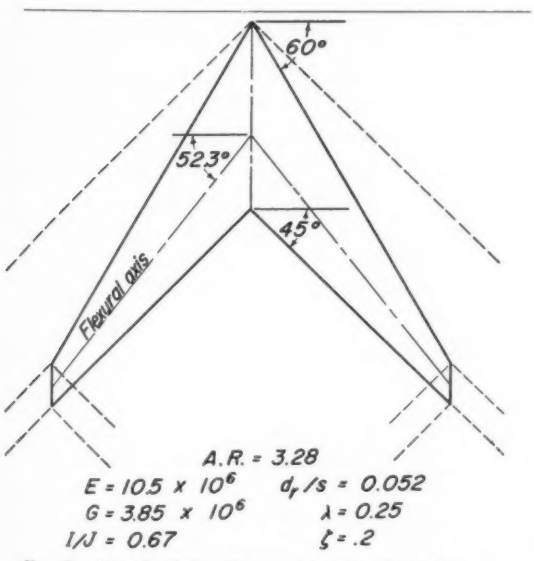

FIG. 7. Sketch of the wing used in the calculations.

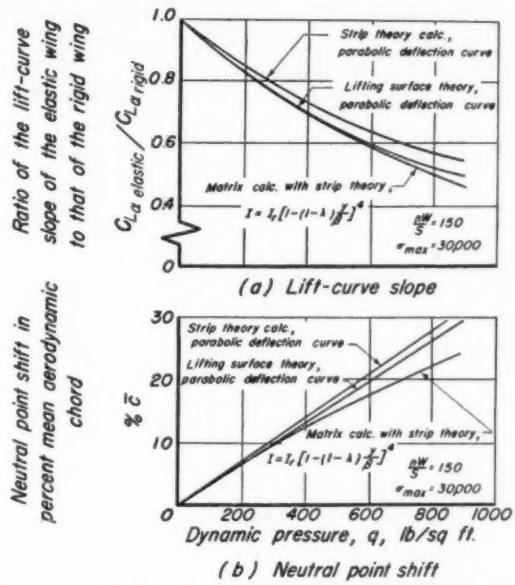
Ratio of the lift-curve slope of the elastic wing to that of the rigid wing
C_L_α elastic / C_L_α rigid
Strip theory calc., parabolic deflection curve
Lifting surface theory, parabolic deflection curve
Matrix calc. with strip theory, I = I_r[1-(1-λ)(r/s)^4]
nW/S = 150
σ_max = 30,000
(a) Lift-curve slope
Neutral point shift in percent mean aerodynamic chord
% c̄
Strip theory calc., parabolic deflection curve
Lifting surface theory, parabolic deflection curve
Matrix calc. with strip theory, I = I_r[1-(1-λ)(r/s)^4]
nW/S = 150
σ_max = 30,000
Dynamic pressure, q, lb/sq ft.
(b) Neutral point shift

FIG. 8. Variation of lift-curve slope and neutral point shift with dynamic pressure at $M = 1.414$ for the elastic wing of Fig. 7, experiencing pure bending deformations.

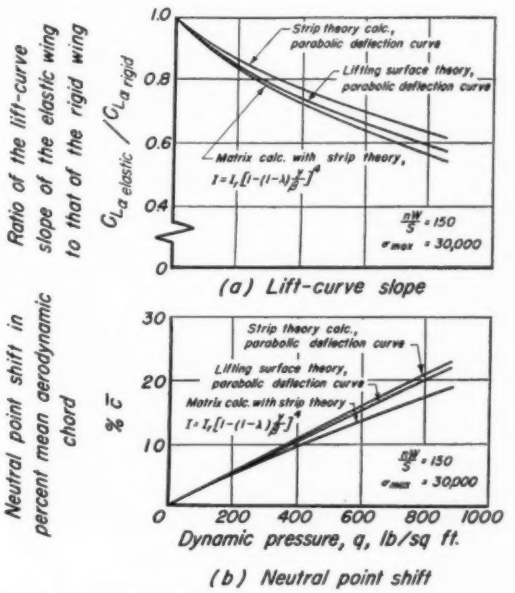
Ratio of the lift-curve slope of the elastic wing to that of the rigid wing
C_L_α elastic / C_L_α rigid
Strip theory calc., parabolic deflection curve
Lifting surface theory, parabolic deflection curve
Matrix calc. with strip theory, I = I_r[1-(1-λ)(r/s)^4]
nW/S = 150
σ_max = 30,000
(a) Lift-curve slope
Neutral point shift in percent mean aerodynamic chord
% c̄
Strip theory calc., parabolic deflection curve
Lifting surface theory, parabolic deflection curve
Matrix calc. with strip theory
I = I_r[1-(1-λ)(r/s)^4]
nW/S = 150
σ_max = 30,000
Dynamic pressure, q, lb/sq ft.
(b) Neutral point shift

FIG. 9. Variation of lift-curve slope and neutral point shift with dynamic pressure at $M = 1.414$ for the elastic wing of Fig. 7, experiencing combined bending and torsional deformations.

Mach Number Effects

It is of interest to compare the results obtained for supersonic speed for the wing of Fig. 7 with calculations for the same wing in incompressible flow utilizing the aerodynamic loadings given by the Weissinger method as developed by Stevens.[9] A comparison is shown in

Fig. 10 for a Mach Number of 1.414 and for incompressible flow. It is evident from these results that the aeroelastic characteristics are affected by the flight Mach Number in a manner such as to give less loss in lift-curve slope and a smaller shift in neutral point at subsonic speed. About half the improvement found for subsonic flight is attributable to the more forward position of the section center of pressure for incompressible flow which changes the torsional deformations of the wing so as to compensate to a greater extent for the effects of the bending deformation.

Aside from the effect of center-of-pressure change, the effects of Mach Number are small, as might be expected since the span loading at subsonic speed is nearly equivalent to that for supersonic speed at least for wings swept within the Mach cone.

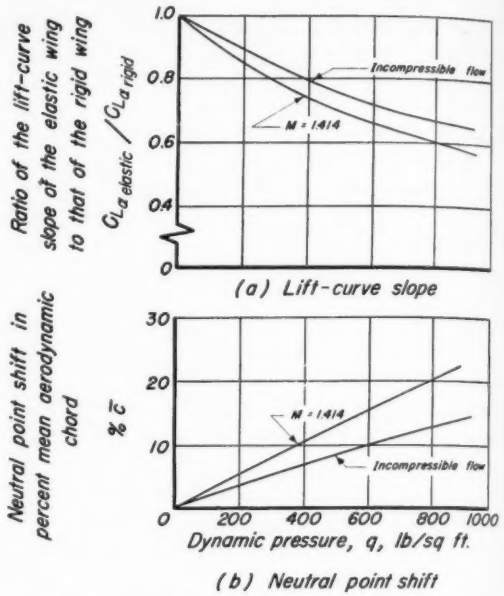

FIG. 10. A comparison of the variation of lift-curve slope and neutral point shift with dynamic pressure for the elastic wing of Fig. 7 in supersonic and incompressible flow.

REFERENCES

[1] Jones, R. T., *Estimated Lift-Drag Ratios at Supersonic Speed*, N.A.C.A. T.N. No. 1350, 1947.

[2] Zender, George, and Libove, Charles, *Stress and Distortion Measurements in a 45° Swept Box Beam Subjected to Bending and to Torsion*, N.A.C.A. T.N. No. 1525, 1948.

[3] Cohen, Doris, *The Theoretical Lift of Flat Swept-Back Wings at Supersonic Speeds*, N.A.C.A. T.N. No. 1555, 1948.

[4] Stewart, H. J., *The Lift of a Delta Wing at Supersonic Speeds*, Quart. App. Math., Vol. IV, No. 3, pp. 246–254, October, 1946.

[5] Brown, Clinton E., *Theoretical Lift and Drag of Thin Triangular Wings at Supersonic Speeds*, N.A.C.A. T.N. No. 1183, 1946.

[6] Lagerstrom, P. A., *Linearized Supersonic Theory of Conical Wings*, N.A.C.A. T.N. No. 1685, 1948.

[7] Brown, Clinton E., and Adams, Mac C., *Damping in Pitch and Roll of Triangular Wings at Supersonic Speeds*, N.A.C.A. T.N. No. 1566, 1948.

[8] Diederich, Franklin W., *Calculation of the Aerodynamic Loading of Flexible Wings of Arbitrary Plan Form and Stiffness*, N.A.C.A. T.N. No. 1876, 1949.

[9] Stevens, Victor I., *Theoretical Basic Span Loading Characteristics of Wings with Arbitrary Sweep, Aspect Ratio, and Taper Ratio*, N.A.C.A. T.N. No. 1772, 1948.

Appendix

MATHEMATICAL DERIVATION OF LOADING FUNCTIONS AND PLAN-FORM CONSTANTS

The functions $f_1(y)$, $f_2(y)$, $f_3(y)$, and $f_4(y)$ and the constants F_1, F_2, F_3, F_4, F_5, and F_6, which appear in Eqs. (7) to (23) of the text, are given in this Appendix. The evaluation of the constants from the analytical expression may prove to be tedious, and it may be easier to evaluate the corresponding integral equations graphically.

The functions $f_1(y)$ and $f_2(y)$ were developed from the following integral:

$$l/q = s \int_{y/m}^{(y + mc_0)/m_t} \left(\frac{\Delta p}{q}\right)_{y = const.} dx$$

from which

$$f_1(y) = \int_{y/m}^{(y + mc_0)/m_t} \frac{dx}{\sqrt{m^2 - (y/x)^2}}$$

which yields

$$f_1(y) = (1/m^2) \sqrt{[(m^2/m_t^2) - 1]y^2 + (2m^2/m_t)c_0 y + m^2 c_0^2}$$

and

$$f_2(y) = \int_{y/m}^{(y + mc_0)/m_t} (x + y) \sqrt{\frac{x + y}{mx - y}}\, dx + \int_{y/m}^{(y + mc_0)/m_t} (x - y) \sqrt{\frac{x - y}{mx + y}}\, dx$$

which yields

$$f_2(y) = \left[\frac{2m(y + m_t c_0) + m_t y(5m + 3)}{4m^2 m_t^2}\right]\left[\sqrt{(y + m_t c_0 + m_t y)\,(my + mm_t c_0 - m_t y)}\right] +$$
$$\left[\frac{3y^2(m + 1)^2}{8m^{5/2}}\right]\left[\cosh^{-1}\frac{2m(y + m_t c_0) - m_t y(1 - m)}{m_t(m + 1)y}\right] + \left[\frac{2m(y + m_t c_0) - m_t y(5m + 3)}{4m^2 m_t^2}\right] \times$$
$$\left[\sqrt{(y + m_t c_0 - m_t y)\,(my + mm_t c_0 + m_t y)}\right] + \left[\frac{3y^2(m + 1)^2}{8m^{5/2}}\right]\left[\cosh^{-1}\frac{2m(y + m_t c_0) + m_t y(1 - m)}{m_t(m + 1)y}\right] +$$
$$\left[\frac{y^2(5m + 1)\sqrt{2(1 - m)}}{4m^{5/2}}\right] - \left[\frac{3y^2(m + 1)^2}{8m^{5/2}}\right]\left[\cosh^{-1}\frac{3 - m}{m + 1}\right]$$

The constants F_1 and F_2 are evaluated as follows: $F_1 = \int_0^\beta f_1(y)\,dy$, which yields, for $m_t \neq 1$,

$$F_1 = \frac{a\beta - m^2 f}{2m_t m^2 a}\sqrt{m^2 f^2 + 2\beta m^2 f - a\beta^2} + \frac{m_t m c_0^2}{2a} + \frac{m_t f^2}{2a^{3/2}}\left(\cos^{-1}\frac{m^2 f - a\beta}{mm_t f} - \cos^{-1}\frac{m}{m_t}\right)$$

and, for $m_t = 1$,

$$F_1 = \frac{\beta(1 - m^2) - m^2 c_0}{2m^2(1 - m^2)}\sqrt{m^2 c_0^2 + 2\beta m^2 c_0 - \beta^2(1 - m^2)} +$$
$$\frac{mc_0^2}{2(1 - m^2)} + \frac{c_0^2}{2(1 - m^2)^{3/2}}\left[\cos^{-1}\frac{m^2 c_0 - \beta(1 - m^2)}{mc_0} - \cos^{-1} m\right]$$

where $a = m_t^2 - m^2$, $f = m_t c_0$, and $F_2 = \int_0^\beta f_2(y)\,dy$, which yields, for $m_t \neq 1$,

$$F_2 = \left(\frac{e}{12m^2 m_t^2 b}\right)\left[(mf^2)^{3/2} - (\beta df + mf^2 - \beta^2 b)^{3/2}\right] + \left[\frac{f(de + 4mb)}{8m^2 m_t^2 b}\right] \times$$
$$\left\{\frac{2\beta b - df}{4b}\sqrt{\beta df + mf^2 - \beta^2 b} + \frac{m^{1/2} df^2}{4b} + \frac{m_t^2(m + 1)^2 f^2}{8b^{3/2}}\left[\cos^{-1}\frac{df - 2\beta b}{m_t f(m + 1)} - \cos^{-1}\frac{d}{m_t(m + 1)}\right]\right\} +$$
$$\left[\frac{\beta^3(m + 1)^2}{8m^{5/2}}\right]\left[\cosh^{-1}\frac{\beta d + 2mf}{\beta m_t(m + 1)} + \cosh^{-1}\frac{\beta h + 2mf}{\beta m_t(m + 1)} - \cosh^{-1}\frac{3 - m}{m + 1}\right] + \left[\frac{f(m + 1)^2}{8m^2}\right] \times$$
$$\left\{\frac{f^2(3d^2 + 4mb)}{8b^{5/2}}\left[\cos^{-1}\frac{df - 2\beta b}{m_t f(m + 1)} - \cos^{-1}\frac{d}{m_t(m + 1)}\right] - \frac{3df + 2\beta b}{4b^2}\sqrt{mf^2 + \beta df - \beta^2 b} + \frac{3m^{1/2} df^2}{4b^2}\right\} +$$
$$\left[\frac{\beta^3(5m + 1)\sqrt{2(1 - m)}}{12m^{5/2}}\right] + \left(\frac{j}{4m^2 m_t^2}\right)\left[\frac{(mf^2 + \beta hf - \beta^2 g)^{3/2} - (mf^2)^{3/2}}{3g}\right] + \left[\frac{f(4mg - hj)}{8m^2 m_t^2 g}\right] \times$$
$$\left\{\frac{2\beta g - hf}{4g}\sqrt{mf^2 + \beta hf - \beta^2 g} + \frac{m^{1/2} f^2 h}{4g} + \frac{f^2 m_t^2(1 + m)^2}{8g^{3/2}}\left[\cos^{-1}\frac{hf - 2\beta g}{m_t f(m + 1)} - \cos^{-1}\frac{h}{m_t(m + 1)}\right]\right\} +$$
$$\left[\frac{f(m + 1)^2}{8m^2}\right]\left\{\frac{f^2(3h^2 + 4mg)}{8g^{5/2}}\left[\cos^{-1}\frac{hf - 2\beta g}{m_t f(m + 1)} - \cos^{-1}\frac{h}{m_t(m + 1)}\right] - \frac{2\beta g + 3hf}{4g^2} \times\right.$$
$$\left.\sqrt{mf^2 + \beta hf - \beta^2 g} + \frac{3m^{1/2} hf^2}{4g^2}\right\}$$

where $b = (m_t - m)(m_t + 1)$, $d = 2m + mm_t - m_t$, $e = 2m + 5mm_t + 3m_t$, $f = m_t c_0$, $g = (m + m_t) \times (m_t - 1)$, $h = 2m - mm_t + m_t$, and $j = 3m_t + 5mm_t - 2m$. For $m_t = 1$,

$$F_2 = \left(\frac{7m+3}{4m^2}\right)\left\{\frac{[mc_0^2 + \beta c_0(3m-1) + 2\beta^2(m-1)]^{3/2}}{6(m-1)} - \frac{(mc_0^2)^{3/2}}{6(m-1)}\right\} + \left[\frac{c_0}{2m} - \frac{c_0(3m-1)(7m+3)}{16m^2(m-1)}\right] \times$$
$$\left\{\left[\frac{4\beta(m-1) + c_0(3m-1)}{8(m-1)}\right]\left[\sqrt{mc_0^2 + \beta c_0(3m-1) + 2\beta^2(m-1)}\right] - \left[\frac{c_0(3m-1)}{8(m-1)}\right] \times \right.$$
$$\left.\left(\sqrt{mc_0^2}\right) + \left[\frac{c_0^2(m+1)^2}{16\sqrt{2}(1-m)^{3/2}}\right]\left[\cos^{-1}\frac{4\beta(m-1) + c_0(3m-1)}{c_0(m+1)} - \cos^{-1}\frac{3m-1}{m+1}\right]\right\} + \left[\frac{\beta^3(m+1)^2}{8m^{3/2}}\right] \times$$
$$\left[\cosh^{-1}\frac{\beta(3m-1) + 2mc_0}{\beta(m+1)} + \cosh^{-1}\frac{\beta(m+1) + 2mc_0}{\beta(m+1)} - \cosh^{-1}\frac{3-m}{m+1}\right] + \left[\frac{c_0^2(m+1)^2}{8m}\right] \times$$
$$\left(\left[\frac{4\beta(m-1) - 3c_0(3m-1)}{16mc_0(m-1)^2}\right]\left[\sqrt{mc_0^2 + \beta c_0(3m-1) + 2\beta^2(m-1)}\right] + \left[\frac{3c_0(3m-1)}{16m^{1/2}(m-1)^2}\right] + \right.$$
$$\left[\frac{c_0(19m^2 - 10m + 3)}{32\sqrt{2}m(1-m)^{3/2}}\right]\left[\cos^{-1}\frac{4\beta(m-1) + c_0(3m-1)}{c_0(m+1)} - \cos^{-1}\frac{3m-1}{m+1}\right] +$$
$$\left\{\frac{2[8m^2c_0^2 - 4\beta mc_0(m+1) + 3\beta^2(m+1)^2]}{15mc_0^{3/2}(m+1)^3}\right\}\left[\sqrt{mc_0 + \beta(m+1)}\right] - \left.\frac{16m^{3/2}c_0}{15(m+1)^3}\right) +$$
$$\left\{\left[\frac{1}{3m(m+1)}\right] + \left[\frac{2mc_0 - 3\beta(m+1)}{10m^2c_0(m+1)}\right]\right\}\left\{[mc_0^2 + \beta c_0(m+1)]^{3/2}\right\} +$$
$$\left[\frac{\beta^3(5m+1)\sqrt{2(1-m)}}{12m^{5/2}}\right] - \left[\frac{8(mc_0^2)^{3/2}}{15m(m+1)}\right]$$

The functions $f_3(y)$ and $f_4(y)$ were developed from the following integral:

$$\frac{m_s}{q} = -s^2\int_{y/m}^{(y + mtc_0)/mt}\left(\frac{\Delta p}{q}\right)_{y = const.} x\,dx$$

from which

$$f_3(y) = \int_{y/m}^{(y + mtc_0)/mt}\frac{x\,dx}{\sqrt{m^2 - (y/x)^2}}$$

Then,

$$f_3(y) = \frac{y + m_tc_0}{2m^2m_t^2}\sqrt{m^2(y + m_tc_0)^2 - m_t^2y^2} + \frac{y^2}{2m^3}\cosh^{-1}\frac{m(y + m_tc_0)}{m_ty}$$

Also,

$$f_4(y) = \int_{y/m}^{(y + mtc_0)/mt}(x + y)\sqrt{\frac{x + y}{mx - y}}\,x\,dx + \int_{y/m}^{(y + mtc_0)/mt}(x - y)\sqrt{\frac{x - y}{mx + y}}\,x\,dx$$

which yields

$$f_4(y) = \left[\sqrt{(y + m_tc_0 + m_ty)(my + mm_tc_0 - m_ty)}\right] \times$$
$$\left[\frac{8(y + m_tc_0)^2}{24mm_t^3} + \frac{2mm_ty(y + m_tc_0)(7m+5) + m_t^2y^2(3m^2 + 22m + 15)}{24m^3m_t^3}\right] + \left[\frac{y^3(m^3 - 3m^2 - 9m - 5)}{16m^{7/2}}\right] \times$$
$$\left[\cosh^{-1}\frac{(2m - mm_t + m_t)y + 2mm_tc_0}{m_t(m+1)y} - \cosh^{-1}\frac{3-m}{m+1} - \cosh^{-1}\frac{(2m + mm_t - m_t)y + 2mm_tc_0}{m_t(m+1)y}\right] +$$
$$\left[\sqrt{(y + m_tc_0 - m_ty)(my + mm_tc_0 + m_ty)}\right] \times$$
$$\left[\frac{8(y + m_tc_0)^2}{24mm_t^3} - \frac{2mm_ty(y + m_tc_0)(7m+5) - m_t^2y^2(3m^2 + 22m + 15)}{24m^3m_t^3}\right] -$$
$$\left[\frac{y^3(3m^2 + 8m + 13)\sqrt{2(1-m)}}{24m^{7/2}}\right]$$

The constant F_3 is evaluated as $F_3 = \int_0^\beta f_3(y)dy$, which yields, for $m_t \neq 1$,

$$F_3 = \frac{m^3f^3 - (m^2f^2 + 2\beta m^2f - \beta^2a)^{3/2}}{6m_t{}^2m^2a} + \frac{\beta^3}{6m^3}\cosh^{-1}\frac{m(\beta + f)}{\beta m_t} + \frac{f(a\beta - 3m^2f)\sqrt{m^2f^2 + 2\beta m^2f - a\beta^2}}{6m^2a^2} + \frac{mf^3}{2a^2} + \frac{f^3(2m_t{}^2 + m^2)}{6a^{5/2}}\left(\cos^{-1}\frac{m^2f - a\beta}{mm_t{}^2c_0} - \cos^{-1}\frac{mf}{m_t{}^2c_0}\right)$$

and, for $m_t = 1$,

$$F_3 = \frac{m^3c_0{}^3 - [m^2c_0{}^2 + 2\beta m^2c_0 - \beta^2(1 - m^2)]^{3/2}}{6m^2(1 - m^2)} + \frac{\beta^3}{6m^3}\cosh^{-1}\frac{m(\beta + c_0)}{\beta} + \frac{c_0[\beta(1 - m^2) - 3m^2c_0]\sqrt{m^2c_0{}^2 + 2\beta m^2c_0 - \beta^2(1 - m^2)}}{6m^2(1 - m^2)^2} + \frac{mc_0{}^3}{2(1 - m^2)^2} + \frac{c_0{}^3(2 + m^2)}{6(1 - m^2)^{5/2}}\left[\cos^{-1}\frac{m^2c_0 - \beta(1 - m^2)}{mc_0} - \cos^{-1}m\right]$$

Also, F_4 is evaluated as $F_4 = \int_0^\beta f_4(y)\,dy$, which yields, for $m_t \neq 1$,

$$F_4 = \left[\frac{A}{24m^3m_t{}^3}\left(\beta + \frac{5df}{6b}\right) + \frac{B}{18m^3m_t{}^3}\right]\left[\frac{(mf^2 + \beta df - \beta^2b)^{3/2}}{-4b}\right] + \left\{\frac{2\beta b - df}{4b}\sqrt{mf^2 + \beta df - \beta^2b} + \frac{m_t{}^2f^2(m + 1)^2}{8b^{3/2}}\left[\cos^{-1}\frac{df - 2\beta b}{m_tf(m + 1)} - \cos^{-1}\frac{d}{m_t(m + 1)}\right] + \frac{m^{1/2}df^2}{4b}\right\}\left[\frac{Af^2(5d^2 + 4mb) + 8Bbdf + 128m^2b^2f^2}{384m^3m_t{}^3b^2}\right] + \left(\frac{5Adf}{144m^3m_t{}^3b} + \frac{B}{18m^3m_t{}^3}\right)\left[\frac{(mf^2)^{3/2}}{4b}\right] + \left(\frac{C}{4}\right)\left(\beta^4\left[\cosh^{-1}\frac{\beta h + 2mf}{\beta m_t(m + 1)} - \cosh^{-1}\frac{3 - m}{m + 1} - \cosh^{-1}\frac{\beta d + 2mf}{\beta m_t(m + 1)}\right] + (m^{1/2}f)\left\{\left(\frac{\beta^2}{3b} + \frac{5\beta df}{12b^2} + \frac{5d^2f^2}{8b^3} + \frac{2mf^2}{3b^2}\right)\left(\sqrt{mf^2 + \beta df - \beta^2b}\right) - \left(\frac{\beta^2}{3g} + \frac{5\beta hf}{12g^2} + \frac{5f^2h^2}{8g^3} + \frac{2mf^2}{3g^2}\right)\times\left(\sqrt{mf^2 + \beta fh - \beta^2g}\right) - \left[\frac{df^3(12mb - 5d^2)}{16b^{7/2}}\right]\left[\cos^{-1}\frac{df - 2\beta b}{m_tf(m + 1)} - \cos^{-1}\frac{d}{m_t(m + 1)}\right] + \left[\frac{hf^3(12mg + 5h^2)}{16g^{7/2}}\right]\left[\cos^{-1}\frac{hf - 2\beta g}{m_tf(m + 1)} - \cos^{-1}\frac{h}{m_t(m + 1)}\right] - (f^3m^{1/2})\left(\frac{5d^2}{8b^3} + \frac{2m}{3b^2} - \frac{5h^2}{8g^3} - \frac{2m}{3g^2}\right)\right\}\right) + \left[\frac{Df^2(5h^2 + 4mg) + 8Hfgh + 128f^2m^2g^2}{384m^3m_t{}^3g^2}\right]\left\{\left(\frac{2\beta g - fh}{4g}\right)\left(\sqrt{mf^2 + \beta fh - \beta^2g}\right) + \left(\frac{f^2hm^{1/2}}{4g}\right) + \left[\frac{m_t{}^2f^2(m + 1)^2}{8g^{3/2}}\right]\left[\cos^{-1}\frac{fh - 2\beta g}{m_tf(m + 1)} - \cos^{-1}\frac{h}{m_t(m + 1)}\right]\right\} - \left[\left(\frac{D}{24m^3m_t{}^3}\right)\left(\beta + \frac{5fh}{6g}\right) + \left(\frac{H}{18m^3m_t{}^3}\right)\right]\times\left[\frac{(mf^2 + \beta fh - \beta^2g)^{3/2}}{4g}\right] - \left[\frac{\beta^4(3m^2 + 8m + 13)\sqrt{2(1 - m)}}{96m^{7/2}}\right] + \left[\frac{(mf^2)^{3/2}}{4g}\right]\left[\left(\frac{5Dfh}{144m^3m_t{}^3g}\right) + \left(\frac{H}{18m^3m_t{}^3}\right)\right]$$

where $A = 8m^2 + 14m^2m_t + 10mm_t + 3m^2m_t{}^2 + 22mm_t{}^2 + 15m_t{}^2$, $B = 2mm_tc_0(8m + 7mm_t + 5m_t)$, $C = (m^3 - 3m^2 - 9m - 5)/16m^{7/2}$, $D = 8m^2 - 14m^2m_t - 10mm_t + 3m^2m_t{}^2 + 22mm_t{}^2 + 15m_t{}^2$, and $H = 2mm_tc_0(8m - 7mm_t - 5m_t)$. For $m_t = 1$,

$$F_4 = \left\{\frac{T}{32m^3}\left[\beta - \frac{5c_0(3m-1)}{12(m-1)}\right] + \frac{V}{24m^3}\right\}\left\{\frac{[mc_0^2 + \beta c_0(3m-1) + 2\beta^2(m-1)]^{3/2}}{6(m-1)}\right\} +$$
$$\left\{\frac{T}{32m^3}\left[\frac{5c_0(3m-1)}{12(m-1)}\right] - \frac{V}{24m^3}\right\}\left[\frac{(mc_0^2)^{3/2}}{6(m-1)}\right] + \left\{\frac{T}{24m^3}\left[\frac{c_0^2(37m^2-22m+5)}{64(m-1)^2}\right] - \frac{V}{24m^3}\left[\frac{c_0(3m-1)}{4(m-1)}\right] + \frac{c_0^2}{3m}\right\} \times$$
$$\left\{\frac{4\beta(m-1) + c_0(3m-1)}{8(m-1)}\left[\sqrt{mc_0^2 + \beta c_0(3m-1) + 2\beta^2(m-1)}\right] + \frac{c_0^2(m+1)^2}{16\sqrt{2}(1-m)^{3/2}} \times\right.$$
$$\left.\left[\cos^{-1}\frac{4\beta(m-1) + c_0(3m-1)}{c_0(m+1)} - \cos^{-1}\frac{3m-1}{m+1}\right] + \frac{m^{1/2}c_0^2(3m-1)}{8(1-m)}\right\} +$$
$$\frac{C}{4}\left(\beta^4\left[\cosh^{-1}\frac{\beta(m+1) + 2mc_0}{\beta(m+1)} - \cosh^{-1}\frac{3-m}{m+1} - \cosh^{-1}\frac{\beta(3m-1) + 2mc_0}{\beta(m+1)}\right] +\right.$$
$$(mc_0)\left\{\frac{2\beta^3\sqrt{m^2c_0^2 + \beta mc_0(m+1)}}{7mc_0(m+1)} - \frac{4[8m^2c_0^2 - 4\beta mc_0(m+1) + 3\beta^2(m+1)^2]}{35(1+m)^4}\sqrt{m^2c_0^2 + \beta mc_0(m+1)} -\right.$$
$$\left[\frac{\beta^2}{6m(m-1)} - \frac{5\beta c_0(3m-1)}{48m(m-1)^2} + \frac{5c_0^2(3m-1)^2}{64m(m-1)^3} - \frac{c_0^2}{6(m-1)^2}\right]\sqrt{2\beta^2m(m-1) + \beta mc_0(3m-1) + m^2c_0^2} +$$
$$\frac{32m^3c_0^3}{35(m+1)^4} + \frac{c_0^3(63m^3 - 39m^2 + 21m - 5)}{128\sqrt{2m(1-m)}\,(m-1)^3}\left[\cos^{-1}\frac{4\beta(m-1) + c_0(3m-1)}{c_0(m+1)} - \cos^{-1}\frac{3m-1}{m+1}\right] +$$
$$\left.\left.\frac{5c_0^3(3m-1)^2}{64(m-1)^3} - \frac{mc_0^3}{6(m-1)^2}\right\}\right) - \left[\frac{\beta^4(3m^2 + 8m + 13)\sqrt{2(1-m)}}{96m^{7/2}}\right] +$$
$$\left\{\frac{2c_0}{9m(m+1)} + \frac{(5-m)\,[2mc_0 - 3\beta(m+1)]}{90m^2(m+1)^2} + \frac{(5-m)\,[8m^2c_0^2 - 12\beta mc_0(m+1) + 15\beta^2(m+1)^2]}{420m^3c_0(m+1)^2}\right\} \times$$
$$\left\{[mc_0^2 + \beta c_0(m+1)]^{3/2}\right\} - [(mc_0^2)^{3/2}]\left[\frac{2c_0}{9m(m+1)} + \frac{c_0(5-m)}{45m(m+1)^2} + \frac{2c_0(5-m)}{105m(m+1)^3}\right]$$

where $T = 25m^2 + 32m + 15$ and $V = 10mc_0(3m+1)$. The constants F_5 and F_6 are evaluated as $F_5 = \int_0^\beta f_1(y)y\,dy$, or

$$F_5 = \frac{1}{m^2m_t}\left\{m^3f^3 - (m^2f^2 + 2m^2f\beta - a\beta^2)^{3/2} + \frac{m^2f}{2a^2}\left[(a\beta - m^2f)\sqrt{m^2f^2 + 2m^2f\beta - a\beta^2} +\right.\right.$$
$$\left.\left.m^3f^2 + \frac{m^2m_t^2f^2}{\sqrt{a}}\left(\cos^{-1}\frac{m^2f - a\beta}{mm_tf} - \cos^{-1}\frac{m}{m_t}\right)\right]\right\}$$

and $F_6 = \int_0^\beta f_3(y)y\,dy$, or

$$F_6 = \frac{1}{2m^2m_t^2}\left\{\frac{m^3f^4(4m_t^2 + m^2)}{12a^2} - \left[\frac{3a\beta + f(4m_t^2 + m^2)}{12a^2}\right](m^2f^2 + 2m^2f\beta - a\beta^2)^{3/2} +\right.$$
$$\left.\frac{5m^2m_t^2f^2}{8a^3}\left[(a\beta - m^2f)\sqrt{m^2f^2 + 2m^2f\beta - \alpha\beta^2} + m^3f^2 + \frac{m^2m_t^2f^2}{a^{1/2}}\left(\cos^{-1}\frac{m^2f - a\beta}{mm_tf} - \cos^{-1}\frac{m}{m_t}\right)\right]\right\} +$$
$$\frac{\beta^4}{8m^3}\cosh^{-1}\frac{m(\beta+f)}{\beta m_t} + \frac{f}{8m^2}\left[\frac{m^3f^3(4m_t^2 + 11m^2)}{6a^3} - \left(\frac{\beta^2}{3a} + \frac{5\beta m^2f}{6a^2} + \frac{5m^4f^2}{2a^3} + \frac{2m^2f^2}{3a^2}\right) \times\right.$$
$$\left.\sqrt{m^2f^2 + 2m^2f\beta - a\beta^2} + \frac{m^4f^3(3m_t^2 + 2m^2)}{2a^{7/2}}\left(\cos^{-1}\frac{m^2f - a\beta}{mm_tf} - \cos^{-1}\frac{m}{m_t}\right)\right]$$

A System for the Excitation of Pure Natural Modes of Complex Structure

ROBERT C. LEWIS* AND DONALD L. WRISLEY†

Massachusetts Institute of Technology

SUMMARY

Analogy is drawn between analytical and experimental approaches to the evaluation of structural dynamic behavior, pointing out the relationship between method complexity and adequacy of results.

The theory, construction, and operation of a system using 24 shakers controlled from a console in the systematic excitation of pure natural modes are described. Practical operation is made feasible by the coordinated display of the force and resultant velocity at each shaker station, together with a system for orderly discriminatory adjustment by the operator, which is analogous to a mathematical iteration. Sample laboratory and full-scale data are shown.

INTRODUCTION

CALCULATION OF THE DYNAMIC BEHAVIOR of complex structure has become increasingly important in the design of modern aircraft whose dynamic loadings influence both aerodynamic and strength considerations.[1] The adequacy of these calculations is dependent on the thoroughness of the mathematical treatment and on the correctness of the engineering evaluation of boundary conditions required by physical circumstances.

Development of mathematical techniques and ingenuity in their application are continually being employed to extend analytical accomplishment. Since it is by experimental verification of the analytical results that the adequacy of the engineering evaluations are proved or found wanting, a similar degree of development and ingenuity is required in the experimental evaluation of these same complex structures.

Experimental determination of the natural mode responses of the complex aircraft structure is required by various contracting agencies.[2] Unfortunately, the results of many shake tests are in a form difficult to compare with the calculated data, and a large part of their value is thereby lost.

The lack of clarity in comparing calculated and experimental data on natural mode responses does little to aid in checking the validity of the theoretical assumptions; it may help to confirm the analyst to more exclusive dependency on mathematics as the ultimate definition of structural behavior, or it may further convince the experimentalist of the perversity of nature oversimplified by the theorist. Neither of these results is desirable.

It would seem worth while to examine the possible reasons for the confused picture of the natural mode responses obtained from some shake-test data:

(1) The shake test on a new airplane is usually made on the prototype prior to flight. Schedules may be lagging and pressure high. Even in the presence of a contract requirement, the shake test smacks of flogging a dead horse to the project nearing the already long-delayed fruition of flight.

(2) Budget and time may not allow check of data for adequacy during the tests. They almost certainly prohibit the rerunning of any data found inadequate later because of the extensive set-up time required.

(3) The experimental procedures used may in some cases be naive by comparison with the mathematical methods whose results they are expected to check.

There is certainly more than a superficial analogy between the mathematical analysis and the experimental analysis, and the results in either case will be no more elegant than the methods devised to treat the problem. The inability in some cases to obtain clear definition of the mode shapes experimentally in complex structure, by the use of techniques adequate for one or two degrees of freedom, should not be surprising.

The instruments available to the experimentalist have developed in a manner similar to the methods of the analyst, and there is a far greater profusion of good instruments here in the United States than elsewhere. It would seem worth while to utilize this material advantage by the continued exercise of ingenuity in the development of experimental techniques capable of evaluating the physical complexities described by the language of the theorist.

An attempt along this line is embodied in the equipment and method of use developed under Government contract‡ and described in this paper.

THE GENERAL PROBLEM

Aircraft structures are characterized by distributed flexibility and mass and a general complexity of structural and spatial arrangement that leads to many natural modes. These modes may have frequencies

Presented at the Aeroelasticity Session, Eighteenth Annual Meeting, I.A.S., New York, January 23–26, 1950.

* Aero-Elastic and Structures Research, Guggenheim Aeronautical Laboratory. Now with The Calidyne Company.

† Aero-Elastic and Structures Research, Guggenheim Aeronautical Laboratory.

‡ The work on which this report is based was done under Contract N156s-2579 for the Aeronautical Structures Laboratory, Naval Air Material Center, Philadelphia Naval Base Station.

close together and may be complicated in mode shape, with all parts of the ship more or less active.

This general complexity and activity is, at one and the same time, (a) the major reason for making experimental check on a somewhat simplified analysis and (b) the major difficulty in obtaining clear experimental definitions of the actual responses.

In general, the excitation of the structure is applied at arbitrary points, and the resultant motion of the structure at the forcing frequency may be thought of as the summation of the forced responses of each of the structure's many natural modes. Since some of the modes have natural frequencies close together, each of several modes may be excited to substantial amplitude by an arbitrary excitation, and various parts of the structure, each perhaps active in a different mode, will exhibit substantial phase differences. If under these conditions the alternating forces are removed, each of the several modes decays at its own frequency, with the production of beats.

The objective sought for the experimental method is to produce, in the complex structure, by means of adjustable forces, oscillations that consist essentially of one natural mode of motion. For the purposes of explaining the basic concepts of the development, it is convenient to assume that such a pure natural mode is by some means sustained. The properties of natural modes are such that all points in the structure will reach their maximum displacements at the same instant. At the instant when the structure reaches the maximum of its complex deflection form, we can visualize this elastic deformation of the structure as the result of a specific distributed inertial loading, and we can further see that the distributed inertial loading produces shears and moments on the structure which are exactly balanced by the shears and moments in the elastically deformed structural members.

In the absence of damping forces, such a natural mode would continue in the steady-state oscillation we have imagined without the application of external forces. If, on the other hand, damping shears and moments did exist in the structure, *we could still preserve the steady-state natural mode if we exactly canceled these shears and moments by externally applied oscillatory forces.*

This is the basic concept around which the method was formed. This assumption of the accomplished existence of a pure natural mode allows certain inferences of importance in devising the experimental method:

(1) Since the natural mode motions are all in phase, the damping forces and, therefore, the driving forces will all be in phase when the final desired condition of a pure mode is obtained. This means that phase manipulation of the driving forces will be not only unnecessary but undesirable.

(2) If our externally applied forces are not properly adjusted to cancel exactly the internal damping shears and moments, the resultant motions of the structure will depart from the "in-phase" condition. This is a valuable criterion for mode purity but not a suitable criterion for corrective adjustment, at least for the present.

(3) If the motion existing under the action of the externally applied oscillating forces is a satisfactory approximation to a pure natural mode, a smooth decay of the mode should be obtained on removal of the excitation; freedom from beats will indicate at least a practical approximation to the required pure mode excitation and will indicate conclusively that the experimentally determined frequency, mode shape, and damping coefficient describe a true natural mode.

(4) A large number of shakers will be required at distributed points on the complex structure in order that a unique adjustment of the magnitude and sense of the shaker forces will be obtained for each natural mode shape.*

The major fundamental problem in applying this simplified concept concerns the mechanics by which external forces can be adjusted to produce shears and moments to cancel exactly those produced by damping within the structure. We are brought face to face with the need for knowing more of the specific mechanisms of structural damping and its distribution. As a reasonable but simple assumption, we can take the concept of structural damping literally and assume that each elastic shear and moment in the structure has associated with it a proportional damping shear and moment in quadrature phase relationship.

Since shears and moments from the inertial loading exactly cancel the elastic shears and moments, it can be seen that, because of the assumption of damping distribution, the externally applied forces required to cancel the damping shears and moments must be distributed over the structure proportional to and in quadrature with the inertial loading. That is, each one of the numerous oscillating forces acting on a complex structure at a natural frequency must be adjusted in magnitude to be proportional to the product of the mass of the structure on which it acts and the amplitude of that mass in the mode being excited.

Thus, the result of assuming a distribution of damping proportional to stiffness provides a practically useful criterion on which to base discriminatory action. The question remains as to how nearly a pure mode might be excited by use of the criterion, even in practical cases where the simple assumption of damping distribution is violated immoderately.

In this connection it is timely to point out that normal mode concepts apply strictly to systems with zero damping, or a "small amount of damping," and are stretched with difficulty to cover the case of distributed

* This concept was formulated in memorandum Aer-RD-223-LEB, January 28, 1946, in which Lt. L. E. Beckley, U.S.N.R., outlined the essential advantages and requirements of such a system.

systems with discontinuous energy sinks or even lumped systems with nonuniform damping elements.

Unfortunately, the actual structures tested by the experimentalist do have concentrated energy sinks, and reasonably clear data are still desired for comparison with the calculations unaware of such circumstances. For example, conventional shaking of a wing at the tips may evoke enthusiastic response from the empennage at one of the "wing" natural frequencies. The experimental data will be confused by large phase shifts between empennage and wing motions, lack of clearly defined nodes, and beating on decay of the "natural" mode so excited. This situation may well be caused in large part by the phase shifts, due to transmission through the flexible wing and fuselage to the tail, of the forces introduced at the wing tips. The energy is fed in at the wing tips and is dissipated throughout the structure and, perhaps, in large sinks at the wing-fuselage joints. The dragging along of other modes consequent to this procedure might be expected. At the same time, much might be done to eliminate this damping- or phase-coupling by simply giving the empennage and other major parts of the structure firsthand knowledge of what is going on by the use of other shakers at these locations, all tied to the same source.

A good understanding of the concepts presented here in descriptive terms is essential to advanced experimental work. A complete mathematical treatment of the theory of small oscillations of conservative systems and of systems with small damping may be found in von Kármán and Biot,[3] chapters 5 and 6, and in Rayleigh,[4] Section 4. A summary of this theory is presented in Appendix I of this paper. Kennedy and Pancu[5] have made a masterful presentation of concepts pertaining to natural modes as a set of generalized coordinates and have presented a method combining experimental and analytical procedures in the separation and definition of structural natural modes.

The Specific Problems

Evolution of the general concepts outlined into an integrated set of equipment for testing full-scale aircraft required four major steps.

(1) Analysis of the theoretical system requirements for exciting natural modes, relating the structural properties, the shaker properties, the mode amplitudes, and the power requirements.

(2) Construction of experimental equipment, designed with consideration of the theoretical analysis.

(3) Experimental development. (a) Investigation of suitable criteria for mode purity by means of a complex model with an adjustable distribution of energy sinks. (b) Determination of suitable means of discriminatory action in adjustment of multiple shaker forces to achieve mode purity as indicated by the criteria discovered. (c) Evolution of a working system, based on practical requirements, on which to base the design of complete full-scale equipment.

(4) Construction and test of the full-scale equipment.

Analysis of Theoretical System

Power Expressions

Assume now a structure whose mass distribution is represented by the function $m = m(x, y)$ oscillating in the ith normal mode. The deflection of any point in the structure can be represented by the product of a real, normalized function $f_i = f_i(x, y)$ and a complex coefficient a_0 ($= a_0 \sin \omega t$). The analysis can be extended to include the z coordinate also.

According to the assumption of distribution of damping forces proportional to restoring forces (and, therefore, inertia forces), the absolute value of the damping force at any point (x_1y_1) is

$$|df_d| = |g_i df_R| = |g_i a_0 \omega_i^2 f_i(x_1y_1) m(x_1y_1)| \tag{1}$$

where df_d and df_R are damping and restoring forces and g_i is the damping coefficient for the ith mode.

The power absorbed by the force df_d is

$$dP_a = [df_d \cdot a_0 \omega_i f_i(x_1y_1)]/2 \tag{2}$$

and the total power absorbed by the structure is

$$P_a = \frac{1}{2} \int_x \int_y g_i a_0 \omega_i^2 f_i(x, y) m(x, y) \cdot a_0 \omega_i f_i(x, y) dx\, dy \tag{3}$$

$$P_a = \frac{g_i a_0^2 \omega_i^3}{2} \int_x \int_y m(x, y) f_i^2(x, y) dx\, dy \tag{4}$$

In evaluating the power supplied by the shaker forces, it is necessary to recognize that the physical limits of the actual shaker equipment must not be exceeded. It is desirable, then, to define the following quantities:

i_s = maximum force rating of an individual shaker
$\bar{M}$ = the value of the function $m = m(x, y)$, where the product $m(x, y)\, f_i(x, y)$ is a maximum for the ith mode
f_M = the value of the normalized deflection function $f_i = f_i(x, y)$ corresponding to $\bar{M}$
i = force at any point (x, y)

It was stated previously that the magnitude of the applied shaker force should be proportional to the product of mass and amplitude at the point of application

$$i = cmf_i \tag{5}$$

and the maximum force applied to the structure will be equal to the maximum shaker force

$$i_s = c\bar{M}f_M \tag{6}$$

from which the proportionality factor, c, can be evaluated for the ith mode under the condition that the

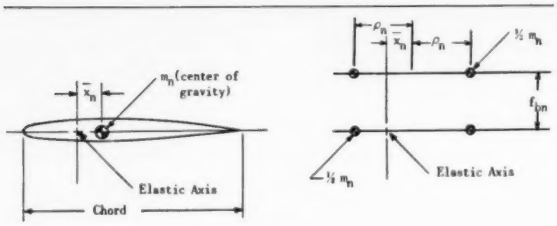

Fig. 1 Pure Bending

m_n = total mass of the n^{th} section

$\bar{x}_n$ = distance from the center of gravity to the elastic axis

ρ_n = radius of gyration of section n about its center of gravity

f_{bn} = value of the normalized deflection function $f_b(y)$ at station n.

$f_{b\bar{M}}$ = value of the normalized deflection function at the station where the product $\frac{m_n}{2} f_{bn}$ is a maximum.

ω_b = circular frequency of the bending mode in radians/sec.

g_b = damping coefficient for this bending mode.

$\bar{M}$ = value of $\frac{m_n}{2}$ corresponding to $f_{b\bar{M}}$

i_s = maximum shaker force rating

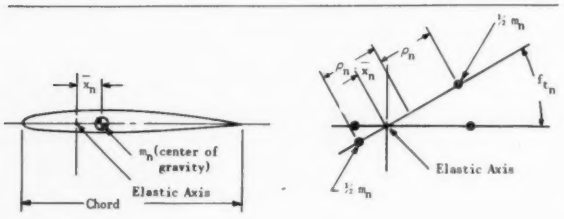

Fig. 2 Pure Torsion

m_n = total mass of section n

$\bar{x}_n$ = distance from the center of gravity to the elastic axis at station n

ρ_n = radius of gyration about the center of gravity at station n.

f_{tn} = the value of the normalized torsional deflection function at station n

$f_{t\bar{M}}$ = the value of the normalized torsional deflection function at the station where the product $\frac{m_n}{2}(\bar{x}_n + \rho_n) f_{tn}$ is a maximum.

ω_t = circular frequency of the torsion mode

g_t = damping coefficient for this mode.

$\bar{M}$ = value of $\frac{m_n}{2}$ corresponding to $f_{t\bar{M}}$

i_s = maximum shaker force rating

shaker called upon for the largest force is adjusted to its maximum rated output.

$$c = (i_s/\bar{M})(1/f_M) \tag{7}$$

the force at any point is now

$$i = (i_s/\bar{M})(f_i/f_M)m \tag{8}$$

The power delivered to the structure by the force i is

$$dP_d = \frac{1}{2}\left(\frac{i_s}{\bar{M}}\right)\frac{f_i}{f_M}\, m \cdot a_0\omega_i f_i \tag{9}$$

and the total power delivered by the distributed forces is

$$P_d = \frac{a_0\omega_i}{2}\left(\frac{i_s}{\bar{M}}\right)\frac{1}{f_M}\int_x\int_y m(x, y)\, f_i^2(x, y)\, dx\, dy \tag{10}$$

Amplitude at Resonance

Equating power delivered to power absorbed, the magnitude of the complex coefficient a_0, which evaluates the deflection, is obtained.

$$a_0 = \frac{1}{\omega_i^2 g_i}\left(\frac{i_s}{\bar{M}}\right)\frac{1}{f_M} \tag{11}$$

The amplitude that the structure attains (subject to shaker stroke limitations) is seen to be dependent on frequency, ω_i; damping coefficient, g_i; and the quantity $(i_s/\bar{M})(1/f_M)$, which includes mass distribution, mode shape, and the force limitation of the shaker.

Power Requirements

The power required to excite a structure to an amplitude a_0 in a normal mode is, from Eq. (4),

$$P_a = \frac{g_i a_0^2 \omega_i^3}{2}\int_x\int_y m(x, y)\, f_i^2(x, y)\, dx\, dy$$

and, substituting the value for a_0 from Eq. (11),

$$P_a = \frac{1}{2\omega_i g_i}\left(\frac{i_s}{\bar{M}}\right)^2\frac{1}{f_M{}^2}\int_x\int_y m(x, y)\, f_i^2(x, y)\, dx\, dy \tag{12}$$

While normal modes may be, and usually are, a combination of bending, torsion, and possibly chordwise motions, they may often be considered predominately "pure" bending or torsion or may be resolved to pure bending and pure torsion components. It is useful, therefore, to write Eq. (12) in terms of pure bending and pure torsion.

Since in an actual test program a finite number of shakers is available, the expressions for pure bending and pure torsion will be written in terms of summations.

The structure can be approximated by a dynamic system where the mass distribution is replaced by lumped masses at appropriate distances from the elastic axis and the axis of roll to approximate the actual inertia properties.

For the case of pure bending (i.e., no twist about the elastic axis, see Fig. 1), we can represent the displacement of the elastic axis by

$$s_b = f a_{0b}(y) \tag{13}$$

where $f_b(y)$ is the normalized deflection curve and a_0 is a complex coefficient.

The power required to excite the structure to an amplitude a_0 in the pure bending mode is

$$P_b = \frac{1}{2\omega_b g_b}\left(\frac{i_s}{\bar{M}}\right)^2\frac{1}{f_{bM}{}^2}\sum_{n=1}^{n} m_n f_{bn}{}^2 \tag{14}$$

and

$$a_0 = (1/\omega_b^2 g_b)\ (i_s/\bar{M})\ (1/f_{bM}) \tag{15}$$

For pure torsion, there is no displacement of the elastic axis (see Fig. 2), and we can express the twist at any spanwise station by the normalized function $f_t(y)$ and complex coefficient α_0:

$$\alpha = \alpha_0 f_t(y) \tag{16}$$

and the displacement of any chordwise point due to twist, assuming no chordwise bending, is

$$s_t = x\ \alpha_0 f_t(y) \tag{17}$$

Now, the power required to excite the structure to an amplitude α_0 in the pure torsion mode is

$$P_t = \frac{1}{2\omega_t g_t}\left(\frac{i_s}{\bar{M}}\right)^2 \frac{1}{f_{tM}^2(\bar{x}_M + \rho_M)^2} \sum_{n=1}^{n} \times m_n\ [\bar{x}_n^2 + \rho_n^2]\ f_{tn}^2 \tag{18}$$

and

$$\alpha_0 = \frac{1}{\omega_t^2 g_t}\left(\frac{i_s}{\bar{M}}\right) \frac{1}{f_{tM}(\bar{x}_M + \rho_M)} \tag{19}$$

Assuming no chordwise bending, any normal mode motion of the wing can be resolved into two components—pure translation of the chord line and twist about the elastic axis. The power required for each component may be found by using the above expressions, and the total power is their sum.

Construction of Experimental Equipment

It was desired to have the experimental program serve in some measure as a proving ground for the equipment later to be procured for delivery to the contracting agency, and it was also desired to have as much as possible of the equipment either commercially available or conducive to the use of standard switch gear.

Electrodynamic shakers were the obviously practical means of delivering forces to the structure, variable in both frequency and magnitude and fixed in phase but reversible in sense.

Selection of the required force rating of the shakers, as well as the power-handling capacity of the variable frequency source, the distribution system, and the control system, was based on application of the amplitude and power relationships derived in the previous section. Typical mode shapes for aircraft structures of known mass distributions were analyzed, and it was concluded that the final system should consist of a variable frequency alternator having a capacity of 2.5 kva. at 100 cycles per sec. powering 24 shakers, each capable of delivering an alternating force of 25 lbs. through a stroke of $\pm 1/2$ in.

Alternator

An alternator was required to furnish good wave form at as low as 80 per cent power factor over a frequency range of from 4 cycles per sec. or lower to 100 cycles per sec. or higher. Although the standard 115-volt output at 60 cycles per sec. favored the use of standard switch gear, it seemed desirable to have a special alternator built rather than use a standard 60 cycles per sec. alternator. The specific advantages of the special alternator obtained are (1) reduction in harmonic content of the current output; (2) provision of forced cooling for low speed, high current operation; (3) specific design for rotational speeds required to produce 100 cycles per sec. output.

A consideration of the overall system requirements, discussed later, determined the required alternator rating.

Power Distribution

The power distribution system for the experimental work was essentially the same as that described later in connection with the final equipment. Essential elements in the control circuit were (1) a large Variac on the alternator output to control the supply to a feeder line and (2) smaller Variacs to control each shaker individually.

The current to each shaker from its Variac (and, hence, the force delivered) was reversible in direction by means of a standard switch.

Shaker Design Considerations

Elementary texts in either physics or electrical engineering show that, when a current is caused to flow in a conductor placed in a magnetic field, a force is exerted on the conductor perpendicular to the conductor and to the lines of magnetic flux. This relationship is expressed mathematically when reduced to pound-inch-second units by

$$i = 0.885 \times 10^{-7} BLIN \tag{20}$$

where

i = lbs. force
B = flux density = ϕ/A, lines per sq.in.
L = conductor length in flux field, in.
I = current, amp.
N = number of turns of length L in flux field

If we divide through by I, we have the relationship,

$$i/I = 0.885 \times 10^{-7} BLN \text{ (lbs. per amp.)} \tag{21}$$

For any particular shaker, B is a function of the field structure design and L and N are functions of the armature coil design.

Therefore, the force/current ratio is a constant for any given shaker (assuming constant field strength), which indicates its performance as an electromechanical transducer, in the conversion of current to force.

If we had only to produce large forces, it would be comparatively easy to do so by using an armature coil of many turns of small-diameter wire. However, it must be remembered that we wish to produce a force to act on a moving or resonating structure. In other

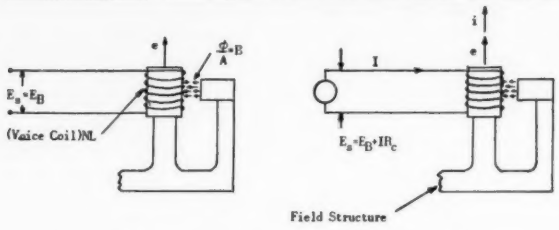

(a) Voice Coil Circuit Open

(b) Voice Coil Circuit Closed

Fig. 3 Schematic Diagram Shaker Relationships

words, it is not sufficient to produce a high "blocked armature" force, but we must so design the system that the force can be delivered for any expected velocity of the moving system—we must be able to deliver power to the mechanical system.

The second basic electromagnetic equation shows why it is difficult to maintain the current (and, hence, the force) when the armature is moving. This equation states that, when a conductor moves in a magnetic field, a voltage is generated. This voltage is such as to cause a current to flow in a closed conductor which will produce a force opposing the motion. For this reason, the generated voltage is known as a back voltage, and its value is given by the equation

$$E_B = 10^{-8}\, BLNe \tag{22}$$

or, dividing through by e,

$$E_B/e = 10^{-8}\, BLN \quad \text{(volts/in. per sec.)} \tag{23}$$

where E_B is the back voltage (volts) and e is the velocity of the moving conductors relative to the field (in. per sec.).

If we now solve for BLN from Eq. (21) and substitute in Eq. (23), we find

$$E_B/e = 0.1125\, i/I \tag{24}$$

That is, the higher a force/current ratio we design for, the higher a back voltage will be obtained for a given velocity.

By referring to Fig. 3a, it is seen that, when an open circuited coil is moved in a field, the open circuit voltage is equal to the back voltage.

On referring to Fig. 3b, it is seen that, in order to drive a current through the coil in a direction producing a force in phase with the velocity, it is necessary to have a supply voltage equal to the voltage drop through the coil electrical impedance plus the back voltage. That is,

$$E_S = IR_C + E_B \tag{25}$$

Thus, it is seen that provision of a high force/current ratio is not the complete answer to a suitable shaker design, because the higher this ratio, the more voltage is required to get current through the coil.

The proper approach to the design problem is through consideration of the mechanical mobility of the systems that will be driven and the matching of this mechanical load by a suitable reflected electrical impedance to a practicable power supply.

The impedance-mobility relationship is found by dividing Eq. (22) by the relationship $I = i/(i/I)$ after suitable transposition, giving

$$E_B/I = 0.1125(i/I)^2 e/i \tag{26}$$

or

$$R_B = 0.1125(i/I)^2 v \tag{26a}$$

where E_B/I is the reflected impedance (resistive at resonance) and e/i is the ratio of the velocity of the driven system to the force applied or the mechanical mobility of the system being shaken.

When the two latter quantities are evaluated, then the required i/I is established. Following Eq. (21), it was remarked that this factor is controlled by B, or field coil design, and the quantities L and N that belong to the armature coil design. Actually, the two designs are closely interrelated.

The practical limitation of current for any given armature coil is dependent on the I^2R power losses that can be dissipated without exceeding commercially acceptable temperature rises. A similar limitation applies to the design of the field coil. The magnetic flux obtainable with a given structure design is also dependent on the material properties affecting magnetic reluctance.

A further design consideration was necessary in attempting to provide the maximum force output possible with a shaker still light enough to be considered portable or movable by a single man. A shaker designed to meet these requirements was available, and, after due consideration of the mobility relationships, an armature coil having an i/I of approximately 3.5 was designed to provide a suitable match for the power supply.

Shaker System Characteristics

It is of paramount interest to know the characteristics of the overall power system in order to understand the source of various limitations.

For a given setting of the field excitation, the alternator terminal voltage at no load varies linearly with the alternator frequency, and the voltage at any particular frequency can be varied by a change in field excitation. It is desirable to have as high a voltage as possible at low frequencies, as will be seen later, and yet the output voltage at any frequency and light load must not be sufficient to cause saturation and distortion of the Variac controls.

It was determined experimentally that a suitable no-load terminal voltage curve produces not over 120 volts at 60 cycles per sec., and the alternator is operated at a fixed excitation.

The approximate relationships of the voltages and currents in the system may be better visualized by reference to Fig. 4, representing a single shaker connected to an alternator by means of a single Variac. (The second Variac, shown in the diagram of Fig. 10, may be considered to be set for a transformation ratio of unity.)

In the section on "Shaker Design Considerations," it was pointed out that one of the main factors governing the system design was the characteristic of the structure being shaken. It was further pointed out, in Eq. (26), that the electrical ratio of E_B/I was directly related to the mechanical ratio e/i through the force-current characteristic of the shaker. That is,

$$E_B/I = 0.1125\ (i/I)^2\ e/i$$

If a force i is applied to a certain structure at its resonant frequency, and the structure responds with a velocity e, then, since the characteristics of the electromechanical transducer or shaker are known, the electrical quantities I and E_B can be calculated as follows:

$$I = i/(i/I) \tag{27}$$

$$E_B = 0.1125(i/I)e \tag{28}$$

The voltage applied to the shaker terminals, E_S, must be equal to the back voltage E_B plus the voltage drop through the armature coil, IR_C.

$$E_S = E_B + IR_C \tag{29}$$

The shaker voltage is supplied through the autotransformer or Variac from the alternator terminal voltage E_T, which is related to E_S by the Variac setting or turns ratio N_1/N_2 as the alternator current is related to the shaker current.

$$E_T = E_s(N_1/N_2) = (N_1/N_2)\ (E_B + IR_C) \tag{30}$$

$$I_a = I(N_2/N_1) \tag{31}$$

Dividing Eq. (30) by Eq. (31) gives

$$\frac{E_T}{I_a} = \frac{E_S}{I}\left(\frac{N_1}{N_2}\right)^2 = \left(\frac{N_1}{N_2}\right)^2\left(\frac{E_B}{I} + R_C\right) \tag{32}$$

or

$$R_T = R_S(N_1/N_2)^2 = (N_1/N_2)^2(R_B + R_C) \tag{33}$$

That is, the terminating resistance of the alternator is equal to the effective shaker resistance times the square of the turns ratio set on the Variac. Also, it is seen that the effective shaker resistance, R_S, is equal to the reflected resistance of the mechanical load, R_B, plus the coil resistance, R_C.

R_T is therefore a function of the variables N_1/N_2 and R_B; R_T can be held constant for different values of R_B by means of a compensating setting of the Variac N_1/N_2. In addition, the terminal voltage E_T differs from the no-load voltage E_{NL} because of the internal resistance of the alternator, R_a, complicated by saturation and armature reaction effects.

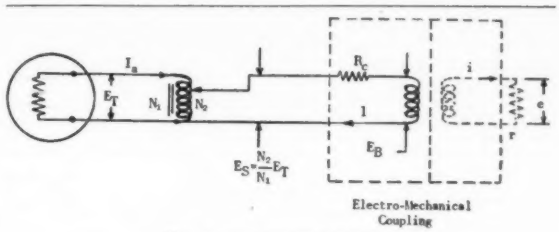

Fig. 4 Power Circuit Relationships

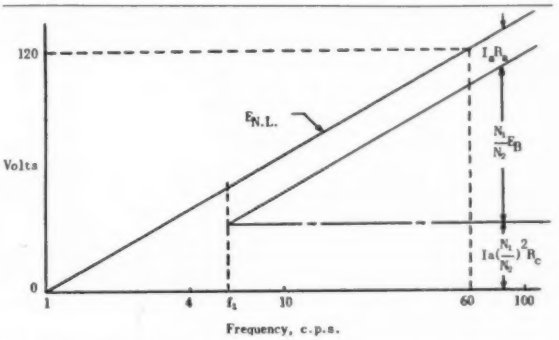

Fig. 5 System Voltage at Constant Current vs. Frequency and Variac Setting

It can now be seen that, for a given frequency of the alternator producing a certain no-load voltage E_{NL}, there will be a certain value of R_T which cannot be reduced without causing the current rating of the alternator to be exceeded.

$$I_a = \frac{E_{NL}}{(R_{a_{eff.}} + R_{T_{min.}})} \tag{34}$$

It can also be seen that, if R_B is low (a highly damped structure), the setting N_2 can be decreased [Eq. (33)], causing R_T to remain above the minimum value.

These relationships can be visualized as a function of varying alternator frequency by reference to Fig. 5. It will be noted that, for a certain assumed current, there is a certain frequency, f_1, at which all the available voltage, E_{NL}, is dissipated by losses, leaving none available to overcome E_B.

This simply means that a current equal to $(N_2/N_1)I_a$ can be pushed through the shaker coil at the frequency f_1 *only when it does not move* (blocked armature) and that, if the armature is allowed to act on the resonant structure, the current deliverable *must* be less.

It is obvious that the most critical design condition is at low frequency, where there is little voltage available from the alternator to overcome the voltage drop at high current values.

An understanding of the relationships between current, back voltage, power to the mechanical system, and losses is better realized by examination of Fig. 6, which shows these relationships at 4 cycles per sec. alternator frequency. The line E_T on this figure

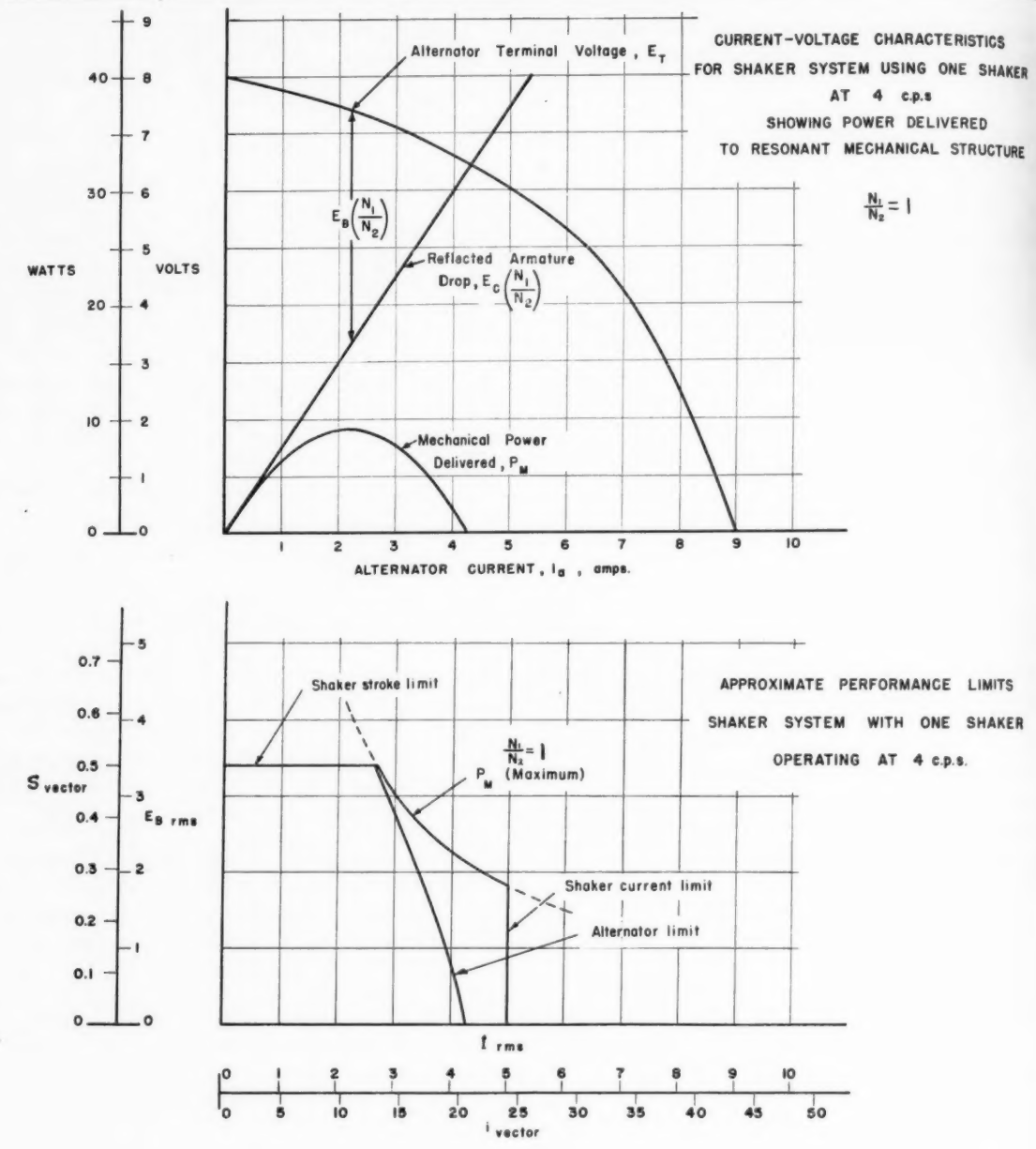

Fig. 6. System Characteristics - 1 Shaker at 4 c.p.s.

is the voltage available at the alternator terminals as a function of increasing current, based on the manufacturer's data. The line $E_C(N_1/N_2)$ represents the voltage drop due to IR_C losses in the armature coil and its connecting cable, as reflected to the alternator by the Variac turns ratio $N_1/N_2 = 1$. For any given current, then, the ordinate between these lines is equal to $E_B(N_1/N_2)$, as can be seen from Eq. (30).

Now, the power delivered to the mechanical structure being resonated is

$$P_M = E_B I = E_B I_a (N_1/N_2) \tag{35}$$

and, since $E_B(N_1/N_2)$ decreases as I_a increases, there is a particular value of I_a at which P_M is a maximum. From the P_M curve of Fig. 6, it is seen that a maximum power transfer to the mechanical system is obtained when $I_a = 2.1$ amp., at which time $E_B(N_1/N_2)$ is 4.32 volts.

The lower plot of Fig. 6 shows the approximate performance limits of the shaker system at 4 cycles per

FIG. 7. Experimental structure with variable damping, set up for test.

sec. It will be noted that, with the turns ratio setting of $N_1/N_2 = 1$ as shown, the maximum power cannot be delivered because the shaker stroke limit of 0.5 in. gives a maximum back voltage of only about 3.4 volts rather than the 4.32 volts required at maximum power.

Similar system limits of power delivery and E_B vs. I relationships can be drawn for other turns ratios within the possible range of about 0.8 to 50. Because of the alternator characteristic, however, only slightly higher limits than those indicated for $N_1/N_2 = 1$ are obtainable.

EXPERIMENTAL DEVELOPMENT

A test structure was devised to allow experimental evolution of a system whereby natural modes might be excited by application of orderly methods based on the concepts described earlier. In particular, it was desired to know:

(1) How good an approximation to a natural mode could be produced in a uniform structure when forces were adjusted proportional to the product of mass and amplitude at the station of force application.

(2) How much better this excitation was than some more arbitrary excitation.

(3) How satisfactory an excitation of pure modes might be obtained by the described method of force adjustment, even in cases of nonuniform structure with irregular damping characteristics.

The test structure as set up for testing is diagrammed schematically at the head of Fig. 8. The structure consisted of nine lumped masses interconnected by two continuous straps or flexures bolted to the top of the masses at each side and two identical flexures bolted to the bottom of the masses on each side. By this arrangement, the flexures constrain the masses to translate relative to each other along axes perpendicular to the flexures.

Motion of one mass relative to the next mass was resisted not only by the flexure forces but also by damping forces that were produced electrodynamically. Each mass, except the center one, consisted of a field struc-

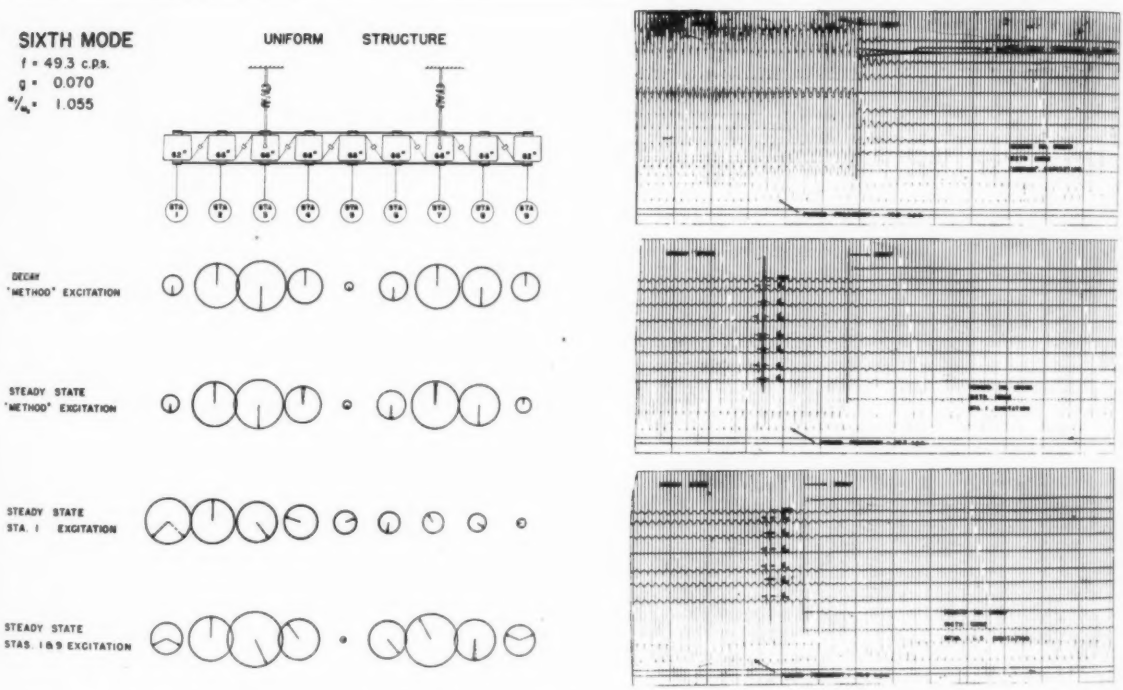

FIG. 8. Data obtained on the sixth natural mode of the symmetrical structure for various excitations. Oscillograph records show the following conditions: top—decay of structural mode from "method" excitation; middle—decay of same mode from excitation at Station 1; bottom—decay of same mode from excitation at Stations 1 and 9.

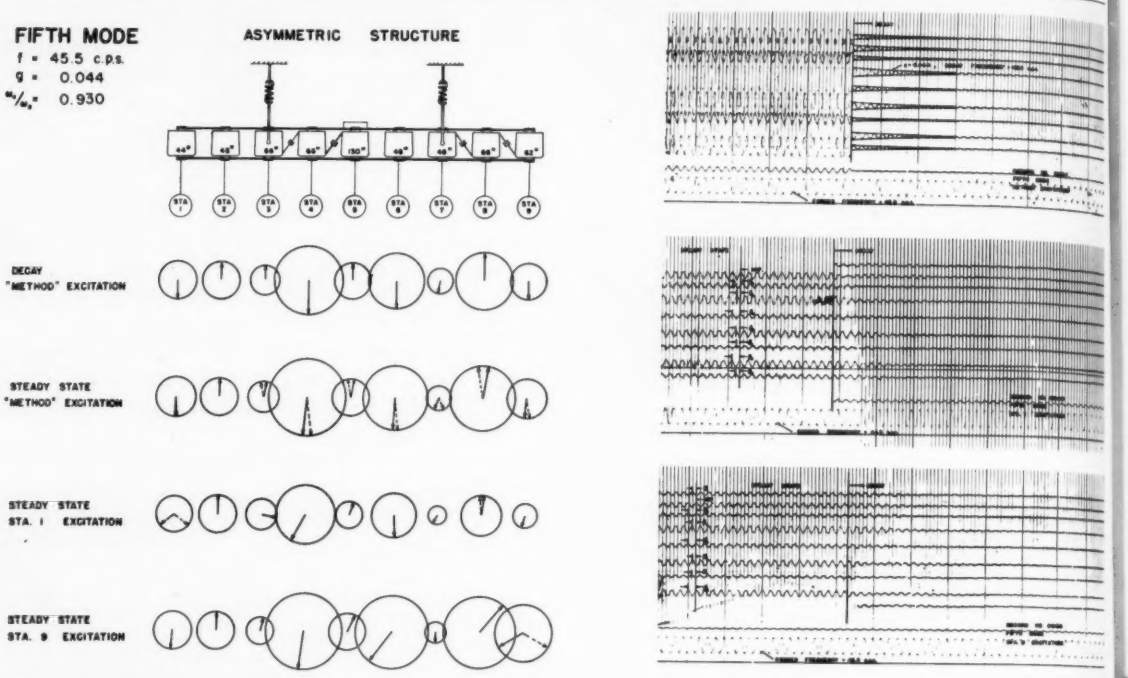

FIG. 9. Data obtained on the fifth natural mode of the asymmetric structure for various excitations. Oscillograph records show the following conditions: top—decay of structural mode from "method" excitation; middle—decay of same mode from excitation at Station 1; bottom—decay of same mode from excitation at Stations 1 and 9.

ture and field coil identical with those used for the experimental shakers. In the air gap of each mass other than the center one was a single shorted turn or tube as armature, which was rigidly attached to the next inboard mass. Thus, motion of one mass relative to another caused damping forces between the two masses.

The mass distribution of the test structure was changed by (a) adding lead blocks to the original mass and (b) removing the field coils. In the latter case, of course, the damping between the light mass and the next inboard mass was eliminated.

The damping distribution was changed by (a) removing the damper field excitation, (b) introducing a mixture of iron powder and oil into the flux gap, and (c) removing selected field coils, as in (b) above.

It was also possible to change the damping by a change in thickness of the damper tube or shorted turn. This variation was not found to be necessary.

Tests were made on two variations of the test structure: (a) a uniform structure, as diagrammed at the head of Fig. 8; (b) an asymmetrical structure, as diagrammed at the head of Fig. 9.

In the former case, masses, stiffnesses, and dampers were as near uniform as practicable, and, in the latter case, masses and dampers were made to differ in magnitude and placement in an asymmetrical fashion, with the stiffnesses remaining uniform between masses.

The test structure was supported from an overhead frame at a low frequency by means of springs attached near the nodes in the first free-free mode of the structure. A vibration pickup was attached to each mass element of the structure for measuring the steady-state amplitude at each mass station. A shaker was attached to each mass and was mounted below the test structure. Each shaker was controlled from a console, whose arrangement and auxiliary systems were evolved during the experimental program to allow systematic convergence on a natural mode excitation. This system, with refinements, is to be described later in connection with the final equipment, and further reference to it here will be omitted.

The test procedure, described more fully in reference 6, was to excite the test structure, first, by the method of pure mode synthesis devised and, then, in one or more arbitrary ways, but using good technique. In each case the amplitude of each mass was measured by means of its pickup, and phase relative to some reference was established. A record was also taken of the mode decay when the excitation was removed.

Experimental Results

Results of these tests are exemplified by Fig. 8, which shows comparative data for the various excitations applied to the sixth mode of the uniform structure, and Fig. 9, which shows similar data for the fifth mode of the asymmetric structure.

Evidence of the superiority of the multiple shaker adjustment is obvious in the purity of the decay record

and by the close degree of similarity between the steady-state and decay amplitude ratios obtained by the multiple excitation.

On the other hand, the amplitude ratios obtained from the arbitrary excitations bear little similarity to those in the pure mode, and the large phase shifts and poor decays give some indication of the obscurity in which data of this type would leave the analyst.

Referring to Fig. 8, some similarity between the mode shapes obtained in the various ways is observed on comparison of the absolute amplitudes of the masses. These values alone are of little value, however, especially on a continuous structure, unless the position of the nodes, indicating a reversal of phase, can be ascertained. The large phase shifts indicate the absence of true nodes on the structure and, hence, makes their location doubtful and only approximated painfully by careful amplitude surveys or phase analyses. The mode is obviously there but makes concise definition difficult, as shown in the poor decays.

Specifically, it can be concluded that the system of multiple shakers, adjusted according to a scheme based on the assumption of damping distributed in proportion to stiffness, offers a great clarification in direct experimental evaluation of mode properties not only for a structure that has the assumed damping distribution but also in at least some cases where the actual damping distribution departs radically from that assumption.

Approach to the Experimental Problem

The theoretical analysis indicated that, with an assumed simple distribution of damping and with multiple shakers distributed to act on each element of the equivalent lumped system, the natural modes could be excited by the adjustment of each shaker force to be proportional to the product of the assigned mass and its amplitude in the mode under excitation. That is,

$$i = cmf_i$$

Since the mass assigned to any shaker is a constant for a particular setup, it can be introduced as an electrical constant, attenuating the signal that must represent the magnitude of the adjusted shaker force. The shaker force is proportional to its armature current, which is regulated by the voltage across its control Variac. This voltage is attenuated by a potentiometer calibrated directly in mass ratio, and the resultant signal for each station, proportional to i/m, is placed on a switch whose selector goes to the horizontal axis of a cathode-ray oscillograph.

The amplitude of the mass in the mode f_i is measured by an accelerometer pickup attached directly to the shaker armature, which moves the mass. Its output is integrated to give proportionality to velocity, and the resultant signal for each station is applied to a switch whose selector goes to a normalizer and then to the vertical axis of the scope.

Proof that ratioing Variac voltage to pickup output is equivalent to ratioing force to amplitude is as follows. Since mass is a constant for each station, it will not be considered in the proof.

Let

E_{S_n} = Variac voltage at any station n
E_{p_n} = pickup output voltage at any station n
I_n = current in voice coil of shaker at station n (amp.)
i/I = calibration of shaker = constant (lbs. per amp.)
i_n = shaker force = $(i/I)\, I_n$ (lbs.)
s_n = amplitude of motion at station n (in.)

Then, following Eq. (29),

$$E_{S_n} = E_{B_n} + I_n R$$

and

$$E_{B_n} = 0.1125\ (i/I)e_n = 0.1125\ (i/I)2\pi f s_n \quad (39)^*$$

for a given mode $0.1125(i/I)2\pi f$ = constant A. Then,

$$E_{S_n} = As_n + [R/(i/I)]i_n \quad (40)$$

E_{p_n} = calibration constant · acceleration
= (const.) . $(2\pi f)^2 s_n$ = (const.) · s_n

$$E_{p_n} = Bs_n \quad (41)$$

then,

$$\frac{E_{S_n}}{E_{p_n}} = \frac{As_n}{Bs_n} + \frac{[R/(i/I)]i_n}{Bs_n}$$

$$E_{S_n}/E_{p_n} = (A/B) + [(R/B)/(i/I)](i_n/s_n) \quad (42)$$

If the adjustment is made such that $E_{S_n}/E_{p_n} = c$ for $n = 1, 2, 3, \ldots$, then i_n/s_n will have a constant ratio

$$i_n/s_n = (i/I)/(R/B)[c - (A/B)] \quad (43)$$

Procedure in Exciting a Natural Mode

Operation of the system in exciting a natural mode starts out with the introduction of alternating forces to the structure by means of only one of the many shakers driven from the same system. The frequency of excitation is varied until the structural response indicates proximity to a natural mode frequency. The electrical signals corresponding to the amplitude and force at this station are selected on the cathode-ray oscilloscope. As the resonant frequency is approached, the velocity of the structure approaches an in-phase condition with the force; hence, the observed figure is an ellipse of variable fineness ratio. The gain controls on the scope are adjusted to give the major axis of this ellipse a 45° slope. By selecting another station, its force may be adjusted proportional to its amplitude merely by adjusting the Variac to obtain a 45° slope of the observed ellipse.

Energy introduced into the system by the second force will cause the amplitude of response to increase, thereby

* There are no Eqs. (36)–(38).

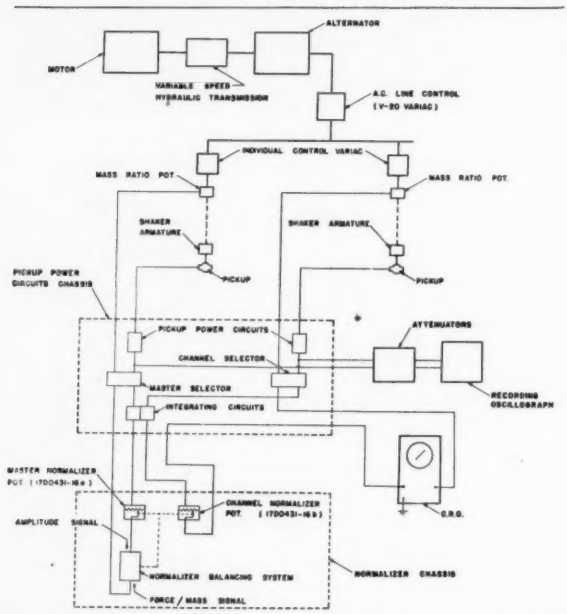

FIG. 10. Schematic diagram of complete system for exciting pure natural modes.

changing the ratio of force to amplitude at the first station. The purpose of the normalizer is to maintain the signal to the scope constant (producing a 45° ellipse) for the changed ratio of amplitude to force at the first (or master) station. This is done by dividing the increased pickup output of the first station by a quantity sufficient to re-establish the original ratio of signals to the oscilloscope and dividing any other selected pickup output by the same quantity. This is essentially a normalization, automatically performed as described later. By this means, each successive force is brought into adjustment to succeedingly better approximations to the finally required constant ratio of force to amplitude, and readjustment of only the first few forces is required to obtain the desired condition:

$$\frac{(i/m)_1}{s_1} = \frac{(i/m)_2}{s_2} = \frac{(i/m)_3}{s_3} = c$$

Before turning on another shaker at a selected station, it is necessary to make sure that its force, when applied, will act in the proper sense, putting energy into the system rather than drawing it out. Application of the original force at the master station evoked a velocity response of the structure that was in phase at that station, and the phase of every other point in the structure (in the natural mode in question) is either in or out of phase with this motion. Since the force applied is measured by the Variac voltage and the phase of all Variacs is the same, the phase of the structural response at any station can be found by comparing the velocity signal from the pickup with the Variac voltage before the shaker circuit is closed. The wiring can then be arranged so that an in-phase indication will produce a lissajous figure to the right, calling for a phase-switch position to the right. Similarly, a lissajous figure with axis inclined to the left requires a phase-switch setting to the left. After this adjustment is made, the shaker can be turned on and adjusted to level as previously described.

It is an experimental fact that, although phase shifts between the responses at various stations may be large under the excitation of the first applied force even when adjusted to a resonant frequency, as more and more forces are applied and adjusted the more uniform in phase are the various points on the structure. This is to be expected. Since we end up with adjustments urging the structure at each of 24 points to move in the natural mode form, we have an excitation practically orthogonal to all other modes.

This means that, with the shakers so adjusted as to phase and force amplitude, the structural response will be in the one mode *regardless of the frequency of excita-*

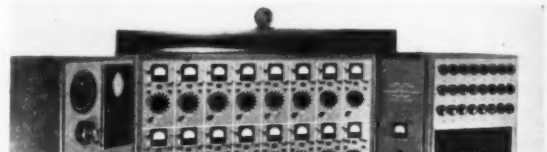

FIG. 11. Control console for systematic excitation of pure natural modes. Contains all power supplies, instruments, and control circuits for 24 shakers and associated pickups. Data recorded by oscillograph housed in bay at right.

FIG. 12. Shaker with accelerometer attached.

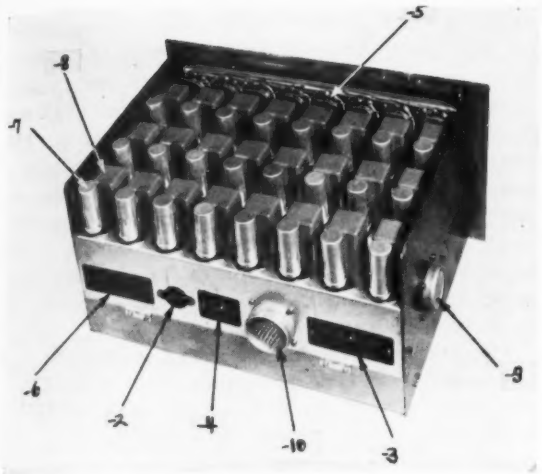

FIG. 13. Chassis containing all master and channel selectors, with 24 pickup coupling circuits and sensitivity adjustments. Note: Dash numbers refer to drawing No. 17CO447.

tion. The frequency can, of course, be adjusted to obtain a maximum velocity amplitude as indicated on the scope or to obtain an in-phase adjustment of force and velocity as indicated by degeneration of the observed ellipse to a straight line.

THE FULL-SCALE EQUIPMENT

A schematic diagram of the overall system is shown in Fig. 10. The complete system (exclusive of shakers) was housed in a control console requiring but a single connection to a 220 volt, three-phase power line.

Thirty shakers were provided, any 24 of which could be controlled from the console. All cables have stowage space in the console. The essential features of the variable frequency power supply and distribution system have been discussed earlier, and it is now in order to describe some of the more important features of the instrumentation and control circuits provided.

Pickups

A pickup is attached directly to each shaker armature. Thus, with a single attachment to the structure, the force applied and the amplitude resulting at the point are obtained.

The pickup signal is used in two ways: (1) to provide an amplitude signal for reference in the adjustment of shaker force and (2) to provide simultaneous signals for recording the resultant structural motion on a multichannel oscillograph.

The pickup used was of a new type, allowing the operation of the oscillograph elements without amplification, which affected a considerable degree of simplification in the instrumentation and its maintenance. Coupling circuits for each of the 24 channels are carried on a single rack mounting panel. Provision is made for convenient calibration of the pickups either on an absolute or comparative basis. The latter is generally sufficient for mode-shape measurements. Sensitivity adjustments are provided for each channel, and means are also provided for rapid overall electrical calibrations of the several attenuator-oscillograph element combinations.

The pickups used are of 15*g* capacity and about 275 cycles per sec. natural frequency. Their voltage sensitivity exceeds 0.5 volt per *g* and, when coupled to the oscillograph, give signals flat in amplitude response to the required 100 cycles per sec. with a sensitivity of 25 in. of record deflection per *g*, thus making adequately clear the need for attenuation at reasonable acceleration levels and the ability to produce good record deflections at low structural accelerations.

Normalizer

A simplified diagram of the normalizer is shown in Fig. 15. The amplitude and force signals from any particular station, selected as master, are fed to the normalizer.

The pickup output from this station is applied to the master potentiometer, from whence the attenuated signal goes through a current amplifier and is applied to the heater element of an isolated construction vacuum thermocouple. At the same time, the output of the mass-ratioing potentiometer (force divided by mass) is applied to a similar thermocouple. The

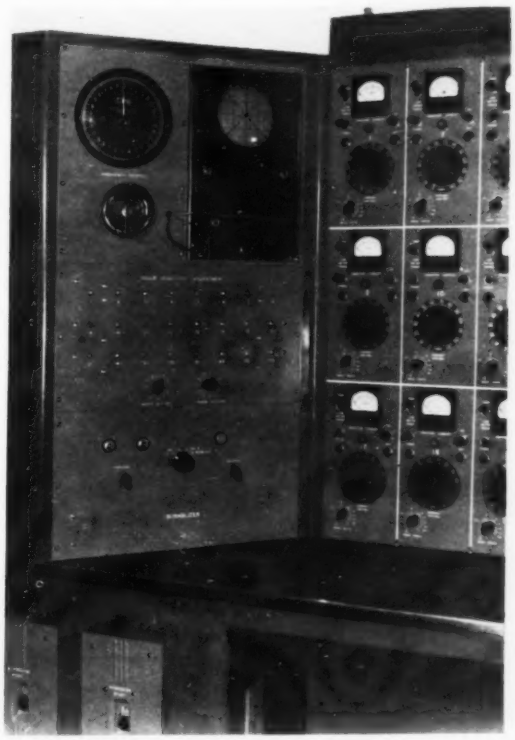

FIG. 14. Left panel of control console, showing typical control stations, frequency control, scope indicator, master and channel selectors, and normalizer.

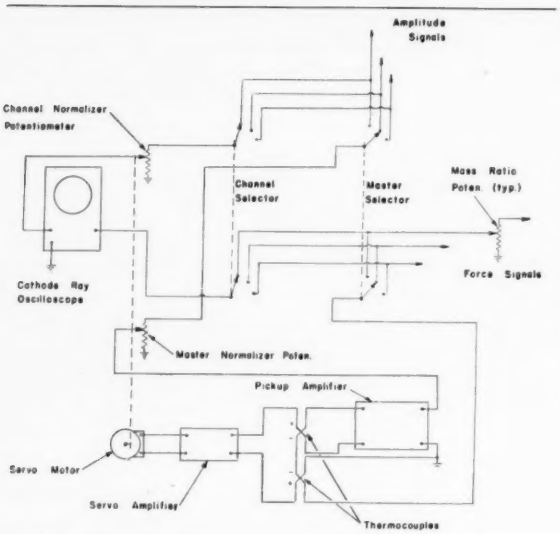

FIG. 15. Simplified schematic diagram of normalizer.

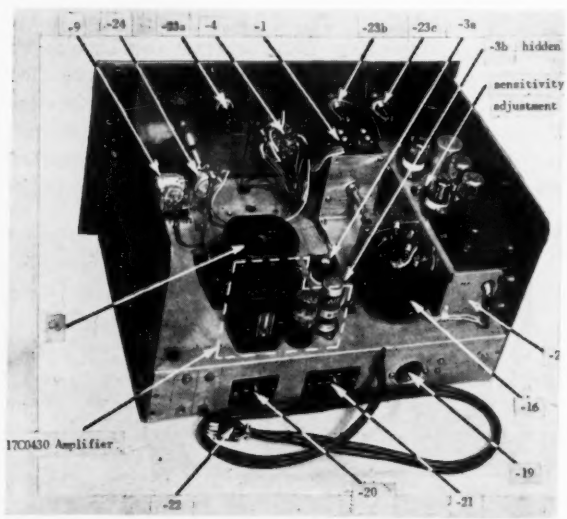

FIG. 16. Normalizer chassis, showing servo amplifier and motor, dual potentiometer, thermocouples, and automatic overload protectors. Note: Dash numbers refer to drawing No. 17DO431.

outputs of the two thermocouples are connected in series opposition and are applied to a d.c. servo-amplifier and associated balancing motor. If the current through each thermocouple heater is the same, it is seen that their outputs cancel and there is no input to the servo-amplifier. If the current through the pickup thermocouple exceeds that through the force signal thermocouple, a polarized signal is applied to the servo-amplifier and causes the balancing motor to rotate in a certain direction. The master potentiometer is geared to the motor in such a manner that its output is further attenuated until the outputs of the two thermocouples again cancel. Conversely, if the output of the force signal thermocouple exceeds that of the pickup thermocouple, a signal of the opposite polarity is applied to the amplifier motor combination and the direction of rotation is reversed. The master potentiometer is now driven so that it attenuates the pickup signal to a lesser extent until the system again comes into balance. The normalizing potentiometer is identical to the master potentiometer and is geared to the motor so that its motion is the same as that of the master potentiometer. Thus, the output of any pickup applied to the normalizer potentiometer through the pickup selector switch is divided in the same ratio and is thereby effectively normalized.

The normalizer assembly utilizes a standard and commercially available servomotor and amplifier.

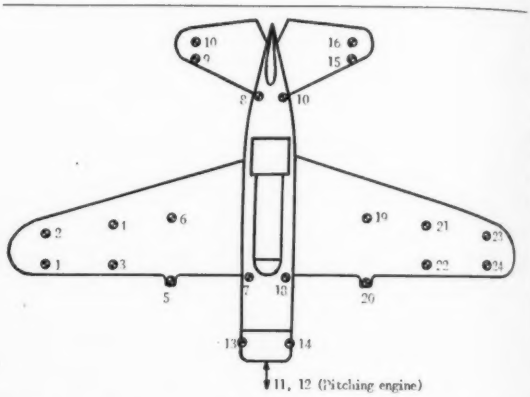

Shaker Channel No	Assigned Weight	Mass Ratio
1, 2, 23, 24	75 Lbs.	1.14
3, 4, 21, 22	152	2.28
7, 18	1286	19.5
9, 10, 15, 16	66	1.0
8, 17	450	6.8
13, 14	1707	25.9 (15)
11, 12	—	(15)

Note: Value of Mass ratio in ( ) for shakers 11, 12, 13 & 14 actually used.

FIG. 17. Shaker locations and mass ratios for SB2C-5 symmetric modes.

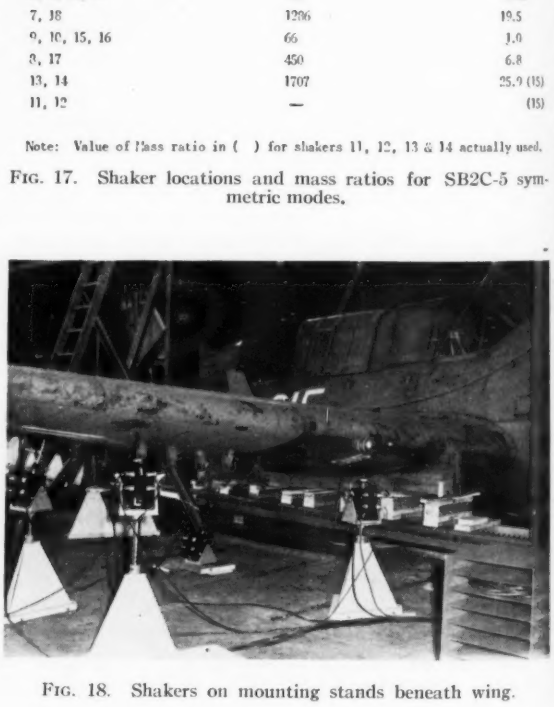

FIG. 18. Shakers on mounting stands beneath wing.

Provision for Setup

The first actual tryout of the equipment was made, after delivery, on an SB2C-5 airplane. A diagram of the shaker locations and mass ratio assignments is shown in Fig. 17. To facilitate locating the large number of shakers used on such a setup, a demountable stand was provided. The top section consisted of a plywood pyramid with a metal mounting table adjustable in height from approximately 25 to 43 in. on a coarse lead screw provided with a clamp. Either one or two subsections, each assembled from flat plywood sections with trunk latches, could be used, thus providing a maximum height of shaker attachment of 83 in.

Attachment to the structure was made by means of metal plates provided with tapped bushings and either cemented to the structure over a thin intermediary layer of sponge rubber or screwed to existing convenient locations.

Connection between the shaker-mounted accelerometer and the structure was made by means of the rod and flexure arrangement. The rod and flexure links provide a simple means of compensating for misalignment and provide a safety link to prevent inadvertent overload of the shaker armature by excessive motion of the aircraft, which is generally spring-supported.

Initial Full-Scale Tests

Records of three modes set up during the first test runs are shown in Fig. 21. These are acceleration records, and it will be noted that the amplitude ratios are clearly definable in either the steady-state or the decay portions of the records. The modes meet the criterion of purity, as evidenced by the lack of beats in the decays.

Some hash is in evidence on the acceleration traces, particularly due to excitation of the transient caused by abrupt removal of the shaker excitations. Some of this hash is due to pickup of miscellaneous structural buzz and rattle, and some is due to excitation of the pickup natural frequency. It should be pointed out in this connection that use of a phase criterion in setting up the modes requires uniformity of phase response, as well as a minimized phase shift. For this reason, the pickups are not damped to the conventional 65 per cent of critical. In any case, the hash does not seem to be of serious consequence in view of the clarity of the recorded modes.

Comments on Operation of Equipment

It is worth remarking that the modes recorded in Fig. 21 were set up, or synthesized, experimentally without any direct reference to the aircraft structure. Rather, the shaker force adjustments were made at the control console solely by reference to the cathode-ray oscilloscope for information as to required adjustments in frequency, phase of shakers, or force.

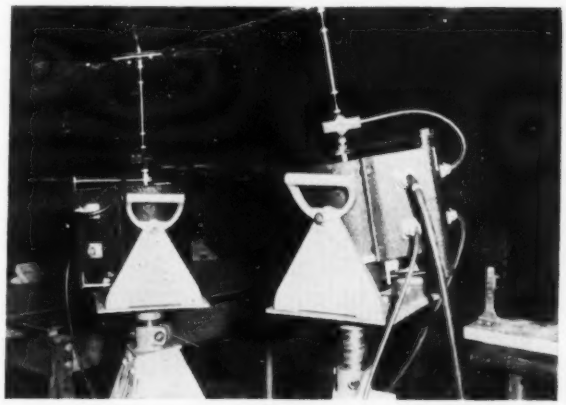

FIG. 19. Attachment of shakers to structure.

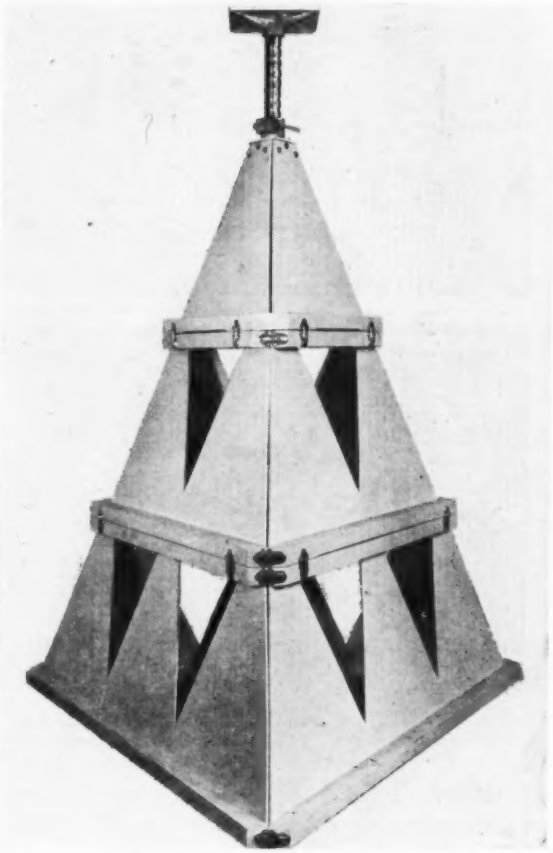

FIG. 20. Adjustable and demountable shaker stand.

It is further worth remembering that this orderly experimental method of natural mode synthesis bases its action in force adjustment on a specific and simple assumption of damping distribution. Its virtue, therefore, must not be expected to lie in either its exactitude or its infallibility but rather in its ability to yield any useful result in a complicated experimental situation. This can only be fully appreciated by one who is faced

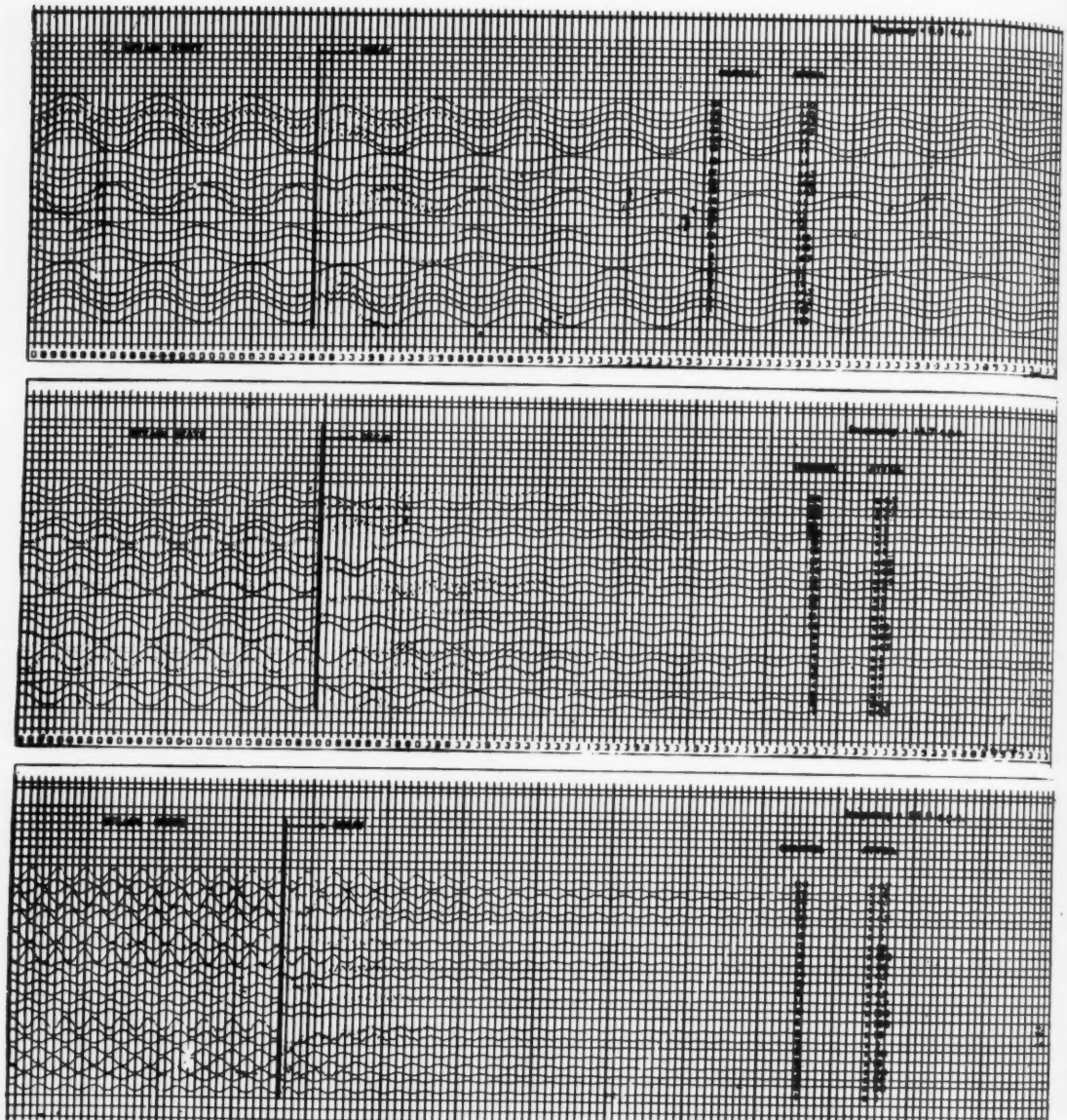

FIG. 21. Recorded structural modes of the SB2C-5 airplane excited with equipment. Freedom from beats is evident in the decays shown for modes at 8.4, 14.7, and 26.5 cycles per sec. Attenuation on the various traces of acceleration response varies from 1 to 100.

with the myriad uncoordinated adjustments possible in a multiple shaker setup.

The criteria of any natural mode, whether excited by a single- or a multiple-shaker system, are in its ability to exist in the steady state without phase shifts or to decay without beats. In many practical cases, moderate phase shift or beating is not intolerable. Should the orderly system devised fail in this practical test, it will do so because the adjustments made are called for by an assumption that is violated. It then becomes a matter of individual insight and common sense on the part of the operator in modifying these adjustments *better to meet the criteria*.

It is of particular importance to note that the operating adjustments are to be based on phase comparisons. If and when a single mode is excited to the major exclusion of all others, the motion of all points will be in (or 180° out of) phase, regardless of the proximity to the natural mode frequency. It is therefore evident that a valid experimental evaluation of the in-phase condition requires a high degree of uniformity in the phase response of the pickup circuits, which must be verified. The in-phase condition of force and velocity is conveniently used as a criterion for the frequency setting. It must be realized that the absolute phase shift of the circuits may be appreciable even though the

relative phase shift between circuits is negligible, and, therefore, such frequency adjustments are not accurately the mode natural frequency. This in itself is not too important, for, if the excitation is orthogonal, the mode response will still be in phase, but not at maximum amplitude, and the true frequency will become evident on the decay. Complication with regard to the frequency adjustment arises in actual cases where two modes are close together in frequency.

In following the procedure set up in the experimental method, it is desired to make convergence on one or the other of these modes. Bringing in successive shakers tends to produce large phase shifts in the responses because of elimination of one of the near-resonant modes. If, under these conditions, readjustment of the frequency is made to close the ellipse formed by force and velocity signals, the change in frequency may be sufficient to cause a node line to shift from one side of a shaker to another because of the effect of changed frequency on the two as yet unseparated modes. Under these conditions the incorrectly phased shaker will draw power from the system. Either the adjustments become divergent or the frequency is again changed and the other mode chased inconclusively. This tendency must be guarded against by awareness of the operator: (1) that both frequency and force distribution are changing the indicated phases; (2) that the indicated phases are not necessarily absolute and, therefore, that the true mode frequency is not necessarily obtained with the force-velocity ellipse closed; and (3) that, even without the true mode frequency, convergence on one mode will be indicated by the same phase shift at all stations.

Conclusions

A coordinated set of equipment has been provided for the experimental evaluation of the pure modes of complex structure. The equipment has been made as simple in operation as possible under the complex requirements of its use.

It has been shown that the multiple shaker system may be adjusted to excite pure natural modes in accordance with a simple procedure, utilizing an automatic normalizer and signals readily interpreted as to phase, frequency, and amplitude on a cathode-ray oscilloscope.

If and when this method, based on a simplified assumption of damping distribution, fails to produce a pure mode, it will be evident on the directly recorded data. In such cases, the adjustments may be modified with full ability to evaluate the effects on the structure.

Much careful attention has been given to providing a complete set of equipment in which the power circuits and instrument circuits are basically simple and utilize commercially available components. Coordination of the extensive equipment required into a single console has helped to provide quick and reliable means of overall check-out on the circuits prior to or during tests.

It is hoped that the emphasis on application of experimental techniques during the test period will be amply repaid by the quality of the data obtained and the savings in data analysis and reduction time.

Appendix—Normal Mode Theory

A complete mathematical treatment of the theory of small oscillations of conservative systems and of systems with small damping may be found in reference 3, chapters 5 and 6, and reference 4, Section 4. The results of these analyses have been summarized below. Reference 5 was an invaluable aid in making this summary.

Conservative Systems

Free Oscillation.—Lagrange's equation of motion for the free vibrations of a conservative system is

$$(d/dt)\,(\partial T/\partial \dot{q}_i) + (\partial U/\partial q_i) = Q_i = 0$$

where T and U are kinetic and potential energies, respectively, q_i are the generalized coordinates ($i = 1, 2, \ldots n$), and Q_i are the corresponding generalized external forces ($Q_i = 0$ for free oscillation).

The most general form of oscillation of such a system, with static coupling only, is represented by the superposition of n pure harmonics,

$$q_i = \sum_{r=1}^{n} A_i^{(r)} \sin(\omega_r t + \psi_r)$$

If the amplitudes of the principal oscillations are introduced by putting $A_i^{(r)} = \phi_i^{(r)} c_r$, it is possible to evaluate T and U in terms of the principal oscillations. Further, using the normalizing condition

$$\sum_{i=1}^{n} m_i \phi_r^{(r)2} = M$$

and calling

$$\xi_r = c_r \sin(\omega_r t + \psi_r)$$

the displacement of the rth *normal* mode, then,

$$T = (1/2)M \sum_{r=1}^{n} \dot{\xi}_r^2$$

$$U = (1/2)M \sum_{r=1}^{n} \omega_r^2 \xi_r^2$$

and the equations of motion become simply

$$\ddot{\xi}_r + \omega_r^2 \xi_r = 0$$

The kinetic and potential energies of the original system are seen to be the sums of the kinetic and potential energies of n single degree of freedom systems of mass M with a spring constant $K_r = M\omega_r^2$.

Forced Oscillations.—The equations of motion for the same system under the action of periodic external forces are

$$\frac{d}{dt}\left(\frac{\partial T}{\partial \dot{q}_i}\right) + \frac{\partial u}{\partial q_i} = F_i \sin(\omega t + \psi)$$

where F_i is the amplitude of the ith component of the generalized force. The component of F_i corresponding to the displacement of the rth normal mode is

$$\Phi_r = \sum_{i=1}^{n} F_i \phi_i^{(r)}$$

The equations of motion in terms of the normal coordinates ξ_r and the normal force components Φ_r are

$$\ddot{\xi}_r + \omega_r^2 \xi_r = (\Phi_r/M) \sin(\omega t + \psi)$$

The steady-state solution is

$$\xi_r = \frac{\Phi_r}{K_r} \frac{1}{1 - (\omega/\omega_r)^2} \sin(\omega t + \psi)$$

If $\omega^2 \rightarrow \omega_r^2$, resonance occurs, and the amplitudes of all normal modes are small compared to the rth mode. The amplitude ratios of the forced vibration are approximately equal to the amplitude ratios of the rth normal mode.

Damping (Nonconservative Systems)

Viscous Damping.—If, now, forces that are linear functions of the velocity components $\dot{q}_i$ ($i = 1, 2, \ldots, n$) are introduced to the system described above, Lagrange's equation becomes

$$\frac{d}{dt}\left(\frac{\partial T}{\partial \dot{q}_i}\right) + \frac{\partial D}{\partial \dot{q}_i} + \frac{\partial u}{\partial q_i} = Q_i$$

where T and U are kinetic and potential energies as before. D is the dissipation function, and Q_i are the generalized external forces corresponding to the generalized coordinate q_i.

In terms of the normal coordinates of the undamped system, the equations of motion for free vibrations are

$$M\ddot{\xi}_r + \sum_{s=1}^{n} \beta_{rs}\dot{\xi}_s + K_r\xi_r = 0$$

were β_{rs} are constant damping coefficients. Furthermore, if the dissipation is small (i.e., $\beta_{rs} \ll M$ and $\beta_{rs} \ll K_r$), the rth solution of Eq. (10) is largely made up of ξ_r, which is the solution of

$$M\ddot{\xi}_r + \beta_{rr}\dot{\xi}_r + K_r\xi_r = 0$$

and small ξ_s's whose amplitude and phase are given by

$$\xi_s = \xi_r[\beta_{rs}\,\omega_r/(M\omega_r^2 + K_s)]$$

and ω_r is the complex root of

$$M\,\omega_r^2 + \beta_{rr}\,\omega_r + K_r = 0$$

The imaginary part of this complex root gives the decay frequency that is nearly the undamped natural frequency. The real part is a measure of the rate of decay.

In the case of forced oscillations of the slightly damped structure ($Q_i = F_i \sin \omega t$), the equations of motion in terms of the normal coordinates of the conservative system are

$$M\ddot{\xi}_r + \sum_{s=1}^{n} \beta_{rs}\dot{\xi}_s + K_r\xi_r = \Phi_r \sin \omega t$$

Again, for small values of β_{rr}, the cross terms β_{rs} are virtually negligible, and the solution is predominantly

$$\xi_r = \frac{\Phi_r}{K} \frac{1}{\sqrt{\left[1 - \left(\frac{\omega}{\omega_r}\right)^2\right]^2 + \left(\frac{\beta_{rr}\omega}{K_r}\right)^2}} \sin \omega t + \theta$$

$$\theta = \tan^{-1}\left\{(\beta_{rr}\,\omega/K_r)/[1 - (\omega/\omega_r)^2]\right\}$$

This is recognized as the solution for the forced oscillation of a single degree of freedom system with viscous damping.

Special Case.—Of particular interest is the type of damping that is proportional to, and in quadrature with, displacement. The equation of motion in terms of the normal coordinates of the conservative system are

$$M\ddot{\xi}_r + K_r(\xi_r + j\sum_{s=1}^{n} g_{rs}\xi_s) = \Phi_r \sin \omega t$$

Again, for small dissipation (i.e., $g_{rr} \ll 1$), the rth solution is predominantly the solution of

$$M\ddot{\xi}_r + K_r(1 + jg_{rr})\xi_r = \Phi_r \sin \omega t$$

For the free oscillation ($\Phi_r = 0$), the decay frequency will be approximately $\omega_r = \sqrt{K_r/M}$ and the rate of decay is approximately equal to that of a single degree of freedom system with a viscous damping coefficient $\beta_{rr}/\beta_{crit.} = (1/2)g_{rr}$.

The solution of the equation for forced vibration is

$$\xi_r = \frac{\Phi_r}{K_r} \frac{1}{\sqrt{\left[\left(\frac{\omega}{\omega_r}\right)^2 - 1\right]^2 + g_{rr}^2}} \sin(\omega t + \theta)$$

$$\theta = \tan^{-1}\left\{g_{rr}/[(\omega/\omega_r)^2 - 1]\right\}$$

References

[1a] Bisplinghoff, R. L., Isakson, G., Pian, T. H. H., Flomenhoft, H. I., and O'Brien, T. F., *An Investigation of Stresses in Aircraft Structures Under Dynamic Loading*, M.I.T., Aero-Elastic and Structures Research.

[1b] Rauscher, M., Zartarian, G., and Haley, S. M., *Theoretical & Experimental Methods of Flutter Analysis*, Vol. 1, Phase 1, *Comparison of Theoretical Methods of Calculating Vibration Modes and Flutter Speeds*, M.I.T., Aero-Elastic and Structures Research.

[2] Civil Air Regulations, Part 4b Airplane Airworthiness—Transport, Category II 4b.321, Civil Aeronautics Board.

[3] von Kármán, Th., and Biot, M. A., *Mathematical Methods in Engineering*, 1st Ed.; McGraw-Hill Book Company, Inc., New York, 1940.

(*Continued on page 735*)

The Flow over a Wedge Profile at Mach Number 1

G. GUDERLEY* AND H. YOSHIHARA†
Wright-Patterson Air Force Base

SUMMARY

The flow over a wedge-shaped profile at zero angle of attack and with a free-stream Mach Number of 1 is computed using the hodograph method as simplified by the transonic law of similarity. Drag coefficients are computed for several profiles.

(1) INTRODUCTION

THE FLOW PATTERN over a two-dimensional profile with the free-stream Mach Number of 1 has been discussed previously.[1] The example given there showed that steady flow patterns at Mach Number 1 do exist. However, in the example computed there, the contour of the body is not suitable to carry out further investigations—e.g., to determine the influence of an angle of attack. For this purpose the study of a wedge profile is more promising. Furthermore, such a problem represents an example where the boundaries in the physical plane are predetermined so that it does have an interest of its own.

The formulation of the boundary value problem in the hodograph plane does not offer essential difficulties. The singularity that arises at the point of the hodograph which corresponds to the free-stream velocity has already been investigated.[1] Also, a family of particular solutions suitable to fulfill the boundary conditions by a superposition is easily found. Serious difficulties, however, are found when one tries to carry out this superposition such that the boundary conditions are actually fulfilled. A direct attack leads to an infinite system of equations. One might attempt to fulfill this system directly by taking a finite number of terms in the system; however, this procedure did not prove too satisfactory.

The present paper shows how to overcome this difficulty. First, the boundary value problem is changed in such a way that the solution remains the same while the supersonic part of the boundary is more conveniently located. This change does not yet eliminate the necessity of solving an infinite system of equations, but it reduces considerably the amount of work required to establish this system. Furthermore, in the present case of zero angle of attack, the problem can be formulated in terms of an integral equation whose kernel in a close approximation corresponds to that appearing in the theory of a thin airfoil in an incompressible flow. Thus, the solution finally requires only a suitable Fourier analysis of the boundary conditions.

Received March 9, 1949. Revised and received January 17, 1950.

* Wind Tunnel Branch, Aircraft Laboratory.
† Office of Air Research.

(2) BASIC RELATIONS

Let x and y be the Cartesian coordinates in the physical plane; w, the absolute magnitude of the velocity vector; θ, the inclination of the velocity vector with the x-axis; p, the pressure; ρ, the density; a, the velocity of sound; ψ, the stream function; φ, Legendre's transformed potential; w^*, the critical velocity at which $w = a$; and k the ratio of the specific heats (k = constant = 1.4).

If one introduces the quantity η by means of the relation

$$\eta = (k+1)^{1/3}\,[(w - w^*)/w^*] \tag{1}$$

then the differential equation for the stream function simplified by the transonic law of similarity assumes the form

$$\psi_{\eta\eta} - \eta\psi_{\theta\theta} = 0 \tag{2}$$

Similarly, the transformed potential can be expressed as

$$\varphi_{\eta\eta} - \eta\varphi_{\theta\theta} = 0 \tag{3}$$

The values of the x and y coordinates in the physical plane corresponding to a certain point (η, θ) in the hodograph plane, within the above approximation, are given by the expressions

$$\left.\begin{aligned} x(\eta,\theta) &= [(k+1)^{1/3}/a_0 w^*]\varphi_\eta \\ y(\eta,\theta) &= (1/a_0 w^*)\varphi_\theta \end{aligned}\right\} \tag{4}$$

Here, a_0 is the velocity of sound for the stagnation condition.

In general, the boundary value problem in the hodograph plane will be given in terms of the stream function. This formulation has the advantage that along the boundaries one has conditions that correspond to a standard form of boundary value problems—that is, to a case in which the value of the function to be determined is prescribed at the boundaries. However, because of the relation

$$\psi = \rho^*\varphi_\theta \tag{5}$$

which connects the transformed potential with the stream function, the boundary value problem can be easily expressed in terms of the transformed potential.

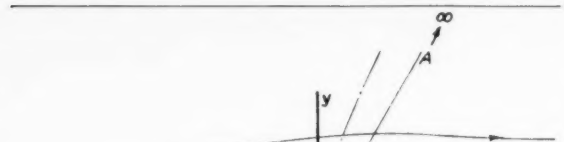

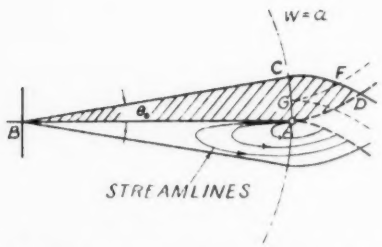

FIG. 1a (*top*). Flow in the physical plane. FIG. 1b (*bottom*). Flow in the hodograph plane.

This form is more suitable in the transformation back to the physical plane.

The pressure coefficient C_p is expressed in terms of η by means of the equation

$$C_p \equiv (p - p^*)/(\rho^* \cdot w^{*2}/2) = -2(k+1)^{-1/3}\eta \quad (6)$$

This form is consistent with the above approximations.

The characteristics in the hodograph plane of the Eq. (2) or (3) are given by

$$\theta \pm (2/3)\eta^{3/2} = \text{const.} \quad (7)$$

where the plus and the minus signs refer to the two possible families. The corresponding directions of the Mach waves in the physical plane are given by

$$dy/dx = \pm(k+1)^{-1/3}\eta^{-1/2} \quad (8)$$

Here, the signs are to be used consistently with those of Eq. (7). Note also from Eq. (1) that positive values of η represent supersonic velocities, while negative values correspond to subsonic velocities, so that only the former give real characteristics as is obviously required.

(3) The Boundary Value Problem for the Wedge

The hodograph representation of the boundary value problem for the flow over a wedge with the free-stream Mach Number of 1 is given in Fig. 1b; the flow in the physical plane is given in Fig. 1a (In the following description only the flow in the upper half-plane will be described, since the flow in the lower half is the same.)

All stream lines start at negative infinity of the physical plane with the free-stream sonic velocity. Accordingly, they all begin at point A, which represents a singular point.

The upper half of the physical plane is limited by the zero stream line. Let us follow the zero stream line in the hodograph plane. It starts at infinity with the sonic velocity (point A). As one proceeds along the zero stream line toward the profile, the velocity vector will always have a horizontal direction, and its magnitude will decrease. Accordingly, the map of this portion will lie along the line AB. At the nose of the wedge one has a stagnation point; the nose of the profile will therefore correspond to point B. Here a branch point of the stream lines arises, and the zero stream line then follows the side of the wedge which has a constant slope (line BC). The side of the wedge is now assumed to end with a convex corner at point C. At the convex corner one obtains the sonic speed; the sonic line will therefore start from point C. The flow over this corner will result in a Meyer expansion. The boundary stream line will therefore map to a characteristic of the hodograph plane. (Considerations of this kind are carried out in detail in reference 2.) The amount of expansion occurring in the flow over the corner depends upon the change of direction taking place at this point.

In general, only a certain portion of this expansion is of importance for the subsonic part of the flow pattern. This can be seen as follows: In the previous example of a flow with a free-stream Mach Number 1,[1] two classes of Mach waves that start at the body could be differentiated. The Mach waves of the first class end at the sonic line, while the Mach waves of the second class never reach the sonic line. If the contour of the body is changed such that the resulting perturbation propagates along one of the Mach waves of the first class, then this perturbation will reach the sonic line and thus influence the subsonic part of the field. A perturbation that travels along one of the Mach waves of the second class has no effect upon the subsonic part of the flow. There exists one Mach wave that is the last to reach the sonic line and thus separates the above two classes; it forms the limit of the supersonic region necessary to determine the subsonic field. We shall therefore denote this wave as the "limiting Mach wave." In the hodograph plane, Mach waves that start from the body are represented by epicycloids, such as AD in Fig. 1b. The Mach wave that reaches the sonic line at infinity—that is, the "limiting Mach wave"—is given by AD since point A is the point of the sonic line which maps to infinity in the physical plane. Accordingly, only the part of the supersonic boundary CD is of importance for the determination of the subsonic part of the field, although the expansion may go beyond point D. One might try to follow the continuation of the field downstream of the "limiting Mach wave" in the hodograph plane. Actually, this will not be necessary, since the continuation of the field is purely a supersonic matter, and the computation may be carried out in the physical plane without the aid of the hodograph.

The singularity at point A has been investigated in detail in reference 1. Accordingly, we obtain the following boundary value problem: We seek a solution of Eq. (2) in the shaded part of Fig. 1b which has a given singularity at point A and assumes the value $\psi = 0$ along the boundary ABCD. Along AD no conditions can be prescribed. The type of boundary value problem considered here is closely connected to the one dealt with by Tricomi.[3] Therefore, one sees that the solution of the problem exists and is unique.

In Fig. 2a the hodograph plane is shown in terms of the variables η and θ. In the transonic law of similarity, a limiting process occurs in which the thickness ratio of the body tends to zero. In Fig. 2a the changes of the location of the boundaries that occur in the course of such a limiting process have been counteracted by an enlargement of the scale. As a consequence of this scale transformation, the stagnation point B will, in the limiting case, lie at negative infinity. (For a more detailed representation of this limiting process the reader is referred to reference 1 or 2.)

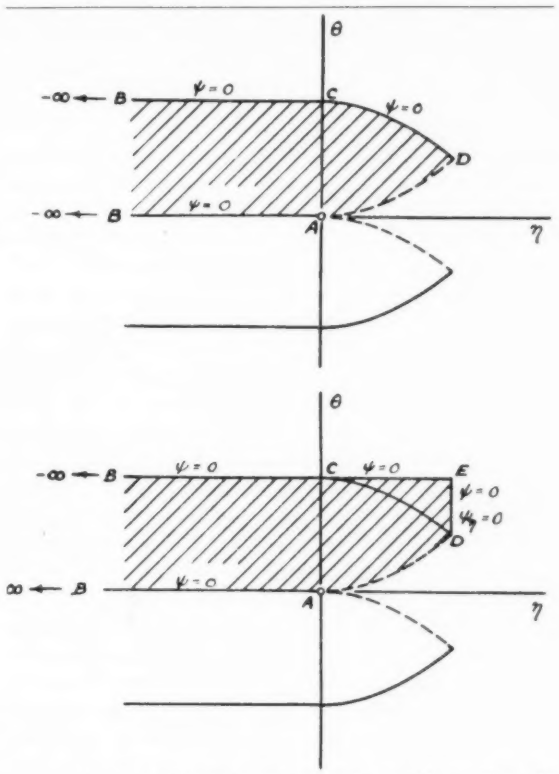

FIG. 2a (*top*). Original boundary value problem. FIG. 2b (*bottom*). Equivalent boundary value problem.

(4) An Equivalent Boundary Value Problem

It will be seen later that it is relatively simple to fulfill the boundary conditions along the lines AB and BC. However, one encounters considerable difficulties if one tries to fulfill the condition along CD. Here, it is useful that the condition along CD can be transformed into conditions prescribed along the line θ = constant which runs through point C—i.e., along CE of Fig. 2b—and along a line η = constant—i.e., along ED. We shall first represent the procedure in a somewhat generalized way.

Let the prescribed condition along the characteristic CD of Fig. 2b be expressed by $\psi = h_1(\theta)$. Now if one imposes the arbitrary condition along the line CE $\psi = h_2(\eta)$, then the flow field in the region DECD will be uniquely determined. It can be computed by means of the method of characteristics. The function ψ and its normal derivative ψ_η along the line DE can especially be found. They may be denoted by $h_3(\theta)$ and $h_4(\theta)$, respectively.

Conversely then, the flow field in the region DECD is uniquely determined if the functions $h_2(\eta)$, $h_3(\theta)$, and $h_4(\theta)$ are given; it can be found again, for example, by means of the method of characteristics. In particular, it will give the function $h_1(\theta)$ along the characteristic CD. Accordingly, if one has a function $\psi(\eta, \theta)$ which fulfills the differential equation, Eq. (2), and which (1) assumes along the subsonic boundary the values required in the original problem, (2) assumes along CE the values $h_2(\eta)$, (3) assumes along DE the value $h_3(\theta)$, and (4) whose normal derivative assumes along DE the values $h_4(\theta)$, then this solution will assume the values of $h_1(\theta)$ along the characteristic CD.

The solution of the boundary value problem modified in the above manner will therefore be the same as the solution of the original boundary value problem.

In the present case, the prescribed boundary condition along the characteristic CD is $\psi = h_1(\theta) = 0$, and the function $h_2(\eta)$ is chosen as zero; therefore, the function ψ will vanish identically in the region DECD. Consequently, the prescribed conditions for ψ and ψ_η along DE will be $\psi = h_3(\theta) = 0$ and $\psi_\eta = h_4(\theta) = 0$, respectively.

(5) The Singularity at Point A

The desired singularity at point A can be expressed by means of the particular solutions obtained by the hypothesis (cf. reference 1)

$$\varphi = |\eta|^{-n} f(\zeta, n) \tag{9}$$

where

$$\zeta = (9/4)\ (\theta^2/\eta^3) \tag{10}$$

and n is a constant.

Inserting this expression into the differential Eq. (3) will yield the following ordinary differential equation for $f(\zeta, n)$:

$$\zeta(\zeta - 1)f'' + \left[\left(\frac{4}{3} - \frac{2}{3}n\right)\zeta - \frac{1}{2}\right]f' + \frac{1}{9}n(n-1)f = 0 \quad (11)$$

Eq. (11) is a hypergeometric equation; the properties of its solution are well known. The considerations for determining the value of the parameter n in the case of the flow with a free-stream Mach Number 1 are carried out in reference 1, and in brief they are as follows:

(1) The "limiting Mach wave" AD must not lie at infinity in the physical plane. Since the gradient of the Legendre potential is proportional to the space vector in the physical plane [cf. Eq. (4)], one obtains the requirement that along the Mach wave AD the functions $f(\zeta, n)$ and $f'(\zeta, n)$ must remain finite. For negative values of n (which are required to produce the singularity at A), this restricts the choice of $f(\zeta, n)$ to one of the linearly independent solutions which is regular at the point $\zeta = 1$. This point corresponds, according to Eq. (7), to the "limiting Mach wave."

(2) Along AB one has the condition $\psi = 0$. Since φ_θ is proportional to ψ according to Eq. (5), one has the condition that the transformed potential is symmetric to the line AB of the hodograph. A solution that fulfills the above condition will, for an arbitrary value of n, in general be represented by a function along the line $\theta = 0$ which consists of a symmetric portion and an antisymmetric portion. Setting the coefficient of the antisymmetric portion equal to zero will yield a condition for n which is fulfilled by an infinite number of discrete values of n.

(3) Among the values of n found above, only those can be used for which the value of ψ tends to infinity at point A and for which the representation in the physical plane is single-valued.

From these considerations the suitable value of n is found to be $n = -1$. Accordingly, the desired singularity is given by

$$\varphi = |\eta|^{-1} f(\zeta, -1) \quad (12)$$

(6) Other Particular Solutions

Another family of particular solutions of Eq. (3) may be found by the hypothesis

$$\varphi = g(\eta, m)\cos(m\pi\theta/\theta_0) \quad (13)$$

where m is a positive integer and θ_0 is an arbitrary angle. Inserting this into the differential Eq. (3) yields the ordinary differential equation for $g(\eta, m)$—namely,

$$g'' + (m\pi/\theta_0)^2 \eta g = 0 \quad (14)$$

The solution of this equation is

$$g = \sqrt{\eta} Z_{1/3}[(2/3)(m\pi/\theta_0)\eta^{3/2}] \quad (15)$$

where $Z_{1/3}$ represents any linear combination of Bessel functions of the order $1/3$.† For negative values of η, this solution is represented by

$$g = \sqrt{|\eta|} Z_{1/3}\left[\left(\frac{2}{3}i\right)\left(\frac{m\pi}{\theta_0}\right)|\eta|^{3/2}\right], \quad \eta < 0 \quad (16)$$

Bessel functions of an imaginary argument have the asymptotic behavior of exponential functions—that is, one linearly independent solution tends to zero for large values of the argument while the other tends to infinity.

Since the stagnation point at the nose of the wedge corresponds to negative infinity in the η, θ-plane, only the solution that tends to zero as the argument tends to negative infinity is permitted, inasmuch as the nose of the wedge must lie in the finite portion of the physical plane. The desired particular solution is, therefore,

$$g = i^{4/3}\sqrt{|\eta|} H^{(1)}_{1/3}\left(\frac{2}{3}\frac{m\pi}{\theta_0} i|\eta|^{3/2}\right), \quad \eta < 0 \quad (17)$$

where $H_{1/3}^{(1)}$ is the Hankel function of the first type of the order $1/3$. The analytical continuation of this solution to positive values of η is given by

$$g = \frac{2}{\sqrt{3}}\sqrt{\eta} \times \left[J_{1/3}\left(\frac{2}{3}\frac{m\pi}{\theta_0}\eta^{3/2}\right) + J_{-1/3}\left(\frac{2}{3}\frac{m\pi}{\theta_0}\eta^{3/2}\right)\right], \quad \eta > 0 \quad (18)$$

where $J_{\pm 1/3}$ are Bessel functions of the order $\pm 1/3$.

The derivatives of these functions are given by

$$\frac{dg}{d\eta} = \frac{m\pi}{\theta_0} i^{5/3}|\eta| H^{(1)}_{2/3}\left(\frac{2}{3}\frac{m\pi}{\theta_0} i|\eta|^{3/2}\right), \quad \eta < 0 \quad (19)$$

and

$$\frac{dg}{d\eta} = \frac{2}{\sqrt{3}}\frac{m\pi}{\theta_0}\eta \times \left[J_{-2/3}\left(\frac{2}{3}\frac{m\pi}{\theta_0}\eta^{3/2}\right) - J_{2/3}\left(\frac{2}{3}\frac{m\pi}{\theta_0}\eta^{3/2}\right)\right], \quad \eta > 0 \quad (20)$$

where $H_{2/3}^{(1)}$ represents Hankel functions of the first type of the order $2/3$ and $J_{\pm 2/3}$ are Bessel functions of the order $\pm 2/3$.

For large values of the argument, the following asymptotic representations are obtained (cf. reference 4):

$$\left.\begin{aligned} g(\eta, m) &\sim \left(\frac{3\theta_0}{m}\right)^{1/2}\frac{|\eta|^{1/4}}{\pi} e^{-(2/3)(m\pi/\theta_0)|\eta|^{3/2}}, \quad \eta < 0 \\ g(\eta, m) &\sim \left(\frac{12\theta_0}{m}\right)^{1/2}\frac{\eta^{-1/4}}{\pi}\cos\left(\frac{2}{3}\frac{m\pi}{\theta_0}\eta^{3/2} - \frac{\pi}{4}\right), \quad \eta > 0 \end{aligned}\right\} \quad (21)$$

For $\eta = 0$, one has

$$g = 3^{-1/6}\frac{2}{(-1/3)!}\left(\frac{m\pi}{\theta_0}\right)^{-1/3}, \quad \eta = 0$$

And, finally, for the derivatives, one obtains

† Cf. reference 4.

$$\left.\begin{aligned} \frac{dg}{d\eta} &= +\left(\frac{3m}{\theta_0}\right)^{1/2} |\eta|^{1/4} e^{-(2/3)(m\pi/\theta_0)|\eta|^{3/2}}, \quad \eta < 0 \\ \frac{dg}{d\eta} &\sim \left(\frac{12m}{\theta_0}\right)^{1/2} \eta^{1/4} \cos\left(\frac{2}{3}\frac{m\pi}{\theta_0}\eta^{3/2} + \frac{\pi}{4}\right), \quad \eta > 0 \end{aligned}\right\} \tag{22}$$

$$\frac{dg}{d\eta} = 3^{1/6}\frac{2}{(-2/3)!}\left(\frac{m\pi}{\theta_0}\right)^{1/3}, \quad \eta = 0$$

From these expressions the following asymptotic formula, which is basic for the method of solution used subsequently, is found:

$$\frac{dg/d\eta}{g} \sim \frac{m\pi}{\theta_0}\eta^{1/2}\tan\left(\frac{2}{3}\frac{m\pi}{\theta_0}\eta^{3/2} - \frac{\pi}{4}\right), \quad \eta > 0 \tag{23}$$

(7) Reformulation of the Boundary Value Problem in Terms of the Legendre Potential

In Sections (3) and (4) the boundary value problem was formulated in terms of the stream function. In this form the boundary value problem conforms to the type considered by Tricomi.[3] From the standpoint of the actual computations, however, the use of the transformed potential is preferable, because of the fact that the coordinates in the physical plane can be obtained from the transformed potential merely by partial differentiations whereas an integration is necessary in the case of the stream function. The correspondence between the two may be obtained from Eq. (5). One merely replaces in the boundary conditions the function ψ by $(1/\rho^*)\varphi_\theta$; then ψ_η is replaced by $(1/\rho^*)\varphi_{\eta\theta}$. Since the latter expression is prescribed only along a line η = constant—i.e., along the line DE of Fig. 2b—one can integrate it with respect to θ and obtain

$$\varphi_\eta = \int \varphi_{\eta\theta} d\theta + \text{const.}$$

Consequently, φ_η is prescribed along DE except for a constant. Since the transformed potential is symmetric with respect to the horizontal axis, the same constant would occur in the lower half of the hodograph. A solution of the hodograph equation that has $\varphi_\theta = 0$ everywhere and for which φ_η = constant along DE is given by

$$\varphi = \text{const.}\ \eta$$

Therefore, the boundary conditions for φ are determined from those for ψ with the exception of a term resulting from a solution given by the last equation. The presence of such a solution would change the x-coordinates by a constant; in other words, it represents a shift of the system of coordinates in the physical plane. Naturally, such a shift is unessential.

Accordingly, the boundary value problem in terms of φ has the following prescribed conditions: $\varphi_\theta = 0$ along ABCE and ED (Fig. 2b) and $\varphi_\eta = 0$ along ED.

(8) Procedure for the Fulfillment of the Boundary Conditions

The computations start with an expression that yields the desired singularity at the point that corrresponds to the free-stream conditions. This expression does not fulfill the boundary conditions. However, since the condition $\varphi_\theta = 0$ along the line BCE can be considered as a condition of symmetry, it may be fulfilled rather easily by an image system. Then, since φ_θ is both continuous and antisymmetric along AB, the condition $\varphi_\theta = 0$ there will be automatically satisfied.

In Eq. (13), if one sets θ_0 equal to half of the angle at the tip of the wedge, then φ_θ formed with these particular solutions will be zero for $\theta = \theta_0$ and $\theta = 0$—that is, along the surface of the body and along the line AB. These solutions can be arbitrarily superimposed without influencing the boundary conditions along BCE and AB and will, therefore, be used to fulfill the boundary conditions along ED.

In the present case, the fulfillment of these conditions will be carried out in two different steps. (1) One forms an expression that fulfills the condition for φ_θ without any regard to the conditions prescribed for φ_η. (2) One adds a solution that does not contribute to the value of φ_θ along ED but fulfills the prescribed conditions for φ_η.

Accordingly, the transformed potential will be obtained as the sum of three portions—that is,

$$\varphi = \varphi_1 + \varphi_2 + \varphi_3 \tag{24}$$

Here φ_1 is the portion that originates from the image system—that is, it arises by a superposition of an infinite number of functions given by Eq. (12). The singularities are located along the θ-axis at the interval of $2\theta_0$.

φ_2 arises by a superposition of the particular solutions given by Eq. (13) such that the condition $\varphi_\theta = 0$ along ED is fulfilled. (φ_2 is not uniquely determined by this requirement as will be seen later.)

φ_3 arises from a superposition of functions given by Eq. (13) such that along ED (or, in other words, $\eta = \eta_0$ and $\theta_0/2 \leq \theta \leq \theta_0$) one has $\varphi_{3_\theta} = 0$ and $\varphi_{1_\eta} + \varphi_{2_\eta} + \varphi_{3_\eta} = 0$. If φ_2 is chosen, then φ_3 will be determined uniquely.

(9) Computation of φ_1

If one differentiates Eq. (12) with respect to θ, then one obtains

$$\varphi_\theta = -3|\eta|^{-5/2}\sqrt{|\zeta|}\,f', \quad \text{sign } \eta\cdot\theta$$

where the symbol sign $\eta\cdot\theta$ denotes that the preceded quantity is to be multiplied by the sign of the product $\eta\cdot\theta$. Accordingly, φ_θ is an odd function with respect to the η-axis. If one now has a series of these singularities located at an interval of $2\theta_0$ along the θ-axis, then along a line θ = constant which lies in the middle be-

tween two singularities—e.g., at $\theta = \theta_0$—the contribution of φ_θ from the singularities in the upper half will be canceled by that from the lower half-plane. In other words, the boundary conditions will be fulfilled. Consequently, φ_1 is given by

$$\varphi_1 = -|\eta|^{-1} \sum_{m=-\infty}^{\infty} f(\zeta_m, -1) \tag{25}$$

where

$$\zeta_m = (9/4)\ [(\theta - 2m\theta_0)^2/\eta^3]$$

The partial derivatives of Eq. (25) with respect to η and θ are

$$\varphi_{1_\eta} = |\eta|^{-2} \sum_{m=-\infty}^{\infty} (3\zeta_m f' + f), \quad \text{sign } \eta \tag{26}$$

and

$$\varphi_{1_\theta} = -3|\eta|^{-5/2} \sum_{m=-\infty}^{\infty} \sqrt{|\zeta_m|}\, f', \quad \text{sign } (\theta - 2m\theta_0)\eta \tag{27}$$

respectively.

Let us check the convergence of these expressions. For large values of the argument, the function $f(\zeta_m, -1)$ is represented by

$$f \sim c_1 \zeta_m^{-1/2} + c_2 \zeta_m^{-2/3}$$

where c_1 and c_2 are constants (see reference 1). Accordingly, the particular solutions (12) for large values of ζ_m are given by

$$\varphi_{1_m} \sim c_1 \left[\frac{2}{3}(\theta - 2m\theta_0)\right]^{2/3} + c_2\eta \left[\frac{2}{3}(\theta - 2m\theta_0)\right]^{-4/3}$$

where φ_{1_m} is the mth term of the series in Eq. (25). Hence, one sees that for large values of ζ_m—i.e., for large values of m—the mth term of the series in Eqs. (26) and (27) will be less than, or equal to, $c'm^{-4/3}$ or $c''m^{-5/3}$, respectively, where c' and c'' are constants independent of m. Consequently, the convergence of the partial derivatives given by Eqs. (26) and (27) will follow.

(10) Computation of φ_2

Let the value of η along the line ED be denoted by η_0. From the equation for the characteristics, Eq. (7), one finds

$$\eta_0 = [(3/4)\theta_0]^{2/3} \tag{28}$$

If one now inserts this expression into the asymptotic formulas given by Eqs. (21) and (22), one finds that for $\eta = \eta_0$ the absolute values of the functions $g(\eta, m)$ and $g'(\eta, m)$ will be larger than a finite constant for all values of m. Therefore, the family of solutions given by Eq. (13) will furnish a complete set of functions $\sin m\pi\theta/\theta_0$ and $\cos m\pi\theta/\theta_0$ in the interval $0 \leq \theta \leq \theta_0$.

If one considers solely the fulfillment of the conditions for φ_θ, then one has at his disposal an entire set of orthogonal functions defined in the interval $0 \leq \theta \leq \theta_0$. However, the condition for φ_2 along ED expressed by the requirement that $\varphi_{1_\theta} + \varphi_{2_\theta} = 0$ is given in the interval $\theta_0/2 \leq \theta \leq \theta_0$ only. Obviously, one can choose the continuation of φ_{1_θ} arbitrarily in the interval from $\theta = 0$ to $\theta = \theta_0/2$; then the determination of φ_2 will be unique. The arbitrary element introduced in this way will vanish if one determines φ_3. For our computations, we choose φ_{2_θ} in the interval $0 \leq \theta \leq \theta_0/2$ symmetric with respect to the line $\theta = \theta_0/2$ with the values in the interval $\theta_0/2 \leq \theta \leq \theta_0$.

The actual computation is carried out in the following manner: One first finds the values of φ_{1_θ} for $\eta = \eta_0$ and $\theta_0/2 \leq \theta \leq \theta_0$, and then continues the curve into the interval $0 \leq \theta \leq \theta_0/2$ as described above. This function is then represented as the Fourier sine series

$$\varphi_{1_\theta} = -3\left(\frac{3}{4}\theta_0\right)^{-5/3} \sum_{m=0}^{\infty} B_{2m+1} \sin \frac{(2m+1)\pi\theta}{\theta_0} \tag{29}$$

where B_{2m+1} are constants determined by the Fourier analysis. Next, φ_2 is written in a corresponding form

$$\varphi_2 = \sum_{m=0}^{\infty} A_{2m+1} \frac{g(\eta, 2m+1)}{g(\eta_0, 2m+1)} \cos \frac{(2m+1)\pi\theta}{\theta_0} \tag{30}$$

Here, the coefficients A_{2m+1} must be determined from the condition that $\varphi_{1_\theta} + \varphi_{2_\theta} = 0$. If one now differentiates Eq. (30) with respect to θ and equates the resulting expression to Eq. (29), one finds the coefficients A_{2m+1} as

$$A_{2m+1} = -3\left(\frac{3}{4}\theta_0\right)^{-5/3} \frac{\theta_0}{\pi} \frac{B_{2m+1}}{2m+1}$$

Accordingly, the partial derivatives φ_{2_θ} and φ_{2_η} will be

$$\varphi_{2_\theta} = 3\left(\frac{3}{4}\theta_0\right)^{-5/3} \sum_{m=0}^{\infty} B_{2m+1} \frac{g(\eta, 2m+1)}{g(\eta_0, 2m+1)} \times \sin \frac{(2m+1)\pi\theta}{\theta_0} \tag{31}$$

and

$$\varphi_{2_\eta} = -3\left(\frac{3}{4}\theta_0\right)^{-5/3} \frac{\theta_0}{\pi} \sum_{m=0}^{\infty} \frac{B_{2m+1}}{2m+1} \times \frac{g'(\eta, 2m+1)}{g(\eta_0, 2m+1)} \cos \frac{(2m+1)\pi\theta}{\theta_0} \tag{32}$$

Since, according to the asymptotic representations Eqs. (21) and (22), the order of magnitude of the functions $g(\eta, m)$ (as well as for the functions g') is always the same for all values of $\eta > 0$ with the exception of the universal factor $\eta^{-1/4}$, the convergence of the function φ_{2_θ} (as well as for φ_{2_η}) is assured if the corresponding series converge at $\eta = \eta_0$. Since the latter series are Fourier expansions of closed functions, the expression for φ_{2_θ} and φ_{2_η}, Eqs. (31) and (32), will converge for all positive values of η. For negative values of η, the convergence is assured because of the presence of the exponential function [cf. Eqs. (21) and (22)]. The fac-

tor $\eta^{-1/4}$ occurring in this consideration seems to indicate a difficulty at the sonic velocity—i.e., for $\eta = 0$. Here, the functions g and g' can be determined directly and are given in Eqs. (21) and (22). One finds that the mth term in the expression for φ_{2_θ} at $\eta = 0$ is comparable to the mth term at $\eta = \eta_0$ except for a factor $m^{1/6}$, whereas at the mth term for φ_{2_η} a factor $m^{-1/6}$ must be added to the corresponding term at $\eta = \eta_0$. Accordingly, the convergence of φ_{2_η} for $\eta = 0$ is somewhat better than for $\eta = \eta_0$ and that for φ_{2_θ} is decreased as compared to the expression at $\eta = \eta_0$. However, since even the Fourier representation of the function $\varphi_{\theta\theta}$ at $\eta = \eta_0$ would converge, the latter factor will be harmless.

(11) Calculation of φ_3

The superposition of the functions φ_1 and φ_2 yields an expression that has the desired singularity and which satisfies the condition that φ_θ is zero along the boundary ABED. In this regard the boundary conditions are fulfilled. However, the condition $\varphi_\eta = 0$ required along DE has not yet been considered. Therefore, a particular solution φ_3 will be added to the previous ones which has $\varphi_{3_\theta} = 0$ along the boundaries ABE and ED and assumes along ED such a value of φ_{3_η} that $\varphi_{1_\eta} + \varphi_{2_\eta} + \varphi_{3_\eta} = 0$. The determination of such a function will, in general, lead to an infinite system of equations. We shall present here a method based on the asymptotic representations of the particular solutions which provides a simpler method of attack. The function φ_3 is represented by a superposition of particular solutions given by Eq. (13)—that is,

$$\varphi_3 = -\frac{\theta_0}{\pi} \sum_{m=1}^{\infty} \frac{b_m}{m} \frac{g(\eta, m)}{g(\eta_0, m)} \cos \frac{m\pi\theta}{\theta_0} \tag{33}$$

where b_m are constants. The conditions along BCE will then be automatically fulfilled. Along ED, one obtains the conditions

$$\left.\begin{aligned} \varphi_{3_\theta} &= 0 \\ \varphi_{3_\eta} &= -(\varphi_{1_\eta} + \varphi_{2_\eta}) \equiv F(\theta) \end{aligned}\right\} \quad \begin{aligned} &\eta = \eta_0 \\ &\theta_0/2 \le \theta \le \theta_0 \end{aligned}$$

where $F(\theta)$ has been determined previously so that it can be considered as a known function. If one inserts Eq. (33) into the above boundary conditions, one obtains

$$\left.\begin{aligned} &\sum_{m=1}^{\infty} b_m \sin (m\pi\theta/\theta_0) = 0 \\ &-\frac{\theta_0}{\pi} \sum_{m=1}^{\infty} \frac{b_m}{m} \left[\frac{g'(\eta, m)}{g(\eta, m)}\right]_{\eta=\eta_0} \cos \frac{m\pi\theta}{\theta_0} = F(\theta) \end{aligned}\right\} \quad (\theta_0/2 \le \theta \le \theta_0) \tag{34}$$

If, in the second equation of Eqs. (34), the asymptotic expression for g'/g for $\eta = \eta_0$ is inserted from Eq. (23), then it is simplified to

$$-\left(\frac{3}{4}\theta_0\right)^{1/3} \sum_{m=1}^{\infty} (-1)^m b_m \cos \frac{m\pi\theta}{\theta_0} = F(\theta) \qquad (\theta_0/2 \le \theta \le \theta_0) \tag{35}$$

The error, due to the use of the asymptotic formula, is 3.9 per cent for $m = 1$ and decreases as m becomes larger. The first condition of Eqs. (34) can be fulfilled in the following way: The function φ_{3_θ} is zero in the interval $\theta_0/2 \le \theta \le \theta_0$, while in the interval $0 \le \theta \le \theta_0/2$ it will, in general, be different from zero. Let the value of φ_{3_θ} in the latter interval be denoted by $p(\theta)$. Then the coefficients b_m are expressed by means of a Fourier analysis of the function φ_{3_θ}—i.e., one obtains

$$b_m = \frac{2}{\theta_0} \int_0^{\theta_0/2} p(u) \sin \frac{m\pi u}{\theta_0} \, du \tag{36}$$

where u is a variable of integration. If the coefficients are determined according to the last equation, the first condition in Eqs. (34) will be fulfilled for any choice of the function $p(u)$. If one inserts the expression for b_m as given by the above equation into Eq. (35), then one obtains

$$-\frac{2}{\theta_0}\left(\frac{3}{4}\theta_0\right)^{1/3} \sum_{m=1}^{\infty} (-1)^m \int^{\theta_0/2} p(u) \times \sin \frac{m\pi u}{\theta_0} \, du \cos \frac{m\pi\theta}{\theta_0} = F(\theta), \quad \frac{\theta_0}{2} \le \theta \le \theta_0 \tag{37}$$

This is an integral equation for the function $p(u)$. The previous problem of finding the coefficients b_m has been transformed into that of finding the function $p(u)$. It should be noted that in the above equations the range of θ is between $\theta_0/2 \le \theta \le \theta_0$, while u varies from 0 to $\theta_0/2$. In order to have the same interval of the variables, one introduces the following transformation:

$$v = \theta_0 - \theta$$
$$F(\theta) = F_1(V)$$

Eq. (36) with the above transformation becomes

$$-\frac{3}{2}\left(\frac{3}{4}\theta_0\right)^{-2/3} \sum_{m=1}^{\infty} \int^{\theta_0/2} p(u) \times \sin \frac{m\pi u}{\theta_0} \, du \cos \frac{m\pi v}{\theta_0} = F_1(V) \tag{38}$$

where $0 \le u \le \theta_0/2$ and $0 \le v \le \theta_0/2$.

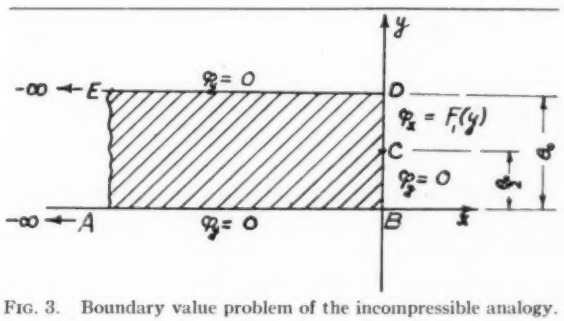

FIG. 3. Boundary value problem of the incompressible analogy.

In the incompressible flow theory, there exists a problem that yields exactly the same equation as the present problem—namely, Eq. (38). A discussion of this incompressible example will be instructive for the subsequent analysis.

Consider a boundary as given in Fig. 3 where the horizontal axis is denoted by x and the vertical axis by y. The differential equation to be fulfilled in the shaded region of Fig. 3 may be that for the incompressible fluid—namely, the Laplace equation—

$$\varphi_{xx} + \varphi_{yy} = 0$$

The boundary conditions prescribed are that $\varphi_y = 0$ along ABC and along DE, and φ_x is a given function $F_1(y)$ along CD. If one replaces φ_y by a new function ϕ and maps the region ABCDE onto a half-plane, the above boundary value problem can be interpreted as that for finding the lift distribution over a thin airfoil.

A harmonic function that fulfills the boundary conditions along AB and DE is given by

$$\varphi(x, y) = -\left(\frac{3}{4}\theta_0\right)^{1/3} \sum_{m=1}^{\infty} \frac{b_m}{m} e^{m\pi x/\theta_0} \cos\frac{m\pi y}{\theta_0}$$

where the b_m's are constants. Since the function φ_y is zero along BC and will assume some value $p(y)$ (unknown as yet) along CD, the coefficients b_m above can then be determined by means of a Fourier analysis; the result is

$$b_m = \frac{2}{\theta_0}\int_0^{\theta_0/2} p(y') \sin\frac{m\pi y'}{\theta_0}\, dy'$$

where y' is a variable of integration.

If one now expresses the condition given for φ_x along CD, one obtains

$$-\frac{3}{2}\left(\frac{3}{4}\theta_0\right)^{-2/3} \sum_{m=1}^{\infty} \int_0^{\theta_0/2} p(y') \sin\frac{m\pi y'}{\theta_0} \times dy' \cos\frac{m\pi y}{\theta_0} = F_1(y),\ 0 \le y \le \theta_0/2 \quad (39)$$

This is exactly the same equation as the one found previously for the main problem—that is, Eq. (38). [To be exact, the variables u and v of Eq. (38) must be replaced by y' and y, respectively.]

The Solution of the Incompressible Analogy

As mentioned above, it is clear that the solution of the incompressible problem can be found by a suitable mapping process. By means of this method one will finally obtain $p(y')$ expressed in terms of $F_1(y)$. We shall give here a method of derivation of the result which is not rigorous from a strictly mathematical point of view; however, it gives the desired expression for $p(y')$ directly in a convenient way. A more rigorous derivation of the result can be obtained either by following the mapping process or by using other properties of the incompressible flow theory.

Eq. (39) will first be rewritten with the order of the integral and the summation signs interchanged—that is,

$$-\frac{3}{2}\left(\frac{3}{4}\theta_0\right)^{-2/3} \int_0^{\theta_0/2} p(y') \sum_{m=1}^{\infty} \sin\frac{m\pi y'}{\theta_0} \times \cos\frac{m\pi y}{\theta_0}\, dy' = F_1(y) \quad (39a)$$

One now introduces in this equation the closed expression given by

$$\sum_{m=1}^{\infty} \sin\frac{m\pi y'}{\theta_0} \cos\frac{m\pi y}{\theta_0} = \frac{(1/2)\sin(\pi y'/\theta_0)}{\cos(\pi y/\theta_0) - \cos(\pi y'/\theta_0)} \quad (40)$$

(The use of this correspondence in the integral equation can be justified by carrying out the mapping process mentioned above.) Eq. (39a) with the use of Eq. (40) becomes

$$-\frac{3}{4}\left(\frac{3}{4}\theta_0\right)^{-2/3} \int_0^{\theta_0/2} p(y') \times \frac{\sin(\pi y'/\theta_0)dy'}{\cos(\pi y/\theta_0) - \cos(\pi y'/\theta_0)} = F_1(y),\ 0 \le y \le \theta_0/2 \quad (41)$$

The singular kernel of this equation offers no essential difficulties, being similar in nature to that in the downwash integral of incompressible theory.

The integral Eq. (41) will now be re-expressed in terms of the new variables r and s defined by the equations

$$\left.\begin{aligned} \cos\frac{\pi y'}{\theta_0} &= \frac{1}{2}(1 + \cos t), \quad p(y') = p_1(t) \\ \cos\frac{\pi y}{\theta_0} &= \frac{1}{2}(1 + \cos s), \quad F_1(y) = F_2(s) \end{aligned}\right\} \quad (42)$$

The integral equation in terms of these new variables is

$$-\frac{1}{\pi}\left(\frac{3}{4}\theta_0\right)^{1/3} \int_0^{\pi} p_1(t) \frac{\sin t\, dt}{\cos s - \cos t} = F_2(s) \quad (0 \le s \le \pi) \quad (43)$$

In order to solve this integral equation, one first introduces the correspondence in Eq. (40) (expressed in terms of s and t instead of y and y') into Eq. (43); the result is

$$-\frac{2}{\pi}\left(\frac{3}{4}\theta_0\right)^{1/3} \int_0^{\pi} p_1(t) \sum_{m=1}^{\infty} \sin mt \cos ms\, dt = F_2(s) \quad (0 \le s \le \pi) \quad (44)$$

In this form the solution is rather obvious. First, one expresses $F_2(s)$ in terms of a Fourier cosine series in s—that is,

$$F_2(s) = \sum_{m=0}^{\infty} d_m \cos ms$$

where

$$d_m = (2/\pi)\int_0^{\pi} F_2(s') \cos ms'\, ds' \quad (45)$$

Here, s' is a variable of integration.

It was mentioned in Section (7) that the expression φ_η can be changed by a constant without an essential effect upon the flow in the physical plane. If the given values of φ_η are changed by a constant, then $F_2(s)$ will also be changed by a constant amount. Accordingly, the constant in the expression for $F_2(s)$ may be disregarded.

One now makes the hypothesis

$$p_1(t) = \sum_{m=1}^{\infty} C_m \sin mt \tag{46}$$

Inserting Eqs. (45) and (46) in Eq. (44) and using the orthogonality relationship for the sines, one obtains a relation between the unknown coefficients C_m and the known coefficients d_m. One simply has $C_m = d_m$ With this result the function $p_1(t)$ can be expressed in the form

$$p_1(t) = \frac{2}{\pi} \sum_{m=1}^{\infty} \int_0^{\pi} F_2(s') \cos ms' \, ds' \sin mt \tag{47}$$

or expressed in the closed form

$$p_1(t) = \frac{\sin t}{\pi} \int_0^{\pi} F_2(s') \frac{ds'}{\cos s' - \cos t} \tag{48}$$

where the correspondence in Eq. (40) has been used.

Eq. (47) represents the solution of Eq. (39). In these equations no serious difficulties of convergence will occur. Eq. (47) has been found by means of the incompressible flow. However, it must be emphasized that the validity of Eq. (47) is naturally independent of the manner in which it has been obtained; it can be used without reference to a specific example. One might question the uniqueness of the solution. In the case of the incompressible analogy and in the case of our example, the uniqueness is obvious from general uniqueness theorems concerning the flow problems (in the case of the transonic flow from Tricomi's uniqueness theorem[3]).

Application of the Incompressible Analogy to the Present Problem

The results of the previous paragraph can now be applied to the main problem. It was seen previously that the equation in this case [Eq. (38)] was identical to the above incompressible analogy if the variables y and y' are replaced by v and u, respectively. Accordingly, Eqs. (47) and (48) may be applied directly to the present problem, provided in the transformation Eq. (42) the variables v and u are inserted in the place of y and y', respectively.

Consequently, Eqs. (33) and (36), together with either of the above results, comprise the final results for φ_3. In the actual computation, however, the function $p_1(t)$ in the form of Eq. (47) was used. The convergence of the function φ_3 and its partial derivatives with respect to η and θ can be investigated by following

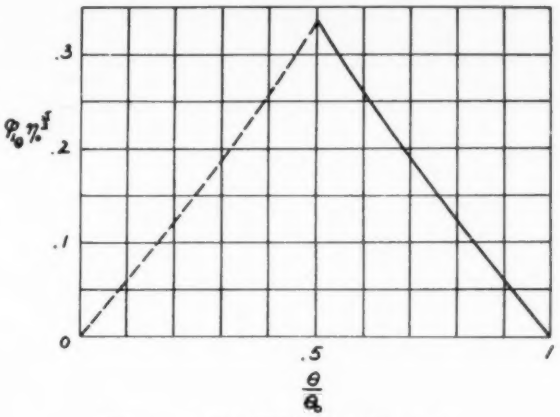

FIG. 4. φ_{1_θ} as a function of θ for $\eta = \eta_0$.

the influence of the different transformations. It can be shown that φ_3 and its derivatives will converge.

(12) DETAILS OF THE COMPUTATIONS

The starting point of the computations is the evaluation of φ_{1_θ} along the line DE—that is, for $\eta = \eta_0$ and $\theta_0/2 \leq \theta \leq \theta_0$. Here, the formulas for the determination of the function $f(\zeta_m, -1)$ and its derivatives are given in reference 1. In some cases more accurate values were determined by means of series representations of these functions. The resulting values of φ_{1_θ} are shown in Fig. 4.

In order to determine φ_2, this curve was continued symmetrically with respect to the line $\theta = \theta_0/2$ (dashed line of Fig. 4). From this curve, the Fourier coefficients B_{2m+1} are found by means of a harmonic analyzer; they are listed in Table 1.

In order to determine φ_3, one first forms the expression $F(\theta) = -(\varphi_{1_\eta} + \varphi_{2_\eta})$ by means of Eqs. (26) and (32). In $F(\theta)$ the transformation from the variable θ, which is essentially the variable v, is now made to the variable s. The relation between v and s (as well as between u and t) is given by Eq. (42), in which y and y' are replaced by v and u, and is shown in Fig. 5. A Fourier analysis is now carried out for the function $F_2(s)$ (cf. Fig. 6), and the coefficients d_m of Eq. (45) are computed. From this result the expression $p_1(t)$ as given by Eq. (46) may be found, since $C_m = d_m$. Because of the singularity that occurs in the relation between $v = \theta_0 - \theta$ and s for $v = \theta_0/2$, the function $p(\theta)$ will have a vertical tangent at $\theta = \theta_0/2$. One now finds the coefficients b_m for Eq. (33) by a Fourier analysis of the

TABLE 1

Values of B_{2m+1} for Eqs. (31) and (32)

m	B_{2m+1}	m	B_{2m+1}
0	−0.0875	5	0.0011
1	0.0124	6	−0.00059
2	−0.0042	7	0.0050
3	0.0023	8	−0.00049
4	−0.0012		

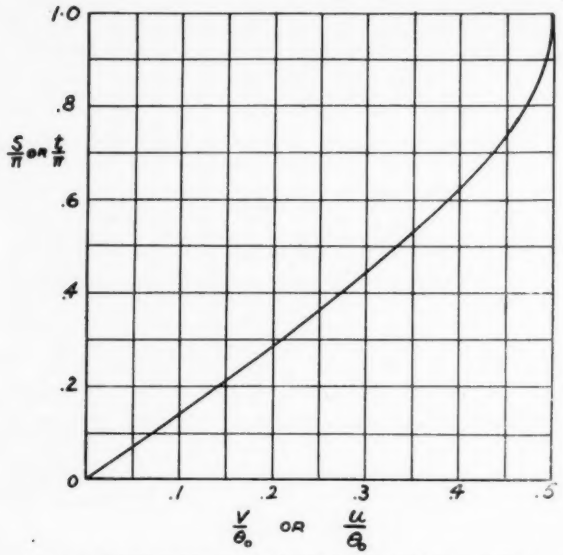

FIG. 5. Transformation of the variables v and u to s and t.

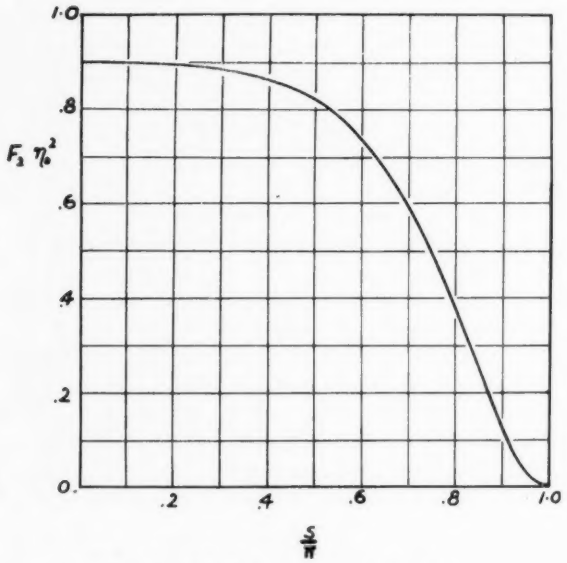

FIG. 6. $F_2(s)$ for $\eta = \eta_0$ and $0 \leq s \leq \pi$.

function that is equal to $p(\theta)$ for $0 \leq \theta \leq \theta_0/2$ and equal to zero in the interval $\theta_0/2 \leq \theta \leq \theta_0$. The coefficients are given in Table 2. The vertical tangent mentioned above for the function $p(\theta)$ at $\theta = \theta_0/2$ will cause this series to converge more slowly.

As a check for the solution φ_3, the fulfillment of the original boundary condition that $\varphi_\theta = 0$ along the characteristic CD will be verified. Fig. 7 shows the values of φ_{1_θ}, $\varphi_{1_\theta} + \varphi_{2_\theta}$, and $\varphi_{1_\theta} + \varphi_{2_\theta} + \varphi_{3_\theta}$ as functions of θ along the characteristic CD. It can be seen that this boundary condition is satisfactorily fulfilled.

The next step of the computations represents the transformation of the results back to the physical

TABLE 2
Values of b_m for Eq. (33)

m	$b_m \left(\frac{3}{4}\theta_0\right)^{2/3}$	m	$b_m \left(\frac{3}{4}\theta_0\right)^{2/3}$
1	0.01796	11	0.00069
2	0.01346	12	−0.00251
3	−0.00354	13	−0.00072
4	−0.00858	14	0.00200
5	0.00061	15	0.00069
6	0.00569	16	−0.00164
7	0.00034	17	−0.00052
8	−0.00412	18	0.00144
9	−0.00041	19	0.00050
10	0.00320	20	0.00118

plane. It is carried out by means of Eqs. (4). We shall restrict ourselves to the determination of the coordinates of the profile and the corresponding pressure distribution. The x-coordinates as a function of η are found according to Eqs. (4) with $\theta = \theta_0$. The pressure coefficient is then found as a function of η by means of Eq. (6). The resulting pressure distribution is shown in Fig. 8.

In the original simplifications of the basic equations by means of the transonic law of similarity, it was assumed that the entire velocity field was in the neighborhood of the critical velocity. The stagnation region at the nose of the profile will, therefore, be out of the range of validity of the present theory, just as in the case of the Prandtl-Glauert approximations. However, Fig. 8 shows that this region is indeed small for conventional thickness ratios of the profile.

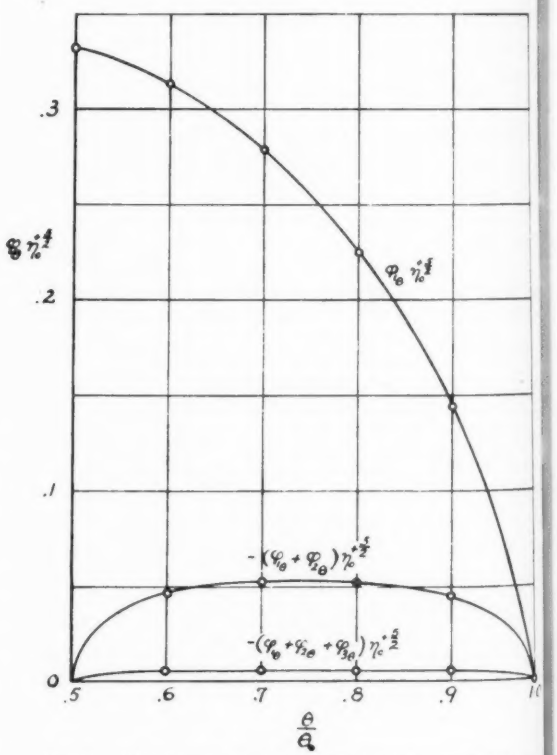

FIG. 7. Distribution of φ_θ along the characteristic CD.

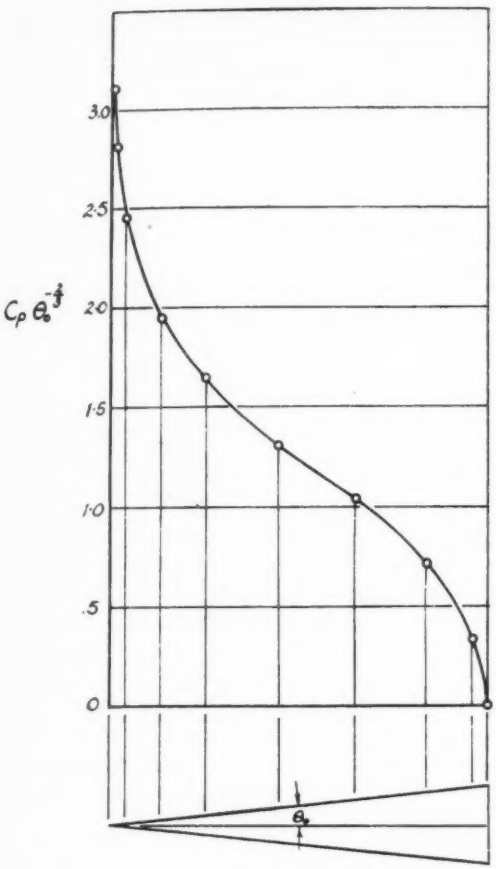

FIG. 8. Pressure distribution over the nose.

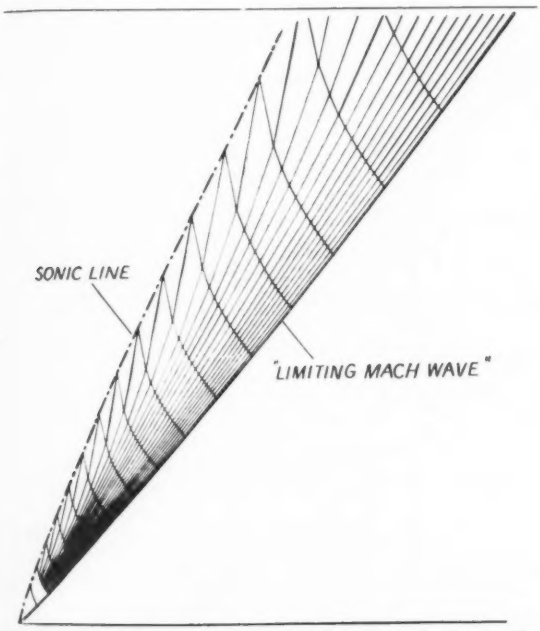

FIG. 9. Construction of the flow from the sonic line to the "limiting Mach wave." (The free-stream direction is from left to right.)

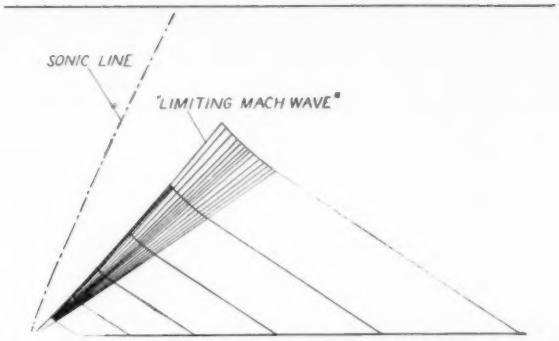

FIG. 10. Construction of the rear part of minimum drag. (The free-stream direction is from left to right.)

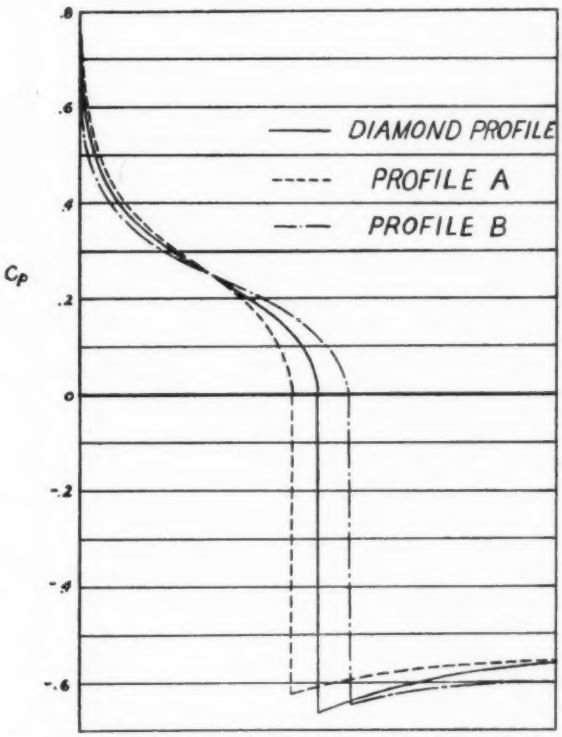

FIG. 11. Pressure distribution for the profiles of Fig. 12 with different positions of the maximum thickness.

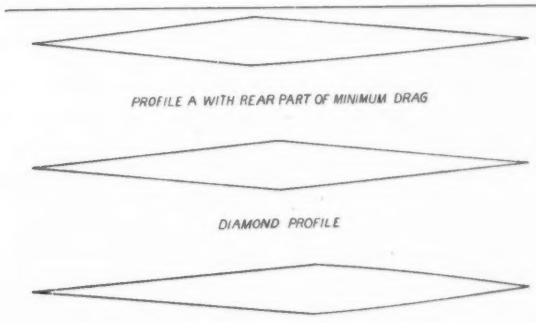

FIG. 12. Profiles for the pressure distributions of Fig. 11.

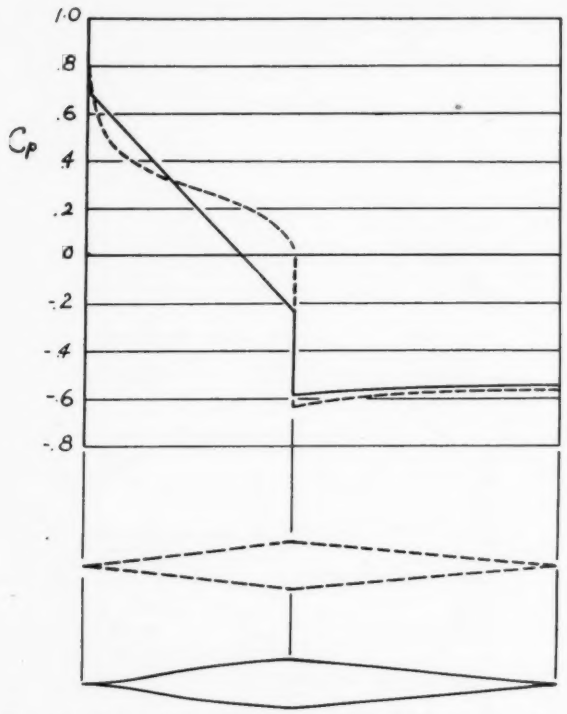

FIG. 13. Comparison of the pressure distributions over wedge and cusped nose profiles of 10 per cent thickness.

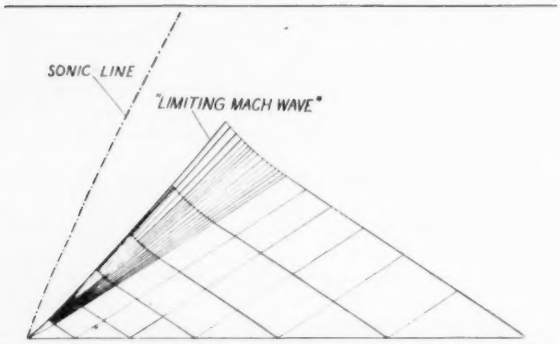

FIG. 14. Construction of the straight-sided rear part. (The free-stream direction is from left to right.)

The position of the sonic line is then computed, and the flow downstream to the "limiting Mach wave" [cf. Section (3)] is constructed by means of the method of characteristics. The result is shown in Fig. 9.

The flow downstream of the "limiting Mach wave" is arbitrary and can be constructed by the method of characteristics if the continuation of the zero stream line is prescribed. First, we shall assume that the rear portion of the body is such that it gives a minimum contribution to the drag at a given length of the profile. In reference 1, it was shown that this optimum condition is fulfilled if one first allows a Meyer expansion and then forms the rear part of the profile such that the compression waves coming from the sonic line are not reflected at the body. The length of the rear portion of the profile is determined by the amount of the Meyer expansion allowed at the corner. The contour of the body downstream of the corner is then found by integrating the slope of the stream lines for $y = 0$. The construction of the flow for a profile with a rear part of minimum drag is shown in Fig. 10. In Fig. 11 is shown the pressure distributions for profiles obtained by using different amounts of expansions at the corner; here, the different profiles are reduced to the same thickness ratio by means of the transonic law of similarity. By this process one obtains a family of profiles in which the position of maximum thickness varies. The profiles corresponding to the pressure distribution of Fig. 11 are shown in Fig. 12.

In Fig. 13, a comparison is shown between the pressure distribution over a wedge-nosed profile with that over a profile with a cusped nose as determined in reference 1; the rear parts in each case are those for minimum drag conditions.

The second type of rear portion is chosen so as to obtain the standard diamond profile with the maximum thickness located at the mid-chord. The construction of the flow in this case is shown in Fig. 14, and the corresponding pressure distribution is given in Fig. 11. It has been shown[1] that at a corner such as that occurring at the mid-chord of the diamond profile, a shock wave must arise; the shock in this case is formed by the compression waves coming from the sonic line which coalesce after being reflected from the side of the profile. In the present case, this shock was so weak that the mesh interval used for the construction was too coarse to show its presence.

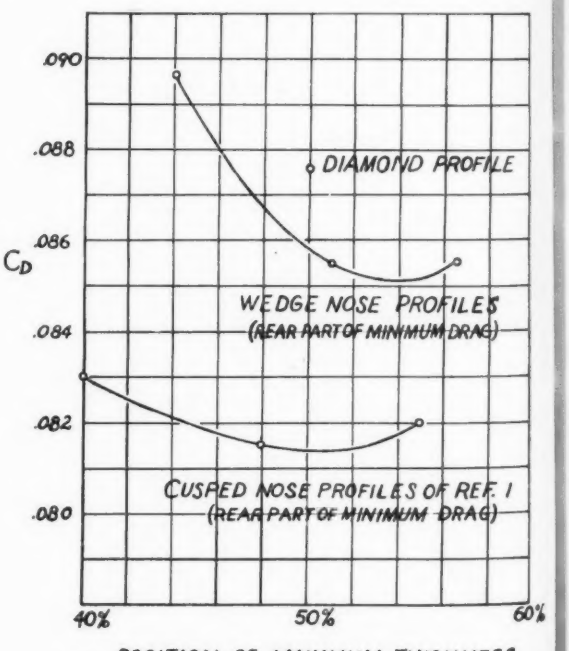

FIG. 15. Variation of C_D with the position of maximum thickness (thickness ratio 10 per cent).

Finally, in Fig. 15 the drag coefficients for the wedge-shaped nose with rear parts of minimum drag are given as a function of the position of maximum thickness. Also shown are the values for the diamond shape profile and for the bodies of reference 1. It should be noticed that the drags for the profiles with the cusped nose are lower than those with a wedge nose. According to physical plausibility, the cusp at the nose must be considered as unfavorable. Naturally, the contribution to the drag that is caused by the tip of the profile in such a case is rather small; therefore, if the tip portion of the cusped profile is omitted, the body as a whole for a given length of the profile will appear to be blunter than a body with the same thickness ratio but without a cusp at the nose. In this respect the above results are astonishing. On the other hand, one sees from Fig. 13 that along the subsonic side of the profile the expansion is much more rapid in the case of the profile with the cusped nose than in the case of the wedge-nose profile. In the former case one has even a suction on the portion of the profile upstream of the maximum thickness.

(13) Final Remarks

In the present paper, the flow over a wedge-shaped profile at Mach Number 1 has been computed. The direct procedure for satisfying the boundary conditions for this flow in the hodograph plane leads to an infinite system of linear equations. By reformulating the supersonic portion of the boundary value problem, it was shown that one could avoid solving this infinite system directly and reduce the problem to that of finding suitable Fourier expansions of the boundary conditions.

The final results indicate that one may expect a reasonable value (as compared to the values that are usually predicted) of the drag coefficient at Mach Number 1. The present results are based upon the assumption that the flow is potential, so that the resulting drag coefficients must be considered only as an optimum result.

References

[1] Guderley, Gottfried, *Singularities at the Sonic Velocity*, U.S. Air Force Report, F-TR-1171-ND, June 1948.

[2] Guderley, Gottfried, *Considerations on the Structure of Mixed Subsonic-Supersonic Flow Patterns*, U.S. Air Force Report, F-TR-2168-ND, October, 1947.

[3] Tricomi, F., *On Linear Partial Differential Equations of the Second Order of Mixed Type*, Brown University Translation, A9-T-26 (to be printed as a Central Air Documents Office translation in the near future). (Original source: Atti della R. Accademia Nazionale dei Lincei 1923. Serie Quinta, Memorie della Classe di Scienze Fisiche, Matematiche e Naturali. Vol. XIV, p. 134.)

[4] Jahnke, E., and Emde, F., *Tables of Functions*, Dover Publications, New York, 1945.

A System for the Excitation of Pure Natural Modes of Complex Structure

(*Continued from page 722*)

[4] Rayleigh, J. W. S. Baron, *The Theory of Sound*, Vol. 1, 2nd Ed., Macmillan and Company, Ltd., London, 1926.

[5] Kennedy, C. C., and Pancu, C. D. P., *Use of Vectors in Vibration Measurement and Analysis*, Journal of the Aeronautical Sciences, Vol. 14, No. 11, p. 603, November, 1947.

[6] Lewis, R. C., and Wrisley, D. L., *Report on Excitation of Pure Natural Modes of Complex Structures (Phase A—Experimental Development)*. M.I.T. Aero-Elastic and Structures Research.

[7] Lewis, R. C., and Wrisley, D. L., *Report on Excitation of Pure Natural Modes of Complex Structures (Phase B—Test Equipment—Operating and Maintenance Instructions)*. M.I.T. Aero-Elastic and Structures Research.

Effect of Torsional Stiffness Requirements on Wing Structural Weight

W. R. MICKS*
The RAND Corporation

SUMMARY

Curves are obtained which show the total increase in weight of an optimum-designed sheet-stiffener compression panel when the skin thickness is increased by an arbitrary amount. These example curves are based on data from tests conducted by the N.A.C.A. on 75S-T Y-stiffened panels. However, the method outlined may also be applied to the plotting of other sheet-stiffener compression panel data.

The N.A.C.A. data, when put in the form outlined here, indicate the minimum amount by which the total weight of sheet and stiffeners would be increased in order to achieve a given increase in sheet thickness. If optimum design principles are followed, this increase in total weight is considerably less than the increase that would result if the amount of stiffener material were left unchanged.

The method outlined here for presenting data is of particular use in preliminary design work where the effects of aeroelasticity requirements must be evaluated in terms of increased wing weight.

INTRODUCTION

ONE OF THE PROBLEMS encountered in the structural design of the wing for high-speed airplanes is that of providing sufficient structure to prevent aeroelastic effects, such as loss in aileron effectiveness, from exceeding acceptable limits. Most of the aeroelastic effects experienced by the unswept wing are due to a reduction in effective torsional stiffness which accompanies an increase in flight speed. For a wing having the flexural axis located aft of the line of aerodynamic centers, there is not a great deal that can be done to prevent this apparent loss in stiffness. What the designer usually does is provide sufficient structural stiffness so that at the speed in question the wing retains sufficient effective stiffness to keep the aeroelastic effects within specified limits.

One method of increasing torsional stiffness, without redesigning the entire wing structure, is to increase the skin thickness of the structural box. Assuming that the shear flow is constant around the structural box, the expression for the section torsional stiffness, GJ (in.lbs. per rad. per in.), is

$$GJ = 4A_e^2G/\int ds/t_s \qquad (1)$$

where

A_e = enclosed area of the structural box
G = modulus of elasticity in shear
s = distance around the perimeter of the box
t_s = skin thickness

Writing the denominator in series form,

$$GJ = \frac{4A_e^2G}{\frac{s_1}{t_{s_1}} + \frac{s_2}{t_{s_2}} + \frac{s_3}{t_{s_3}} + \ldots + \frac{s_n}{t_{s_n}}} \qquad (2)$$

It can be seen from Eq. (2) that, since the terms in the denominator are divided by skin thickness, the most efficient† way to increase the torsional stiffness at any spanwise station is to make the skin thickness uniform around the box. After this has been done, the section torsional stiffness may be determined from the expression

$$GJ = 4A_e^2Gt_s/s \qquad (3)$$

where

t_s = skin thickness (assumed to be uniform around the structural box)
s = perimeter of the structural box

Eq. (3) shows that, for a uniform skin thickness around the box, the torsional stiffness varies directly with the skin thickness; hence, any further increase in stiffness is most efficiently obtained by a uniform increase in skin thickness.

At this point it is desirable to know how the weight of a sheet-stiffener compression panel is affected by an increase in skin thickness, the loading remaining unchanged. It is incorrect to assume that an increase in torsional stiffness would require an increase in skin thickness without any decrease in the amount of stiffener material. Actually, as the skin thickness is increased, the amount of stiffener material may be decreased, since the axial loading to be carried remains constant. This, of course, can be done only in the earlier stages of design.

By using data from tests made by the N.A.C.A., it is possible to obtain curves showing the total increase in weight caused by increasing the skin thickness by an arbitrary amount.

METHOD OF OBTAINING CURVES

The data on which the curves of this report are based were obtained from Fig. 20 of N.A.C.A. Technical

Received March 14, 1950.
*Engineer.

† "Efficient" is used here in the sense of obtaining the maximum increase in stiffness for the amount of weight added.

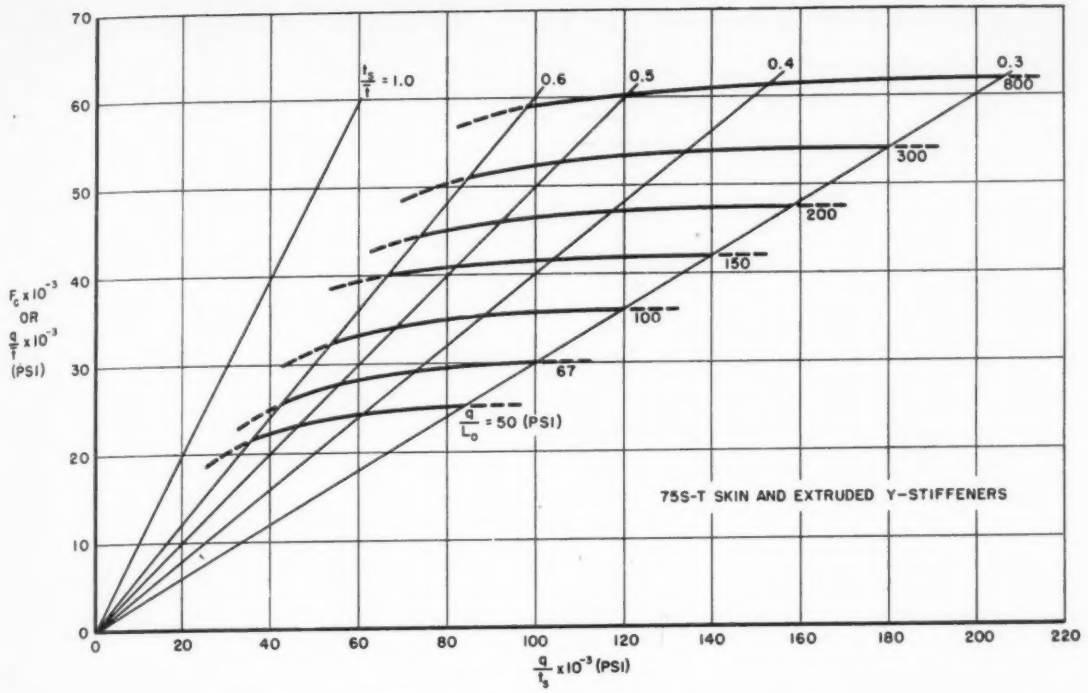

FIG. 1 — MAXIMUM ALLOWABLE STRESS FOR 75S-T SHEET-STIFFENER PANELS FOR DIFFERENT VALUES OF $\frac{q}{t_s}$ AND STRUCTURAL INDEX

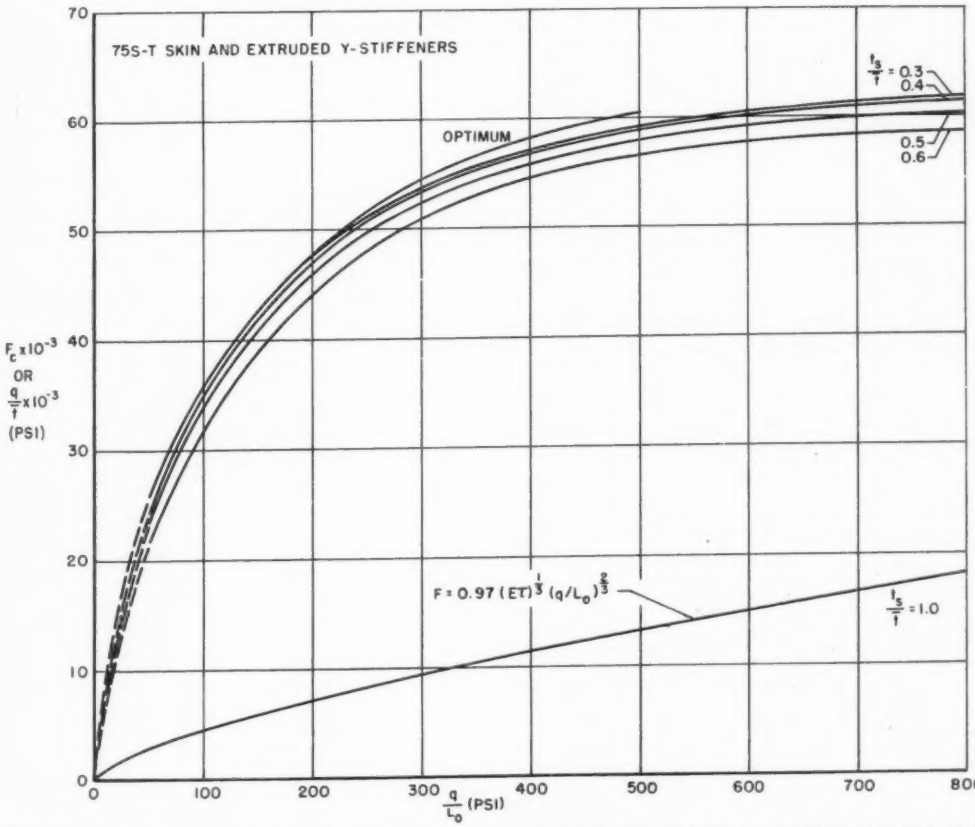

FIG. 2 — MAXIMUM ALLOWABLE STRESS FOR 75S-T SHEET-STIFFENER PANELS FOR CONSTANT VALUES OF $\frac{t_s}{t}$

Note No. 1389, which contains data on tests of sheet-stiffener compression panels. Fig. 20 shows a plot of $q/\bar{t}$ vs. q/t_s for lines of constant q/L_0, where

q = average load per inch width (lbs. per in.) = total load divided by total width
$\bar{t}$ = average thickness of the panel (in.) = total area divided by total width
t_s = skin thickness (in.)
L_0 = effective pin-end column length (in.)

Since the curves were composed of a series of arcs, envelopes were drawn to represent a continuous variation. These envelope curves are shown in Fig. 1.

The term $q/\bar{t}$ represents the average compressive stress developed in the panel. The term q/L_0 is the structural index,[2] which is a measure of the loading intensity. The parameter q/t_s, the average load per inch width divided by the skin thickness, is a convenient means for introducing the skin thickness as a parameter.

A straight line through the origin (Fig. 1) represents a line of constant value of the ratio $t_s/\bar{t}$, the slope being equal to $t_s/\bar{t}$. By cross-plotting the curves of Fig. 1 as $q/\bar{t}$ vs. q/L_0 for lines of constant $t_s/\bar{t}$, we can show how changing the ratio of skin thickness to average thickness affects the allowable stress for any value of structural index. This cross-plot is shown in Fig. 2.

It is apparent from Fig. 2 that, as the value of $t_s/\bar{t}$ is increased, the allowable stress is decreased. The lower curve, for $t_s/\bar{t} = 1.0$, represents the limiting case, wherein all of the material is in the skin. This curve was calculated from Eq. (15b) in reference 2. This expression for the allowable stress F_c of a flat plate used as an Euler column is

$$F_c = 0.97(E\tau)^{1/3}\,(q/L_0)^{2/3} \qquad (4)$$

where

E = modulus of elasticity (elastic range)
$\tau = E_t/E$, where E_t = tangent modulus

The position of this curve indicates that, as $t_s/\bar{t}$ approaches unity, the allowable stress drops off rapidly.

At higher values of q/L_0, it is likely that the rate of decrease of F_c with increases in $t_s/\bar{t}$ will be less pronounced. At the time of writing, however, there were no experimental data available which covered values of q/L_0 above a value of 800; therefore, this could not be shown by the curves.

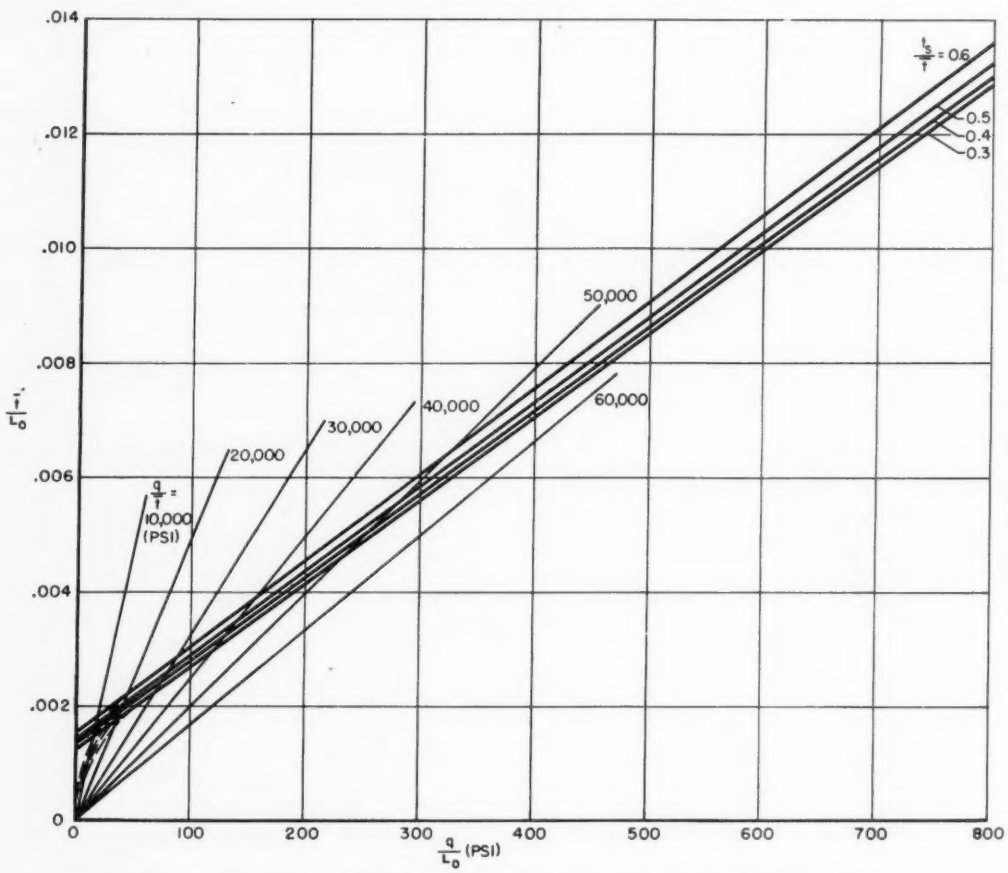

FIG. 3 — REQUIRED THICKNESS OF 75S-T SHEET-STIFFENER PANELS

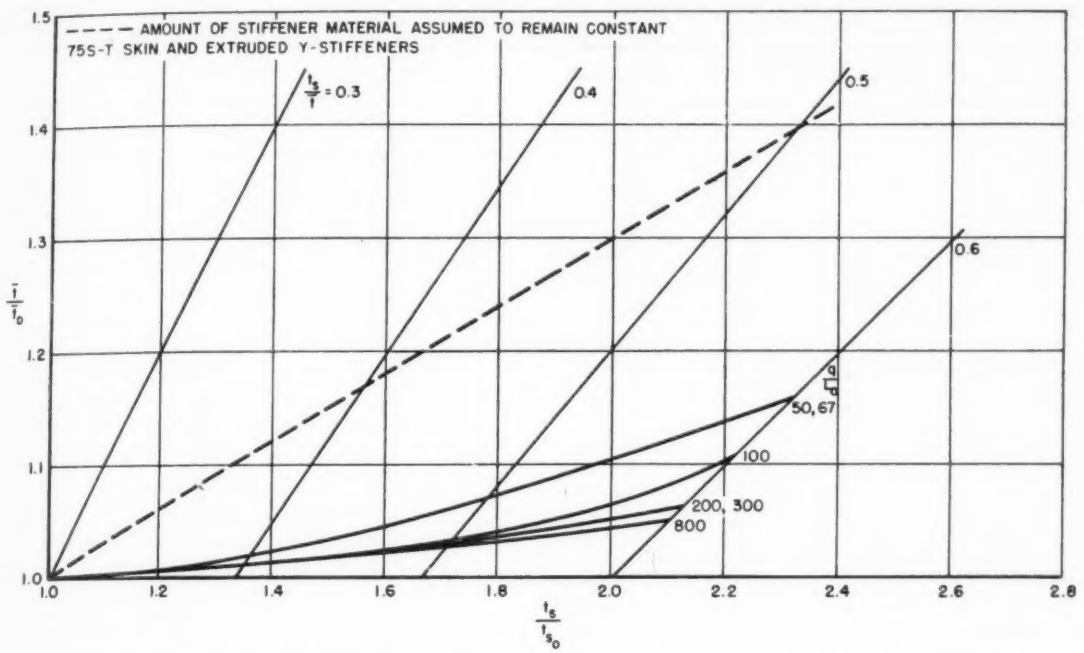

FIG. 4—VARIATION OF AVERAGE PANEL THICKNESS WITH CHANGES IN SKIN THICKNESS

It can be seen that the curve representing optimum (minimum-weight) design may be attained only by using an extremely low value of $t_s/\bar{l}$. This indicates that such a value of allowable stress is not likely to be attained in compression panels designed for use in wing structures. For this reason, it is desirable to qualify allowable-stress curves, of the type shown in Fig. 2, with values of $t_s/\bar{l}$. The ratio $t_s/\bar{l}$ is a useful parameter for estimating the relative amount of torsional stiffness which would be contributed by the panel when used in a wing structure. Its use introduces a further convenience because, according to the design charts of reference 1, for a specified value of $t_s/\bar{l}$ there exists a variety of combinations of stiffener size and spacing which will yield very nearly the same allowable stress as the maximum for that value of $t_s/\bar{l}$ shown in Fig. 2.

As shown by Shanley,[2] the average thickness may be determined from curves of the type shown in Fig. 2 and approximated by a straight line as follows: If the value of q/L_0 at each point on the curves is divided by the corresponding value of $q/\bar{l}$, we can obtain curves of $\bar{l}/L_0$ vs. q/L_0 as shown in Fig. 3. These curves can be closely approximated by straight lines. For the set of curves in Fig. 3, the straight lines are not distinguishable from the curves except at extremely low values of q/L_0. The expression for the line is given by

$$\bar{l}/L_0 = C_c + [(q/L_0)/F_{c_0}] \tag{5}$$

where

C_c = intercept value at $q/L_0 = 0$
F_{c_0} = effective stress = 1/slope of the line

The average thickness may be written

$$\bar{l} = C_c L_0 + (q/F_{c_0}) \tag{6}$$

For any value of $t_s/\bar{l}$, the total average thickness $\bar{l}$ required at any value of q/L_0 may be found from this expression. For a value of $t_s/\bar{l} = 0.6$, the expression for the average thickness is

$$\bar{l} = 0.00155L_0 + (q/83{,}000)$$

For example, if a panel 20 in. in length and having pin-end conditions is subjected to a loading of 300 lbs. per in., the total average thickness required is 0.0246 in., of which the skin thickness is 0.0148 in. It should be remembered that these numbers refer to panels made of 75S-T Alclad skin and 75S-T extruded Y-section stiffeners.

Fig. 2 shows how a change in the ratio $t_s/\bar{l}$ affects the allowable average stress. However, it does not show how the average thickness is affected by changes in skin thickness, the loading remaining constant. This can be done as follows:

Using Fig. 1 and choosing some value of $t_s/\bar{l}$ to be used as a reference value (designated by $t_{s_0}/\bar{l}_0$), we can obtain curves of t_s/t_{s_0} vs. $\bar{l}/\bar{l}_0$ for each line of constant q/L_0, where

t_{s_0} = skin thickness of a panel having a value of $t_s/\bar{l}$ equal to the reference value
$\bar{l}_0$ = average thickness of a panel having a value of $t_s/\bar{l}$ equal to the reference value

The term t_s/t_{s_0} represents the ratio of an arbitrary skin thickness to the skin thickness of the panel having $t_s/\bar{t}$ equal to the reference value. The term $\bar{t}/\bar{t}_0$ is the corresponding ratio of the average thicknesses.

The value of $t_s/\bar{t} = 0.3$ will be chosen as the reference value because it represents a limiting case for the curves of Fig. 1 and all values of t_s/t_{s_0} and $\bar{t}/\bar{t}_0$ will be greater than unity.

For each line of constant q/L_0, the intersection with the line of $t_s/\bar{t} = 0.3$ gives values of $q/\bar{t}_0$ and q/t_{s_0} for that particular value of q/L_0. Then, for each line of constant q/L_0, the values of $q/\bar{t}_0$ and q/t_{s_0} are divided by the ordinates and abscissas defining that line. The resulting values are plotted in Fig. 4 as $\bar{t}/\bar{t}_0$ vs. t_s/t_{s_0} for lines of constant q/L_0.

For example, Fig. 4 shows that, for a panel having an initial value of $t_s/\bar{t} = 0.3$ and a structural index of 300 lbs. per sq.in., the skin thickness may be doubled at the cost of only 5 per cent increase in total panel weight if optimum design methods are employed. The dashed line shows the variation of panel weight based on the assumption that any increase in skin weight will increase the total panel weight by the same amount.

Conclusions

The curves of allowable stress F_c vs. q/L_0 representing "optimum" design for given types of sheet-stiffener panels show that this minimum-weight design can be attained only at extremely low ratios of $t_s/\bar{t}$. Since wing panels are not designed on the basis of allowable compressive stress alone, curves of this type should show how much of the panel material is made up of skin and can be counted on to resist torsion. One method of indicating the relative amount of material in the skin is illustrated by the curves of Fig. 2, which are drawn for constant values of $t_s/\bar{t}$.

The allowable stress curves of Fig. 2 can be cross-plotted as shown in Fig. 3 and closely approximated by straight lines, resulting in a simplified analytical expression for the relationships involved. Straight-line approximations of this type have been used conveniently in wing-weight-estimation procedures.[3]

Fig. 4 illustrates the manner in which panel weight must change with changes in skin thickness and shows the overconservatism of the assumption represented by the dashed line. For an actual design, where the values of both q and q/L_0 are known, the curves of Fig. 1 could be used to calculate directly any change in panel weight for a given change in skin thickness.

As the skin becomes an increasingly greater fraction of the total panel thickness, the construction approaches the "panel" type[2] in which a lighter construction may be obtained by putting all of the material in the skin and running the separators spanwise rather than chordwise. In this type of construction, which uses all the panel material to resist torsion, the compressive strength of the panel will depend on the width rather than on the length. If the data had covered a higher range of values of q/L_0 and skin thickness, the curves of sheet-stiffener construction could be extended to show a comparison of these two types of construction and would then indicate the values of t_s/t_{s_0} and q/L_0 at which it would be advantageous to change from one type of construction to the other.

References

[1] Dow, Norris F., and Hickman, William A., *Design Charts for Flat Compression Panels Having Longitudinal Extruded Y-Section Stiffeners and Comparison with Panels Having Formed Z-Section Stiffeners*, N.A.C.A. T.N. No. 1389, August, 1947.

[2] Shanley, F. R., *Principles of Structural Design for Minimum Weight*, Journal of the Aeronautical Sciences, Vol. 16, No. 3, p. 133, March, 1949.

[3] Shanley, F. R., *Structural Weight Analysis—General Method: Wing Structures*, Project RAND, The RAND Corporation, Report R-100, October 1, 1948, unclassified.

Readers' Forum

BRIEF REPORTS of investigations in the aeronautical sciences and discussions of papers published in the JOURNAL are presented in this special department. The publication will be completed approximately 8 weeks after receipt of the material. The Editorial Committee does not hold itself responsible for the opinions expressed by the correspondents. Contributions should not exceed 800 words in length.

Correction for "The Effect of Variation of Mass on the Dynamic Stability of Jet-Propelled Missiles"*

M. V. Barton
Professor of Aeronautical Engineering and Research Engineer, Defense Research Laboratory, The University of Texas
August 1, 1950

MR. A. H. FLAX, of the Cornell Aeronautical Laboratory, Inc., has pointed out that there is an error in the expressions for the jet damping force and moment of the air-jet-type missile. This error comes about by neglecting the sudden change of momentum of the incoming air at the entrance of the duct. The air at the entrance of the duct has a velocity component of Ql_2 at right angles to the undisturbed stream. The sudden change in momentum thus produces a force at the lip of c_aQl_2 and a moment of $c_aQl_2^2$. When these quantities are added to the expressions for the forces and moments representing the integrated coriolis forces [Eqs. (10) of the paper] the jet damping force becomes

$$2[c(l_0 - l_1) + c_al_0]Q$$

and the damping moment is

$$[c_al_0^2 + c(l_0^2 - l_1^2)]Q$$

The net effect of this change can be effected by setting $l_2 = 0$ in the final equations.

The general conclusions in the paper are not generally modified by this change except that the possibility of negative damping in the case that $l_2 > l_0$ is precluded.

* JOURNAL OF THE AERONAUTICAL SCIENCES, Vol. 17, No. 4, pp. 197–203, April, 1950.

Roll to Sideslip or Yaw Ratios

Dunstan Graham and Allan McCaskill
Flight Research, Cornell Aeronautical Laboratory, Inc., Buffalo, N.Y.
August 23, 1950

REFERENCE 1 SUGGESTS the ratio of amplitudes of the rolling motion to the yawing or sideslipping motion in the lateral-directional oscillation of airplanes as a possible pilots' criterion for the upper limit of acceptable effective dihedral. Relative amplitudes of roll and sideslip in unforced oscillations should not, however, be confused with the bank angle to sideslip ratio in cross-controlled rectilinear flight which may be shown to depend entirely on other aerodynamic characteristics.

Since the solutions to the equations of lateral, stick-fixed motion of an airplane are of the form[2]

$$\beta,\ p,\ \text{or}\ r = C_1e^{\lambda_1 t} + C_2e^{\lambda_2 t} + C_3e^{\xi t}\ (\cos \psi t - C_4) \quad (1)$$

the ratios defining the relative magnitudes of rolling and yawing or rolling and sideslipping are functions of the three values of C_3. These constants of integration are expressions containing the various airplane stability derivatives, mass factors, disturbing functions, and the roots of the characteristic equation raised to various powers and multiplied together in an involved manner. Fortunately, however, the use of sweeping, simplifying assumptions permits the development of approximate formulas for the roll-to-sideslip ratio and the roll-to-yaw ratio whose accuracy does not seem to have been unduly affected by the simplification.

Thus, if the lateral motions are assumed to be described by the emaciated differential equations

$$\left.\begin{aligned} -\frac{dp}{d(t/\tau)} + l_vp - \mu l_v \int r\, d(t/\tau) &= \sum L \\ -\frac{dr}{d(t/\tau)} - \mu n_v \int r\, d(t/\tau) &= \sum N \end{aligned}\right\} \quad (2)$$

(these equations assume an undamped directional oscillation with the rolling motion coupled only through the dihedral effect and no lateral motion of the c.g.), the solution for the oscillatory components of $p(t)$ and $r(t)$ following a step yawing moment disturbance gives

$$\frac{|p(t)|_{\text{osc.}}}{|r(t)|_{\text{osc.}}} = \frac{\varphi}{\psi} = \frac{\varphi}{\beta} = \left| \frac{\mu l_v}{\eta^2\sqrt{1 + (l_p/\eta)^2}} \right| \quad (3)$$

where

- φ = rolling oscillation amplitude
- ψ = yawing oscillation amplitude
- β = sideslipping oscillation amplitude
- μ = airplane relative density parameter $= m/\rho Sb$
- l_v = nondimensional rolling acceleration due to sideslip (dihedral effect) $= (1/2)(b/k_x)^2C_{l_\beta}$
- l_p = nondimensional rolling acceleration due to rolling (damping in roll) $= (1/4)(b/k_x)^2C_{l_p}$
- n_v = nondimensional yawing acceleration due to sideslip (directional stability) $= (1/2)(b/k_z)^2C_{n_\beta}$
- η = nondimensional frequency of oscillation (radians per unit t/τ) = imaginary part of complex root of characteristic equation
- k_x = radius of gyration in roll (ft.)
- k_z = radius of gyration in yaw (ft.)
- C_{l_β} = rolling moment coefficient due to sideslip (per rad.)
- C_{l_p} = rolling moment coefficient per unit wing tip helix angle, $pb/2U$
- C_{n_β} = yawing moment coefficient due to sideslip (per rad.)
- τ = unit of aerodynamic time $= m/\rho sU$

This result may also be derived by neglecting the effects of product of inertia and inclination of the flight path, assuming zero damping of the oscillation and the stability derivatives $l_r = n_r = n_p = 0$ in the complete expression for φ/β.

Similar assumptions applied to the complete expression for φ/ψ give as an approximation

$$\frac{\varphi}{\psi} = \left| \frac{l_v}{n_v} \frac{1}{\sqrt{1 + (l_p/\eta)^2}} \right| \quad (4)$$

The same results are obtained no matter what the form of the yawing or rolling moment disturbance may be.

Under certain circumstances [as it is in Eq. (2)] $\eta = \sqrt{\mu n_v}$ is a valid approximation to the imaginary part of the complex root of the characteristic equation. The expressions for φ/β and for φ/ψ are then equivalent. At high altitude and high lift coeffi-

cients, however, $\eta \neq \sqrt{\mu n_v}$, and φ/β and φ/ψ may be markedly different.

The approximate expressions given by Eqs. (3) and (4) check numerically with the complete expressions (within 10–12 per cent) even for some extreme flight conditions and radical airplane configurations. Where the inclination of the airplane's principal longitudinal axis is significant, the root η must be computed taking the changes in inertia and the product of inertia into account. Otherwise, the approximations are still good. For the combination of high dihedral effect and large positive inclination of the principal axis, the approximation fails completely, and the same is true for conditions of extremely low directional stability. Some error exists in predictions (by the approximate formulas) of the airplane's response to disturbances from its controls because of the facts that the ailerons do not produce a pure rolling moment and the rudder does not produce a pure yawing moment. This is particularly true of some ailerons. In one typical case, however, other errors inherent in the approximation slightly more than canceled the error due to neglecting aileron adverse yaw, and the result was again in good agreement with the more exact calculation.

Effects of design changes or trends on the roll-to-yaw and roll-to-sideslip ratios may perhaps be best discerned by considering the effects on the stability derivatives contained in the approximate expressions. For instance, since l_β is proportional to the dihedral effect and inversely proportional to the rolling moment of inertia, an increase in the dihedral effect will result in an almost exactly proportionate increase in φ/β and φ/ψ. Decreasing the rolling inertia will tend to have the same effect, modified, however, by the corresponding change in l_p.

If the roll-to-sideslip or -yaw ratios should achieve reputability as a significant parameter, the approximate expressions may be useful for checking calculations of these quantities and as a guide to designers in the labyrinthine choice of fin area and dihedral.

References

[1] Liddell, Charles J., Jr., Van Dyke, Rudolph D., Jr., and Heinle, Donovan R., *A Flight Determination of the Tolerable Range of Effective Dihedral on a Conventional Fighter Airplane*, N.A.C.A. T.N. No. 1936, August, 1949.

[2] Zimmerman, C. H., *An Analysis of Lateral Stability in Power-Off Flight with Charts for Use in Design*, N.A.C.A. T.R. No. 589, 1937.

On the Plastic Buckling of Plates

P. P. Bijlaard
Cornell University, Ithaca, N.Y.
August 8, 1950

In an interesting Readers' Forum item (Journal, June, 1950, p. 378) Dr. Cicala calculates approximately the reduction, caused by eccentricity in the buckling stress of a compressed plate with one unloaded side simply supported and the other free. Assuming the incremental (or flow) theory to be valid and assuming initial shear strains γ_0 of $0.04\tau_p/G$ and $0.1\tau_p/G$ he finds eccentric buckling stresses σ_e of about *0.75* and *0.66* times the concentric ones, respectively.

Since these eccentric buckling stresses are for these eccentricities and for this special case of the order of magnitude of the concentric buckling stresses according to the deformation theory, he suggests that in this way the excellent confirmation of the latter by buckling experiments may be explained.

The assumed eccentricities, which obviously are suggested to be inevitable in concentrically loaded plates, are, however, rather large. From Dr. Cicala's formula the initial angle of twist of the mid-section is

$$\beta_{0\,max.} = \gamma_0 L/\pi s \tag{1}$$

According to the simple incremental theory the concentric buckling stress is equal to the elastic one—i.e., using Dr. Cicala's notations

$$\sigma_{cr.} = G(s/b)^2 \tag{2}$$

With $\sigma_{cr.} = 1.5\sigma_p$, $G = 4{,}000{,}000$ lbs. per sq.in. and a proportional limit $\sigma_p = 30{,}000$ lbs. per sq.in., Eq. (2) yields $b/s = 9.5$. Since $\tau_p = 0.577\sigma_p$ and assuming $L/b = 10$ so that $L/s = 95$, the assumed initial strains γ_0 of $0.04\ \tau_p/G$ and $0.1\ \tau_p/G$ result from Eq. (1) in initial angles of twist of 0.0052 and 0.0131, respectively. The corresponding maximum initial deflections $\beta_{0\,max.}\,b$ of the free edge are $0.049s = 0.3k$ and $0.125s = 0.75k$, respectively, where k is the core radius $k = h/6$.

These eccentricities are large, since the other unloaded edge is held straight by the support. Therefore the ratios $\mu = \sigma_e/\sigma_{cr.} = 0.75$ and 0.66 between eccentric and concentric buckling stresses are not extraordinary low. For a simply supported steel column of rectangular cross section and slenderness ratio 100, although having a smaller L/s ratio than the plate, initial eccentricities e of $0.25k$ and $0.75k$ cause ratios $\mu = \sigma_e/\sigma_{cr.}$ (where $\sigma_{cr.}$ is the tangent modulus buckling stress) of *0.70* and *0.55*, respectively,[1] if, somewhat analogous to Dr. Cicala's approximation, the case of initial end eccentricities e is considered.

Thus, the influence of eccentricities on the column buckling stress is of the same order of magnitude as for the plate. If eccentricities of this amount were really inevitable in experiments with theoretically concentrically loaded plates and columns, it should be expected that with concentrically loaded columns similar reductions in buckling stress would also occur. Nevertheless, the experimental buckling stresses for the latter case are in good agreement with the concentric Engesser (tangent modulus) buckling stress. The theoretical Shanley buckling stress is somewhat higher than the Engesser stress, since after deflection the resistance increases a little because of partial elastic unloading of the fibers. Hence, the inevitable eccentricities obviously cause only a decrease from the actual concentric buckling stress to the Engesser stress, which supposes fully plastic behavior. Consequently, the inevitable eccentricities are much smaller than assumed by Dr. Cicala, and there is no reason to expect experimental buckling stresses of plates which are substantially lower than the concentric ones, calculated from the present writer's theory[1] in the same way as the Engesser stress—i.e., assuming fully plastic behavior.

Dr. Cicala assumes that above the proportional limit, σ_p, the tangent modulus E_t is constant and half of the elastic modulus E, although for aluminum a better approximation would be $E_t = E/30$ or $E/40$. It could be thought that with lower E_t the ratio $\mu = \sigma_e/\sigma_{cr.}$ would be less. This may be easily checked by assuming $E_t = 0$, so that σ_p is the yield stress.

Assuming $\sigma_{cr.} = \sigma_p$, it follows that, from comparison of external and internal torsional moments, with a compressive stress σ

$$\sigma(\gamma_0 + \gamma) = \sigma_p\gamma$$

so that the shear stress

$$\tau = G\gamma = G\gamma_0[\sigma/(\sigma_p - \sigma)] \tag{3}$$

Since, according to the yield condition

$$\sigma^2 + 3\tau^2 = \sigma_p^2 \tag{4}$$

the yield stress σ_p is reached when, from Eq. (3),

$$\sigma^2 + 3G^2\gamma_0^2[\sigma^2/(\sigma_p - \sigma)^2] = \sigma_p^2$$

or, with

$$\gamma_0^2 = \alpha^2(\tau_p^2/G^2) = (\alpha^2/3)(\sigma_p^2/G^2) \tag{5}$$

when

$$(1 + \mu)(1 - \mu)^3 - \alpha^2\mu^2 = 0 \tag{6}$$

in which

$$\mu = \sigma/\sigma_p$$

After reaching the yield stress, however, with further twisting τ will increase, so that from Eq. (4) the compressive stress σ will decrease. Hence, the maximum stress (since membrane stresses may be neglected here) and thus the eccentric buckling stress σ_e follow directly from Eq. (6), in which, consequently,

$$\mu = \sigma_e/\sigma_p \tag{7}$$

With the assumed values $\gamma_0 = 0.04\tau_p/G$ or $0.1\tau_p/G$, or from Eq. (5), with $\alpha = 0.04$ or 0.1, Eq. (6) yields

$$\mu = \sigma_e/\sigma_p = 0.84 \text{ or } 0.91$$

It follows from Eq. (2) that here, with $\sigma_{cr.} = \sigma_p = 30{,}000$ lbs. per sq.in., $b/s = 11.5$, so that with $L/b = 10$, from Eqs. (1) and (5), $\beta_{0\,max.} = 0.158\alpha$. Hence, the maximum deflection $b\beta_{0\,max.}$ of the free edge is $1.83s\alpha$. With $\alpha = 0.04$ or 0.1, this yields eccentricities of $0.44k$ or $1.1k$.

On the other hand, with the same stress-strain diagram and assuming also $\sigma_{cr.} = \sigma_p$, for a rectangular simply supported column the ratio $\mu = \sigma_e/\sigma_{cr.}$ for eccentricities of $0.5k$ and k is 0.53 and 0.42, respectively,[2] and thus much less than for the plate. Even for an eccentricity of $0.1k$ it is still 0.75.

Hence, in this case, the influence of eccentricities is even more for the column than for the plate, which confirms the above conclusion that there is no reason to expect experimental plate buckling stresses much lower than the concentric ones.

The present writer's theory[3, 4] includes the possibilities of plastic behavior according to deformation (Hencky body), as well as flow theory (Prandtl-Reuss body), the latter case by equating value $e = (E/E_s) - 1$, where E_s is the secant modulus, to zero. Assuming the actual behavior to be between that described by deformation and flow theories, he already gave his own explanation for the agreement of the experiments with his results according to the deformation theory (reference 4, pages 532–533), on which he based his calculations from the beginning in order to remain on the safe side.[3] Eccentricity plays only a secondary role here, as far as it prevents unloading of the material, so that the plate may be assumed to remain plastic all over (reference 4, page 536). Moreover, it helps to increase σ during buckling, so that in most planes the active shearing stresses increase, in which case the plastic behavior will approximate that according to the deformation theory.

References

[1] Chwalla, E., *Discussions of Questions I_1 and I_2*, Int. Assoc. f. Bridge and Struct. Eng., 1st Congress, Paris, Final Report, pp. 53–63, 1932.

[2] Jezek, K., *Die Festigkeit von Druckstäben aus Stahl;* Springer, Vienna, 1937.

[3] Bijlaard, P. P., *A Theory of Plastic Stability and Its Application to Thin Plates of Structural Steel*, Proc. Kon. Akad. v. Wetensch., Amsterdam, Vol. 41, No. 7, pp. 731–743, 1938.

[4] Bijlaard, P. P., *Theory and Tests on the Plastic Stability of Plates and Shells*, Journal of the Aeronautical Sciences, Vol. 16, No. 9, pp. 529–541, September, 1949.

Plastic Column Behavior

N. J. Hoff

Head of Department of Aeronautical Engineering and Applied Mechanics, Polytechnic Institute of Brooklyn, Brooklyn, N.Y.

August 16, 1950

IN A THOROUGH ANALYSIS presented by Dr. John A. Duberg and Thomas W. Wilder, III, under the title "Column Behavior in the Plastic Stress Range" published in this JOURNAL in June, 1950, the variations in stress and strain in columns buckling in the plastic range and the maximum loads the columns are able to carry after buckling were calculated. This writer does not want to add to, or detract anything from, the results of these calculations, which are undoubtedly correct and contribute considerably to our knowledge of column behavior. However, he wants to mention a few basic issues related to our way of thinking about columns in general.

First, it should be pointed out that the classical definition of stability is not ambiguous but leads to a unique buckling load even in the inelastic range. According to the classical procedure, the buckling load is calculated as the load under which the stability of the system is neutral. The system consists of a given elastic body upon which given loads are acting. The loads are constant even though their magnitude is unknown. It can be seen from Fig. 2 of the paper quoted that infinitesimal deflections are possible without a change in load only at the reduced modulus load P_{RM} derived by von Kármán. This is the unique buckling load according to the classical theory.

The load of real interest to the engineer is that obtainable during some loading process rather than the theoretical neutral stability load. This is so because columns will seldom collapse under constant loads but rather during the period when they are loaded. To talk of the stability of a system that is in a state of continuous, or even discontinuous, change of loading (the latter being the case when dead weights are used in loading the elastic body) is not possible without defining first what is meant by the term. One possible definition of the buckling load is the maximum load the column can support during the loading process. This definition has the advantage that it can be easily correlated to buckling tests in which the maximum load is the principal quantity measured. The intrinsic importance of the maximum load was recognized by the authors, inasmuch as they presented several diagrams containing it. Another proper choice of the buckling load is the load at which the deflections of an initially slightly curved column become inadmissibly large. The value of this load can be taken from diagrams of the type shown in Fig. 4 of the subject paper after the meaning of the word "inadmissible" is defined in some exact manner. Finally, the authors' definition is also a feasible one: The buckling load can be taken as the load at which an initially straight column begins to deflect if its behavior is assumed to be the limit of the behavior of an initially slightly curved column whose initial deviations from straightness are made to approach zero. This definition is only one of many other equally arbitrary definitions. It has no particular theoretical significance, and it is not certain—or even likely—that a perfect column would behave as indicated by the limiting process. Its practical importance is also not obvious, since the slope of the load-deflection curve of an initially slightly curved column changes abruptly below the tangent modulus load if Fig. 4 is indicative of the behavior of real columns and since the maximum load the column can support is always greater than the tangent modulus load as shown in Fig. 9.

Moreover, it must not be forgotten that the entire analysis of the paper is based on the assumption of an infinitely slow monotonically increasing loading process in which the inertia forces can be neglected. That this last assumption is permissible is not obvious to the writer of this discussion. For this reason, under the sponsorship of the Office of Naval Research of the U.S. Navy, he undertook the investigation of the actual motion of a column during the process of loading in a testing machine making use of the dynamic equation of motion. The results of the calculations as related to perfectly elastic columns were presented under the title "The Dynamics of the Buckling of Elastic Columns" at the Annual Summer Meeting of the Applied Mechanics Division of the A.S.M.E. in June, 1950. Work is now in progress at the Polytechnic Institute of Brooklyn on the problem of the inelastic column.

Finally, it may be mentioned that the definition of instability admits of a further generalization. A system should be con-

sidered stable if its equilibrium is automatically re-established after a disturbance. In systems that are not perfectly linear, the magnitude of the disturbance is a decisive factor, and in the presence of dry friction or plastic deformations the original state of equilibrium is regained, as a rule, only approximately. For these reasons the writer proposed in his paper "Dynamic Criteria of Buckling" (*Research, Engineering Structures Supplement*, Butterworths Scientific Publications, Ltd., London, and Academic Press, Inc., New York, 1949, page 121) that the stability of such systems be investigated by determining their motion following a disturbance. They should be considered stable if after a reasonable time they return reasonably close to their original position of equilibrium. The nature and the magnitude of the disturbance, the specification of a "reasonable" time, and the definition of the expression "reasonably close" depend upon the circumstances and cannot be established in advance for all possible systems. The paper discusses the problems involved with the aid of simple dynamic models.

The writer wishes to emphasize once more that it is not his intention to minimize the substantial advances made by Dr. Duberg and Mr. Wilder in column theory. He feels, however, that further improvements of our knowledge of column action are possible, and he wants to indicate the direction in which, in his opinion, they might be attained.

A Note on the Calculation of Oblique Shock-Wave Characteristics*

M. J. Thompson
Professor and Chairman of the Department of Aeronautical Engineering; Associate Director, Defense Research Laboratory, The University of Texas

July 27, 1950

THIS NOTE IS CONCERNED WITH a simplified method for handling the numerical calculations involved in determining the characteristics of an oblique shock wave in supersonic flow. The wave is considered as being formed at the leading edge of a two-dimensional airfoil section having a nose angle θ_s between its surface and the free-stream direction. The problem originated as a part of a study of airfoil pressure distribution.[1]

Using the method of analysis employed by Taylor and Maccoll,[2] the wave angle, pressure ratio, downstream Mach Number, and other desired flow characteristics may be determined in terms of the wedge angle and the free-stream Mach Number. The method of solution, however, is an indirect one and generally requires the use of elaborate charts and a considerable amount of cross-plotting. By using this method it is possible to set up an expression for the pressure ratio in the form of a quartic, with algebraic coefficients that depend on the free-stream Mach Number M_1, the wedge angle θ_s, and the ratio of specific heats, γ, for the gas.

The present analysis follows the method used by Liepmann and Puckett[3] and others. The relation from which the wave angle θ_w may be determined is

$$\frac{1}{M_1^2} = \sin^2\theta_w - \left(\frac{\gamma+1}{2}\right)\frac{\sin\theta_w \sin\theta_s}{\cos(\theta_w - \theta_s)} \tag{1}$$

Expressions for the other characteristics may also be derived in terms of the known quantities defined above and the wave angle computed from Eq. (1). In order to use Eq. (1), Laitone,[4] for example, assumes a series of values of θ_w for a given M_1 and computes θ_s.

Eq. (1) may be rewritten in the form

$$\sin^6\theta_w + b\sin^4\theta_w + c\sin^2\theta_w + d = 0 \tag{2}$$

where

$$b = -\{[(\gamma+1)M_1^2 + 2]\tan^2\theta_s + M_1^2 + 2\}/M_1^2 \times (1+\tan^2\theta_s \tag{3}$$

$$c = \{[(\gamma+1)M_1^2 + 2]^2\tan^2\theta_s + 8M_1^2 + 4\}/4M_1^4(1+\tan^2\theta_s) \tag{4}$$

$$d = -1/M_1^4(1+\tan^2\theta_s) \tag{5}$$

which is a cubic in $\sin^2\theta_w$ and may be solved directly by numerical procedures such as Tartaglia's method. Thus, any desired degree of accuracy can be maintained in the calculations, and, what is more important, θ_w is obtained directly for any given values of M_1, θ_s, and γ without the necessity of trial-and-error solutions and cross-plotting. Such a procedure is more readily adapted to comparison with wind-tunnel test results in which M_1 and θ_s are the primary independent variables.

It is also interesting to note that, in the special case where $\theta_s = 0$, Eqs. (3), (4), and (5) reduce to

$$b_0 = \frac{-(M_1^2+2)}{M_1^2}, \quad c_0 = \frac{2M_1^2+1}{M_1^4}, \quad d_0 = -\frac{1}{M_1^4} \tag{6}$$

Furthermore, Eq. (2) is now factorable, the significant roots being

$$\sin\theta_w = 1/M_1, \quad \sin\theta_w = 1 \tag{7}$$

The second root, of course, has no physical significance, while the first corresponds to the Mach wave created by an infinitesimal point disturbance.

The values of Eq. (6) may be introduced into Eqs. (3), (4), and (5) so that the latter become

$$b = -[(M_1^2+2)/M_1^2] - \gamma\sin^2\theta_s \tag{8}$$

$$c = \frac{2M_1^2+1}{M_1^4} + \left[\frac{(\gamma+1)^2}{4} + \frac{(\gamma-1)}{M_1^2}\right]\sin^2\theta_s \tag{9}$$

$$d = -\cos^2\theta_s/M_1^4 \tag{10}$$

While these forms do not permit the factoring of the original expression, Eq. (2), nor do they provide for a complete separation of the effects of Mach Number and wedge angle, they are believed to be somewhat simpler in form and better adapted to numerical calculation procedures than Eqs. (3), (4), and (5).

* Acknowledgment is made to the Navy Bureau of Ordnance for its support of this work under Contract NOrd-9195, which is a part of the Bumblebee guided-missile program.

REFERENCES

[1] Thompson, M. J., *A Study of Airfoil Pressure Distribution at Supersonic Speeds*, Defense Research Laboratory Report No. 142, CF-821, November 15, 1947.

[2] Taylor, G. I., and Maccoll, J. W., *The Mechanics of Compressible Fluids*, Vol. III, Div. H of *Aerodynamic Theory*, Edited by W. F. Durand, pp. 236–243; Durand Reprinting Committee, Pasadena, Calif., January, 1943.

[3] Liepmann, H. W., and Puckett, A. E., *Introduction to the Aerodynamics of a Compressible Fluid*, pp. 51–58; John Wiley & Sons, Inc., New York, 1947.

[4] Laitone, Edmund V., *Exact and Approximate Solutions for Two-Dimensional Oblique Shock Flow*, Journal of the Aeronautical Sciences, Vol. 14, No. 1, January, 1947.